This is to certify that the
dissertation entitled

VIBRATIONAL COHERENCE IN ZINC PORPHYRINS IN POLAR SOLUTIONS AND IN PROTEINS: VAN DER WAALS INTERACTIONS WITH SURROUNDING GROUPS IN THE FIRST SOLVATION SHELL

presented by

Kevin Lawrence Dillman

has been accepted towards fulfillment
of the requirements for the

Ph.D. degree in Chemistry

Warren F. Beck
Major Professor's Signature

17 December 2009
Date

VIBRATIONAL COHERENCE IN ZINC PORPHYRINS IN POLAR SOLUTIONS AND IN PROTEINS: VAN DER WAALS INTERACTIONS WITH SURROUNDING GROUPS IN THE FIRST SOLVATION SHELL

By

Kevin Lawrence Dillman

A DISSERTATION

Submitted to
Michigan State University
in partial fulfillment of the requirements
for the degree of

DOCTOR OF PHILOSOPHY

Chemistry

2009

ABSTRACT

VIBRATIONAL COHERENCE IN ZINC PORPHYRINS IN POLAR SOLUTIONS AND IN PROTEINS: VAN DER WAALS INTERACTIONS WITH SURROUNDING GROUPS IN THE FIRST SOLVATION SHELL

By

Kevin Lawrence Dillman

We have employed femtosecond dynamic-absorption spectroscopy to monitor the low-frequency vibrational coherence from Zn^{II} tetrakis(N-methylpyridyl)porphyrin (ZnTMPyP) in polar solutions and Zn^{II}-substituted cytochrome *c* (ZnCytc). The ground-state vibrational coherence from ZnTMPyP is dominated by rapidly damped components whose intensities are perhaps an order of magnitude stronger than the more slowly damped components that arise from the skeletal normal modes of the porphyrin macrocycle. The mean frequencies of the rapidly damped features exhibit a solvent-dependent shift. The shift is consistent with a van der Waals potential dominated by London-dispersion interactions. In the excited-state vibrational coherence, these components exhibit an increase in frequency that suggests the potential is altered by the presence of charges. These components are assigned to intermolecular vibrational modes between the porphyrin and clustered, first-shell solvent molecules. The vibrational coherence from ZnCytc in the native state is exhibits similar behavior. Low-frequency metal-doming modes contribute ~10 and ~30 cm^{-1} oscillatory features, but the strongest component in the vibrational coherence is a very rapidly damped (damping time γ<150 fs) contribution centered at 79 cm^{-1}. This feature is assigned to van der Waals interactions between the porphyrin chromophore and

nearby nonpolar amino-acid residues in the surrounding protein medium. The vibrational coherence from the molten-globule state of ZnCytc does not exhibit the rapidly damped feature. Its resonance Raman activity is effectively quenched owing to expansion of the hydrophobic core and randomization of the surrounding structure. The results strongly suggest that the van der Waals modes gain resonance Raman activity through a direct attack of the solvent or neighboring groups on the π-electron density of the porphyrin chromophore. These findings provide the first structural accounting for the rate-controlling, low-frequency vibrational motions that are coupled to the electron-transfer reactions in photosynthesis.

ACKNOWLEDGMENTS

The research presented in this dissertation could not have been performed without the support of many other individuals. First and foremost is that of my advisor, Professor Warren Beck. I thank him for his invaluable guidance and his mentorship. Without him and the effort he has put into teaching me, this work would have been impossible. I thank my committee members, Professor Marcos Dantus, Professor James McCusker and Professor Lynmarie Posey for their time and input.

I thank Dr. Kathrine Shelly and Dr. Sanela Lampa-Pastirk for their patience and instruction. They taught me almost everything I know about how to perform femtosecond spectroscopy. I also thank my fellow graduate student Jagnyaseni Tripathi. Her curiosity and questions have led me to a better understanding of my own work. I have been fortunate to work with several talented undergraduate students, and I particularly wish to acknowledge Kenneth Barnes, Aaron Dame and Steven Miller.

I must also thank my entire family, who have provided me with endless encouragement. Specifically, I must thank my parents, Tom and Ellen Dillman, who have always been there to support me, and my brother, Peter, for his excellent friendship.

I thank the Department of Chemistry at Michigan State University for a Teaching Assistantship (2005–2009). This research was supported by the National Science Foundation Biomolecular Systems Cluster/Molecular Biophysics program under grants MCB-009120 and MCB-0520002. Additional support for instrumentation was provided by the Michigan Structural Biology Center at Michigan State University, which is supported by the Michigan Life Sciences Corridor.

TABLE OF CONTENTS

LIST OF TABLES

LIST OF FIGURES

LIST OF ABBREVIATIONS

B777, monomeric subunit protein of B820

B820, dimeric subunit protein of the LH1 light-harvesting complex

BChl, bacteriochlorophyll

$BPhe_L$, primary electron acceptor in the photosynthetic reaction center

CD_3OD, perdeuturated methanol

CH_3OH, methanol

CH_3CN, acetonitrile

DMF, N,N-dimethylformamide

DMSO, dimethylsulfoxide

ESA, excited-state absorption

FeCytc, Fe^{III} cytochrome *c*

fwhm, full width at half maximum

K, lysene

Mb, myoglobin

N, asparagine

P, primary electron donor in the photosynthetic reaction center

PB, photobleaching

Q_a, primary quinone electron acceptor in the photosynthetic reaction center

Q_b, secondary quinone electron acceptor in the photosynthetic reaction center

RISRS, resonant impulsive stimulated Raman scattering

SE, stimulated emission

T, threonine

W, tryptophan

Y, tyrosene

ZnCytc, Zn^{II} cytochrome *c*

ZnTMPyP, Zn^{II} *meso*-tetrakis(N-methylpyridyl)porphyrin

ZnTPP, Zn^{II} tetraphenylporphyrin

CHAPTER 1

Introduction

The electron-transfer reactions in the purple-bacterial photosynthetic reaction center are nearly barrierless.[1] Low-frequency vibrational modes that couple to the reaction account for the majority of the reorganization energy that matches the driving force in the Marcus theory for condensed-phase electron-transfer rates[2-4] and contribute to the barrierless reaction kinetics. The structural origin of these modes has not been previously determined. This dissertation provides the first detailed structural accounting for the vibrational motions that are coupled to the electron-transfer reactions in photosynthesis. The findings suggest that the relevant vibrational modes are intermolecular in nature. They arise from van der Waals interactions between the chromophore and nearby amino-acid residues in the surrounding protein medium.

This dissertation is organized as follows:

Chapter 2 introduces some of the previous contributions that have led to the principal work covered in this dissertation. We briefly cover the nature of the electron-transfer reactions in the photosynthetic reaction center, and we discuss the nature of the dynamic-absorption experiment. We examine the results of some of the early vibrational coherence measurements on the reaction center and the results of similar experiments on myoglobin and cytochrome *c*. We finish by discussing previous

work from this laboratory. Femtosecond dynamic-absorption spectroscopy on bacteriochlorophyll (BChl) in polar solution, and on the light-harvesting subunit proteins B777 and B820 reveal that the low-frequency vibrational coherence is dominated by rapidly damped components that are assigned to intermolecular vibrational modes. These modes exhibit a dependence on the dipole moment of the solvent. These results inspire the experiments discussed in the subsequent chapters.

In Chapter 3, we examine the origin of the rapidly damped vibrational coherence from Zn^{II} tetrakis(N-methylpyridyl)porphyrin (ZnTMPyP) with Soret-band excitation. ZnTMPyP has a high degree of symmetry, so it has a much smaller dipole moment than BChl. We discuss the effect this should have on the rapidly damped mode. We discuss how the dependence of the mean frequency of the intermolecular mode on the solvent dipole moment is consistent with a van der Waals intermolecular potential with the strongest terms coming from London-dispersion interactions. We show evidence of a isotope-dependent shift in the frequency of the intermolecular mode from methanol and perdeuturated methanol. We conclude that the rapidly damped vibrational modes arise from intermolecular modes with clustered, first-shell solvent molecules.

Chapter 4 discusses the intermolecular vibrational coherence from ZnTMPyP with Q-band excitation. The vibrational coherence observed in these experiments arises from wavepacket motion on the S_1 excited state. We observe that the intermolecular mode is shifted to substantially higher frequencies than previously obtained from ground-state vibrational coherence of ZnTMPyP. In the excited state of ZnTMPyP, the π-electron density extends over the N-methylpyridyl rings, so charge terms are added to the van der Waals intermolecular potential. We discuss how these terms dominate the potential and change its character relative to the neutral potential. We conclude with a brief discussion of how the formation of charged species in electron-

transfer reactions in the photosynthetic reaction center can trap the charged species and contribute to their high quantum efficiency.

Chapter 5 concludes this dissertation with a discussion of the van der Waals interaction in Zn^{II}-substituted cytochrome *c* (ZnCytc). We compare the vibrational coherence from the native and molten-globule states of ZnCytc In a protein environment, the van der Waals mode arises from interactions with nearby amino-acid residues. We examine how the potential is dominated by London-dispersion interactions, and how the absence of nearby polar or charged residues in the native state leads to inhomogeneous linebroadening of the van der Waals mode. In the molten-globule state, the protein core expands and the interactions are randomized. These factors effectively quench the van der Waals mode in the molten globule. We discuss how this result suggests that the van der Waals modes gain resonance Raman activity through direct attack of the nearby groups on the π-electron density of the chromophore. We conclude that the addition of charged or polar groups could tune the frequency of the van der Waals mode, and that similar interactions are likely candidates for the rate-controlling interactions in the photosynthetic reaction center.

CHAPTER 2

Vibrational Coherence and Photosynthetic Electron Transfer

Over the last 25 years, there has been an effort to design light-harvesting and electron-transfer molecular donor-acceptor systems for use in solar energy conversion applications.[5-17] A central design principle in this work has been to mimic various aspects of the structure and function of natural photosynthetic reaction centers, such as that from the purple non-sulfur bacteria.[8,10] The quantum efficiency of man-made systems falls far short of the essentially unity efficiency of the natural reaction center.[18,19] It is quite likely that what has not been mimicked so far is the structure and dynamics of the surrounding protein medium.

This dissertation describes an experimental study of how solvent structures around porphyrins in polar solutions and in a small redox protein are coupled to electronic transitions. The experiments employ a time-domain version of resonance Raman spectroscopy, dynamic-absorption spectroscopy. These studies provide the first detailed structural accounting for the vibrational motions that are coupled to the electron-transfer reactions in photosynthesis. In order to provide an introduction to these questions, the structure of electron transfer in photosynthesis is re-

viewed. Vibrational coherence and wavepacket generation are then discussed, and the dynamic-absorption pump-probe experiment is introduced. Observations of vibrational coherence first in the photosynthetic reaction center and then in myoglobin and cytochrome *c* will be reviewed. This chapter concludes with a review of the vibrational coherence observed from bacteriochlorophyll in polar solutions and in proteins.

2.1 Electron Transfer in Photosynthesis

The electron-transfer rate for the primary and secondary charge-separation reactions in the purple-bacterial photosynthetic reaction center is almost completely independent of temperature.[1,20] Figure 2.1 shows the rate constant as a function of temperature for the primary electron-transfer rate in the reaction center of *Blastochloris viridis*. The figure indicates that as the temperature increases, the reaction rate decreases: at room temperature, the primary electron transfer event takes approximately 3 ps, while at 10 K, the reaction time decreases to ~700 fs. This behavior defies the typical temperature dependence expected from the Arrhenius equation, $k = Ae^{-Ea/RT}$, where the rate k decreases as the temperature T increases.[21] This fact suggests that the electron-transfer reaction in the photosynthetic reaction center is nearly barrierless, so E_a is approximately 0. This both accounts for the rate behavior and for the long lifetimes of the non-neutral products: if the barrier is zero for the charge-separation reaction, then provided the reaction is enthalpically favored, the barrier for the charge-recombination reaction is high. Bixon and Jortner examined the case where vibrational modes of the solvent coupled to the electron transfer reaction.[1,22,23] In particular, for the case where the reaction is truly barrierless, or $E_a = 0$, the reaction rate k can be expressed as[1]

$$k = \frac{2\pi V^2}{\hbar^2 \omega (2p)^{1/2}} \left(\frac{e^{\hbar\omega/k_B T} - 1}{e^{\hbar\omega/k_B T} + 1} \right)^{1/2} \tag{2.1}$$

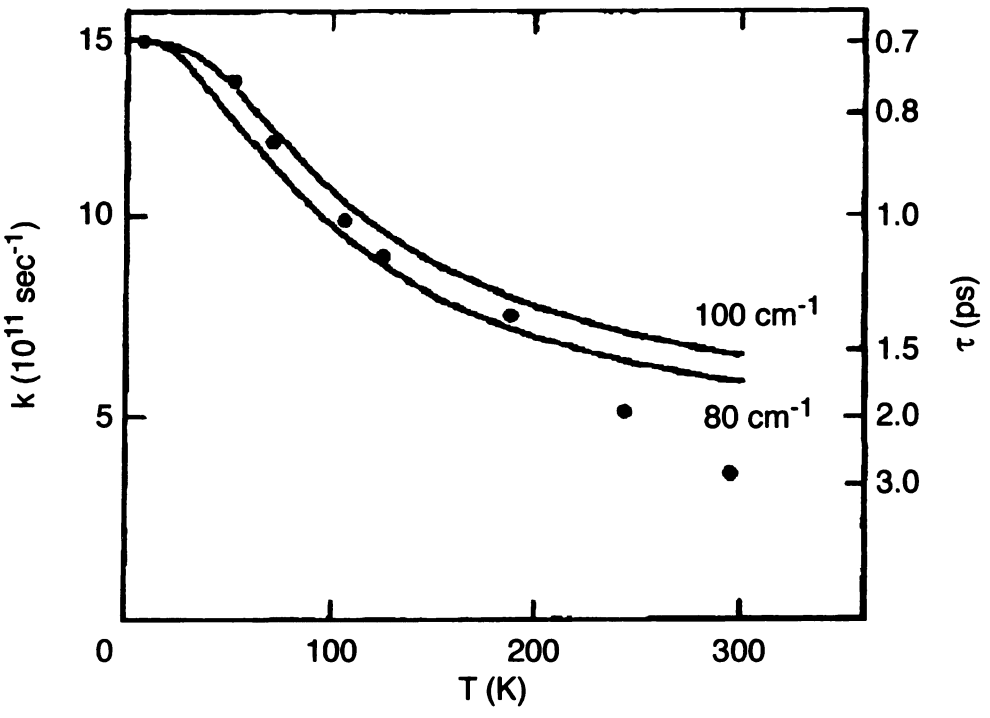

Figure 2.1. Temperature dependence of the primary electron transfer rate constant in the reaction center of *Blastochloris viridis.* (Adapted from reference 1.)

where V is the electronic coupling, ω is the vibrational frequency, $\hbar$ is Planck's constant divided by 2π and k_B is Boltzmann's constant.

From the Marcus theory for condensed-phase electron-transfer rates,[2-4] the activation energy for the electron-transfer reaction depends on both the driving force, the Gibbs free energy difference between the reactant and product ΔG^0, and the reorganization energy λ, the energy required by the reactant to assume the geometry of the product state. Under the Born-Oppenheimer approximation,[21] the reactant must reorganize before the electron transfer can occur. Figure 2.2 shows the reorganization energy for a model pair of non-adiabatic potential energy surfaces. A spontaneous reaction (for which ΔG^0 is negative) has a positive driving force. The activation energy is given by

$$E_a = \hbar\omega(p - S)^2/4S \tag{2.2}$$

Here, $p = \Delta G^0/\hbar\omega$, and $S = \lambda/\hbar\omega$. Since the rate constant is inversely proportional to the activation energy, it is clear from Equation 2.2 that for a given spontaneous reaction with a fixed $\Delta G^0<0$, the reaction rate will increase as the reorganization energy λ increases between 0 and ΔG^0. This is the so-called 'normal regime' in the Marcus theory.[4] As the reorganization increases beyond the driving force, the 'inverted regime', the reaction rate decreases. However, if the reorganization energy exactly matches the driving force, then the $(p - S)^2$ term in Equation 2.2 will become zero, so the reaction barrier will vanish. Bixon and Jortner observed that the relevant vibrational modes coupled to the electron transfer reaction that provided the bulk of the reorganization energy needed to match the driving force were in the ~100 cm^{-1} regime.[1,20,22] The structural origin of these low-frequency modes, however, was indeterminate.

The next section discusses how femtosecond spectroscopy can be used to monitor wavepacket motion on a potential energy surface. It also reviews the phenomenon

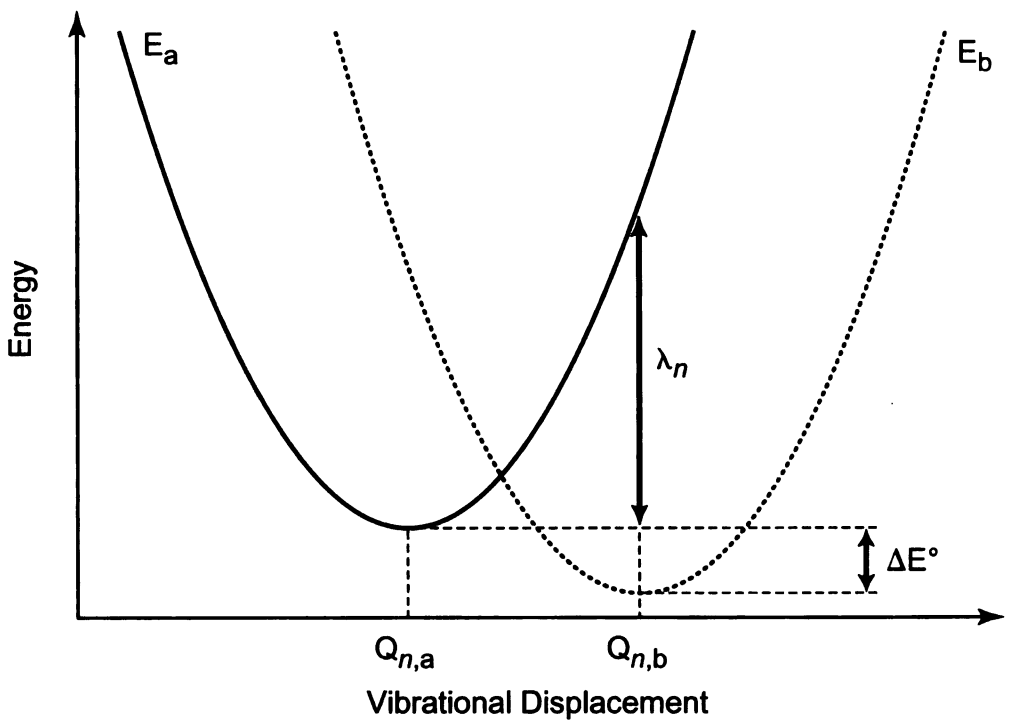

Figure 2.2. Driving force ΔE^0 and reorganization energy λ_n for a model pair of non-adiabatic potential energy surfaces, E_a and E_b. The driving force corresponds to the Gibbs free energy difference between the minimum of the potential wells between the reactant ($Q_{n,a}$) and product ($Q_{n,b}$) states. The reorganization energy is the difference between the minimum of the the potential well for the reactant and the energy of the reactant surface at the geometry of the product minimum.

of vibrational coherence. These two concepts form the basis of the femtosecond dynamic-absorption experiment, which is discussed later.

2.2 Vibrational Coherence and Wavepackets

Vibrational coherence arises from coherent wavepacket oscillation on a vibronic potential energy surface.[24-26] When a coherent pulse of light that is resonant with a vibronic transition hits a sample, it launches a wavepacket provided that the pulse is impulsive (*i.e.*, the duration of the pulse is shorter than the period of the vibrational mode).[27] The first and second actions of the electric field of the pump with the matter in the sample prepare a population in either the ground state or some resonant excited state.[25,26] Figure 2.3 shows the formation and motion of a wavepacket in the dynamic-absorption experiment. The excited-state potential energy surface $|e\rangle$ is displaced from the ground-state surface $|g\rangle$ in Figure 2.3. Because the two surfaces are displaced along the vibronic reaction coordinate, the potential is sloped in the Franck-Condon region. The slope of the potential surface generates a force on the wavepacket. This imparts momentum to the wavepacket, which will begin to move away from the Franck-Condon region[25,28,29] on either the ground or excited state. For the case of a ground-state wavepacket, this mechanism is analogous to resonance-Raman scattering.[25,26,30-33]

Following its formation, the wavepacket oscillates in the potential well. For a ground-state wavepacket, the duration of the pump pulse controls the displacement and momentum of the wavepacket. For a particular vibrational mode, the optimum pulse duration is approximately one-third of the mode's period. If the pulse is significantly shorter than the optimum duration, then the displacement away from the Franck-Condon region is small, and the experimentally detectable modulation by the wavepacket of a probe pulse is weak. If the pump pulse is too long, then it is no

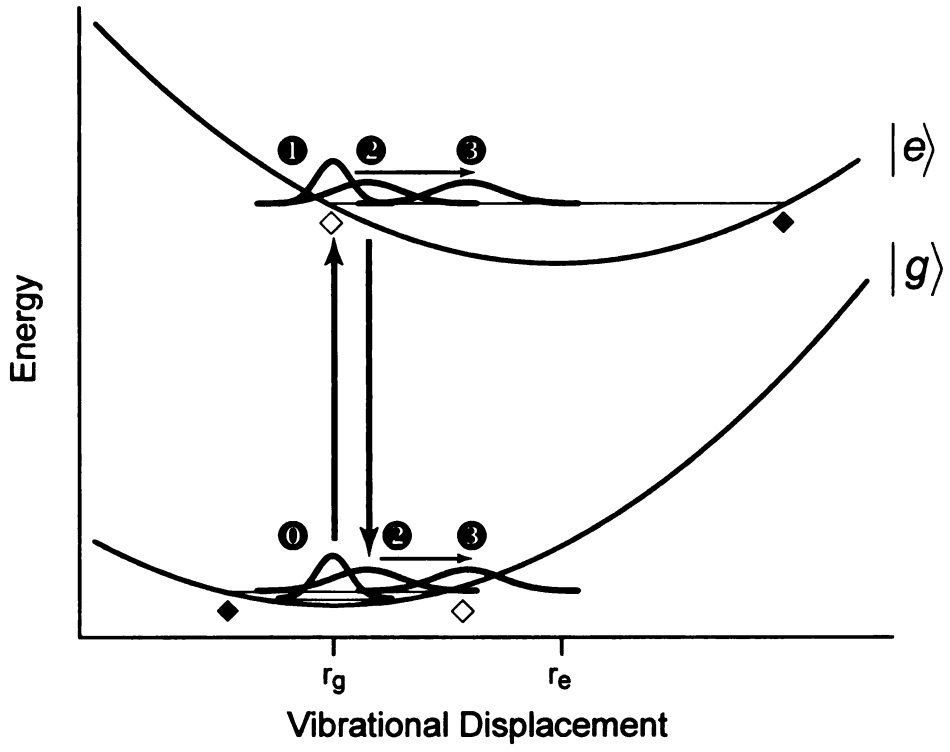

Figure 2.3. Excited-state and ground-state coherent wavepacket motion in the dynamic-absorption experiment. The excited-state ($|e\rangle$) and ground-state ($|g\rangle$) potential-energy surfaces are drawn as parabolas that are displaced with respect to a generalized multimode coordinate; r_g and r_e mark the equilibrium ground-state and excited-state geometries, respectively. Thick arrows represent the resonant pump-laser field; thin arrows show the direction that the wavepackets evolve during the first passage on the two surfaces. The numbers indicate event times, starting with the ground-state probability density (t = 0), creation of the excited-state wavepacket by the pump field (t = 1), creation of the ground-state wavepacket by the pump field (t = 2), and evolution during the first vibration (t = 3). The turning-point regions, where a wavepacket narrows and reverses its direction of motion, are marked on both surfaces with diamonds; white (unfilled) diamonds mark the turning points that contribute to the interference pattern in the dynamic absorption spectrum. (From reference 29.)

longer impulsive, so this too decreases the modulation intensity.[33] For an excited-state wavepacket, the intensity patterns are different. As long as the excited state is displaced from the ground state, the excited-state wavepacket will gain momentum if the pulse is impulsive. The strongest modulations will be those modes with the lowest frequency. The momentum of the wavepacket also trivially depends on the displacement of the excited state relative to the ground state. Not all modes are equally displaced; modes with a larger displacement will impart a greater momentum to the wavepacket than modes with a smaller displacement. The experimentally detectable modulation of a probe pulse will be greater for modes with larger displacements. The next section discusses the femtosecond dynamic-absorption pump-probe experiment, which can be used to monitor wavepacket motion and can generate information about the vibrational modes.

2.3 Dynamic-Absorption Spectroscopy

Vibrational coherence can be detected using the dynamic-absorption technique.[26,32,35-37] As the wavepacket oscillates back and forth in the potential well, changes in the transmitted intensity of a variably delayed probe pulse can be measured. As the wavepacket oscillates, it is only resonant with the probe pulse at a particular geometry of the vibronic displacement along the reaction coordinate. As the wavepacket moves on- and off-resonance with the probe bandwidth, the intensity of the transmitted probe pulse is modulated with the probe delay. When the wavepacket is on-resonance, the absorption of the sample increases, and the intensity of the transmitted probe beam decreases. When the wavepacket is off-resonance, the transmitted intensity increases. The dynamic-absorption pump-probe experiment monitors the intensity of the transmitted probe beam as a function of the variable probe delay. The resonant transitions generate an oscillatory signal in the time do-

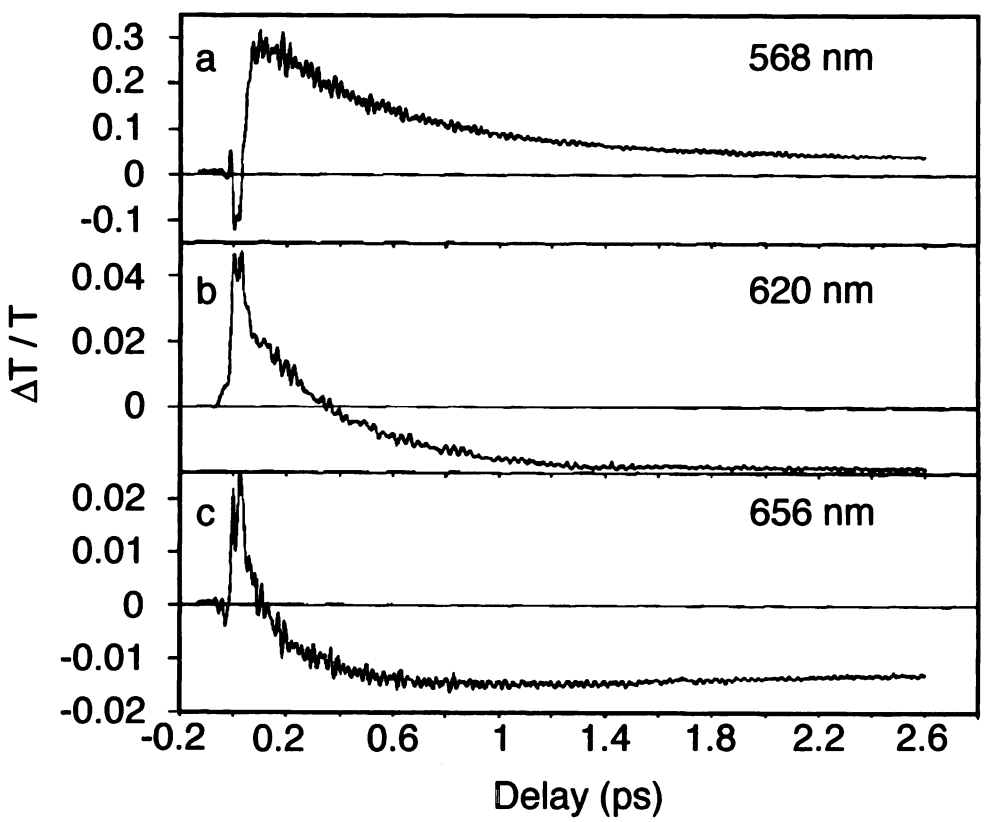

Figure 2.4. Femtosecond dynamic-absorption transients of bacteriorhodopsin. The laser spectrum was monitored at (a) 568 nm, (b) 620 nm, and (c) 656 nm probe wavelengths. (Adapted from reference 32.)

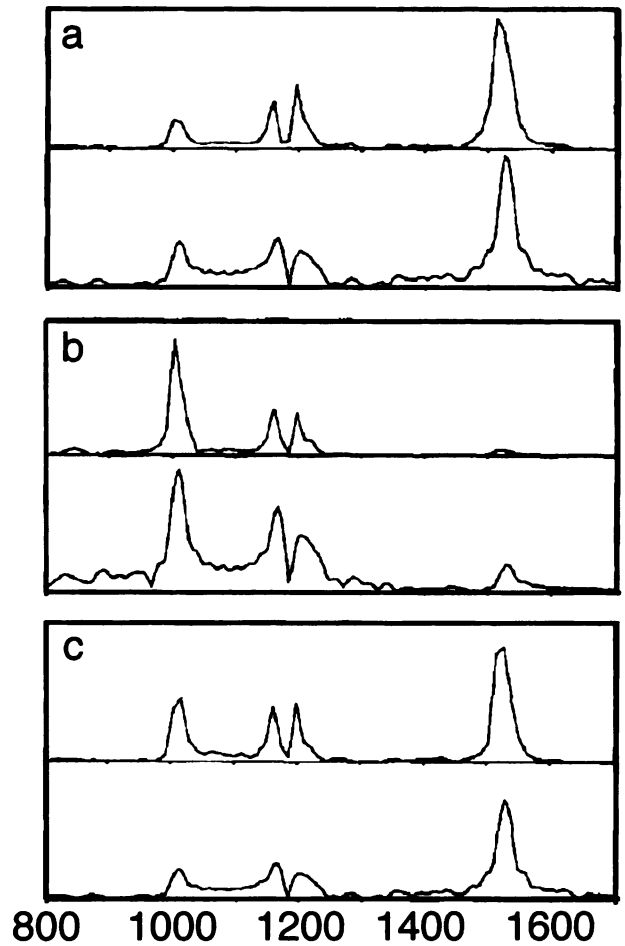

Figure 2.5. Fourier-transform spectra and model calculations of the oscillatory part of the pump-probe transients obtained from bacteriorhodopsin (see Figure 2.4). Panel a shows the spectrum obtained with a 568 nm probe wavelength and the 580 nm calculated spectrum. Panel b shows experimental and spectra at 620 nm. Panel c shows 656 nm experimental and 650 nm calculated spectra. The calculations used to generate the models are detailed in references 32, 33 and 34. (Adapted from reference 32.)

main that can be analyzed in the frequency domain to produce peaks corresponding to the coupled vibrational modes.

Early use of this technique included characterization of torsional motions in retinal that are associated with formation of the photoisomerization product state in bacteriorhodopsin and rhodopsin by Shank, Mathies and coworkers.[31-33,36,38-42] Figure 2.4 shows the dynamic-absorption transients obtained from bacteriorhodopsin using 12 fs excitation pulses by Shank and co-workers.[32] Following excitation by the pump-pulse, each transient exhibits a pattern of oscillations over at least the first picosecond. These oscillations correspond to the motions of the wavepacket described above. Fourier-transform spectra corresponding to the dynamic-absorption transients are shown in Figure 2.5. These spectra show peaks at 1010, 1160, 1200 and 1525 cm^{-1}. Below each experimental spectrum in the figure is a calculated model spectrum. The models exhibit good agreement with the experimental spectra. The peaks correspond to vibrational modes at those frequencies. The results are significant because they reveal the particular vibrational modes that are coupled to vibronic transition. This methodology is equally applicable to the vibrational modes coupled to the electron transfer reaction in the photosynthetic reaction center.

2.4 Vibrational Coherence in the Purple-Bacterial Photosynthetic Reaction Center

Vos, Martin and co-workers observed vibrational coherence in the photosynthetic reaction center of *Rhodobacter sphaeroides* R-26 following impulsive excitation of the primary electron donor, *P*. The vibrational coherence in the stimulated emission signal following excitation of the primary electron donor is primarily modulated primarily by low-frequency oscillations. The damping time of the vibrational coherence

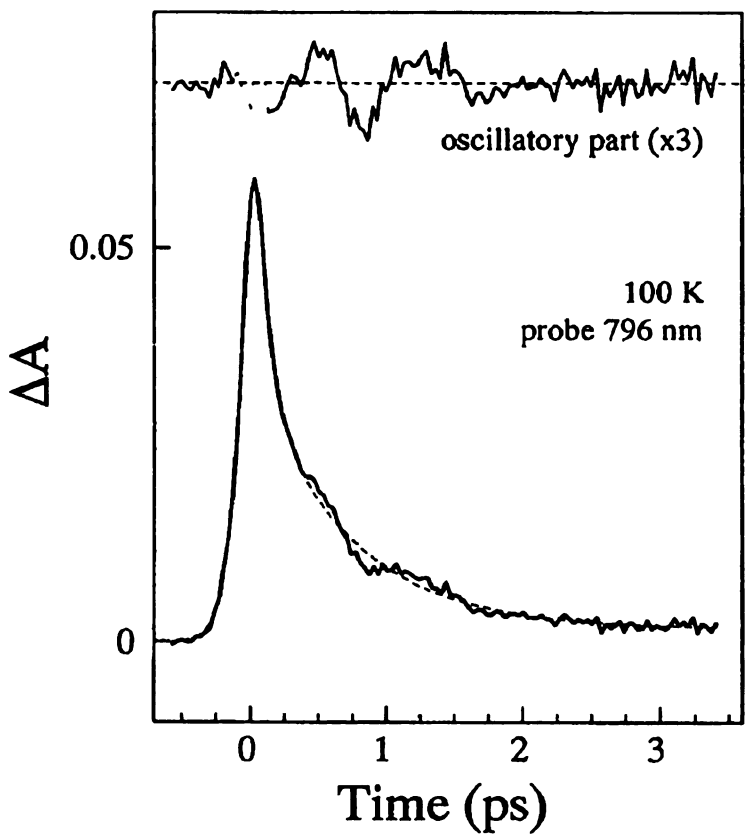

Figure 2.6. Dynamic-absorption transient from the reaction centers of *Rhodobacter sphaeroides* R-26 at 100 K. The oscillatory part of the signal is shown magnified ×3 above the transient. (From reference 43.)

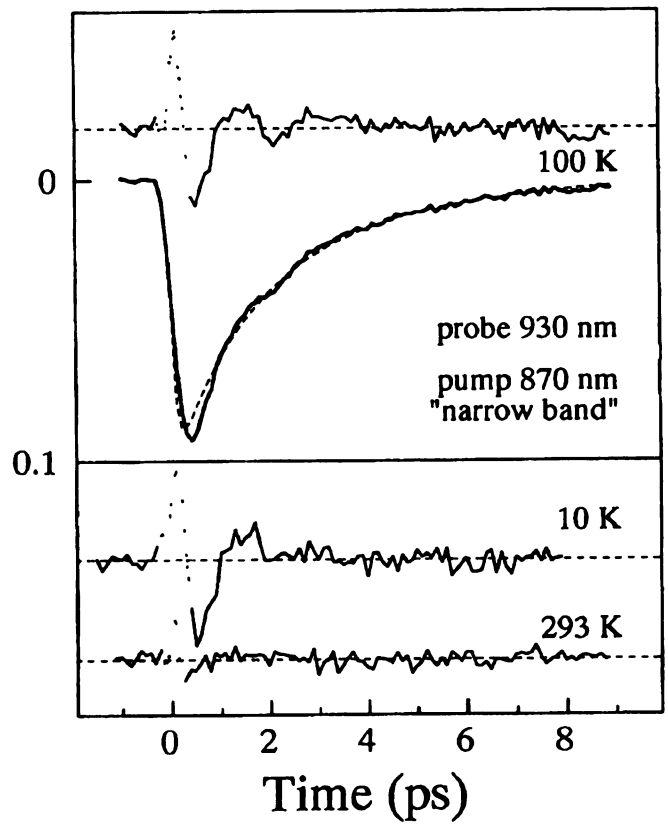

Figure 2.7. Dynamic-absorption transients at various temperatures of reaction centers of *Rhodobacter sphaeroides* R-26 at 100 K, 10 K, and 293 K. The oscillatory portions of the signals are shown magnified ×3 (normalized to the maximum signal at 100 K). (From reference 43.)

(<1 ps at 10 K) was on the same time scale as the primary electron transfer reaction. Moreover, the frequencies of these modes were in the 30-100 cm^{-1} regime.[43-51] A sample dynamic absorption transient from their early experiments[43] is presented in Figure 2.6. At 100 K, the strongest contribution to the oscillatory portion of the signal is a low-frequency mode with a period greater than 500 fs. At lower temperatures, the low-frequency components provide greater contributions to the overall vibrational coherence signal than at room temperature, as shown in Figure 2.7. The low-frequency components are perhaps an order of magnitude larger than any higher-frequency contributions. The low-frequency components are damped almost completely within the first two picoseconds. Vos, Martin and co-workers assigned these low-frequency vibrations to global modes of the protein medium.[43,52] These low-frequency modes are likely candidates for the modes that account for the majority of the reorganization energy in the charge-separation reactions in photosynthesis.

Subsequent experiments revealed strong components between 80 and 150 cm^{-1}, in addition to low frequency (15-80 cm^{-1}) modes.[47] The Fourier-transform spectrum from these experiments is shown in Figure 2.8 The top panel shows two strong features at 84 and 145 cm^{-1}, and a slightly weaker one at 192 cm^{-1}. The bottom panel shows a strong 30 cm^{-1} mode. The linewidths of these components are relatively broad, perhaps 50 cm^{-1} full-width at half-maximum (fwhm) for the 30-cm^{-1} and 145-cm^{-1} peaks. The low-frequency features were once again assigned to motions of the protein.[47,48] In particular, it was suggested that these low-frequency ~30 cm^{-1} modes were phonon-like in character, involving collective motions of the entire protein.[48-50] However, the frequency of these modes are much lower than the ~100 cm^{-1} modes that Bixon and Jortner suggested were coupled to the primary electron-transfer reaction.[1,22] However, Figure 2.8A also suggests the possible presence of a very broad (>100 cm^{-1} fwhm) component centered near 125 cm^{-1}. This feature was not discussed by the authors. The nature of the broad lineshape com-

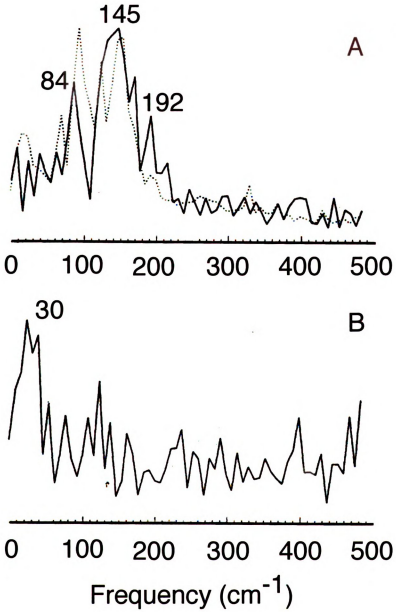

Figure 2.8. Fourier-transform spectra of the oscillatory parts of the pump-probe signals of the dynamic absorption transients of *Rhodobacter sphaeroides.* The pump-probe signals were obtained with pump pulses of 30 fs (A, solid curve) and 100 fs (B). For comparison, the same analysis for the data at 10 K (30-fs pump pulses) is shown (A, curve). (Adapted from reference 47.)

ponents in Zn^{II} porphyrins in polar solutions and in proteins is discussed heavily in Chapters 3-5. If the modes are not global motions of the protein, as suggested by Vos, Martin and co-workers, then the structural origin of the coupled modes is still indeterminate.

2.5 Vibrational Coherence from Myoglobin and Cytochrome *c*

Although they do not directly address the questions raised in the previous section, the pump-probe vibrational coherence experiments performed by Champion and co-workers are discussed here. Their experiments probe the vibrational coherence of the proteins cytochrome *c* (Cytc) and myoglobin (Mb). Both of these proteins contain a heme group,[53] similarly to bacteriochlorophyll, although the proteins studied by Champion typically contained iron as the metal ion bound to the porphyrin rather than magnesium. The Zn^{II}-substituted form of cytochrome *c* (ZnCytc), however shares some additional similarities to the magnesium-containing heme in bacteriochlorophyll. We examine the the vibrational coherence from ZnCytc in Chapter 5, and it grants crucial insight into the nature of the modes that are relevant to the electron-transfer reactions. The instrumental setup used by Champion and co-workers implements some novel design elements. We take advantage of similar techniques in our experiments discussed in Chapters 3-5. The results found by Champion and co-workers that are reviewed in this section revealed several low-frequency vibrational modes of the heme that provide a basis to which we later compare the results of the ZnCytc experiments in Chapter 5 These results are also significant because they demonstrate that skeletal normal modes of the porphyrin can be observed in the vibrational coherence.

The experiments by Champion and co-workers were performed using a Ti:sapphire laser to generate 45-120 fs pulses between 700 and 960 nm.[53-57] These pulses were frequency-doubled by a BBO crystal to generate blue pulses that could probe the Soret absorption band of the samples. A particularly novel approach used in these experiments was the use of spatially selective detection techniques that allowed a narrow region of the probe bandwidth to be analyzed.[55,56] This method could be used to selectively enhance the intensity of components in the vibrational coherence signals over certain ranges of frequencies compared to experiments where the entire probe bandwidth was integrated.[55,56] The narrow probe bandwidth enhances the modulation depth of the transmitted probe, which increases the signal quality and also enhances the detected intensity of certain modes. Data analysis was performed using linear predictive singular value decomposition (LPSVD) methods[58-60] to analyze the resulting pump-probe transients.[53] The LPSVD algorithm was used to generate frequency and damping time information for the various components from the overall vibrational coherence signal.

The most prominent vibrational modes consistently observed in the dynamic absorption signals, such as those shown in Figures 2.9 and 2.10, were near 40 and 80 cm^{-1}.[54,56,57,61,62] Figure 2.9 shows the dynamic-absorption transients and corresponding LPSVD spectra from MbNO. The most intense components in the spectra are the low-frequency oscillations. They are up to an order of magnitude stronger than any of the high-frequency components. Figure 2.10 shows the transients and LPSVD spectra from ferrous cytochrome *c* (FeCytc). Similarly to MbNO, the most intense components are the from the low-frequency ~40-cm^{-1} and ~80-cm^{-1} modes. The observed frequencies are somewhat higher in FeCytc than in MbNO. The 40-cm^{-1} mode was assigned to doming motions of the central metal ion in the heme, while the 80-cm^{-1} mode was assigned to an overtone of the doming mode.[57] A relatively high-frequency mode near 220 cm^{-1} was also reported. This mode was assigned to a

metal-doming mode involving the metal ion and one of its axial ligands.[57] In particular, for the case of FeCytc, this mode was assigned to the stretch between the metal ion and its axial His-18 ligand.[54] While typically weaker than the doming modes, this mode was consistently observed in both myoglobin and cytochrome *c*.[54,57,61] These results are important for comparison to our later experiments on Zn^{II} *meso*-tetrakis(N-methylpyridyl)porphyrin (ZnTMPyP) in Chapters 3 and 4 and also in particular to our experiments on ZnCytc in Chapter 5.

While the results reported by Champion and co-workers give very good results for the slowly damped features in the vibrational coherence, they do not address any rapidly damped features. The focus of the experiments was on the origin of the low-frequency components near 40 cm^{-1}, but additional features in the vibrational coherence can be observed. In particular, a direct comparison of a Fourier-transform spectrum and LPSVD fit of a pump-probe transient obtained from deoxymyoglobin reveals a broad component near 300 cm^{-1} in the Fourier-transform spectrum and LPSVD analysis,[53] as shown in Figure 2.11 that is not directly addressed by the authors. Figure 2.11 shows the dynamic-absorption transient of deoxyMB; Panel b reveals a broad background centered near 300 cm^{-1} that underlies the narrower components. This lineshape is similar to that discussed earlier from the vibrational coherence from the reaction center of *Rhodobacter sphaeroides* (see Figure 2.8). Similar features can be seen in Figures 2.9 and 2.10. In each case, the broad portion of the broad background has superimposed narrower components. The broad lineshape is characteristic of a rapidly damped feature in the time domain. The vibrational modes corresponding to these features likely play a critical role in the previously discussed electron transfer reactions in the photosynthetic reaction center.

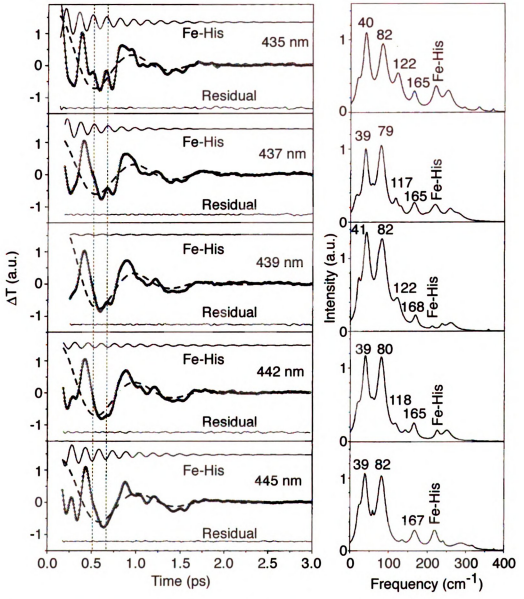

Figure 2.9. Open band femtosecond dynamic-absorption spectroscopy measurements on MbNO samples. The left panels present the oscillatory parts of the the pump-probe signals (circles) with their LPSVD fits (solid line). The 40 cm^{-1} component (dashed line) is superimposed on the oscillatory signal and the 220 cm^{-1} mode shown is shifted for clarity (thin solid line). The right panels show the LPSVD-generated power spectra. (Adapted from reference 54.)

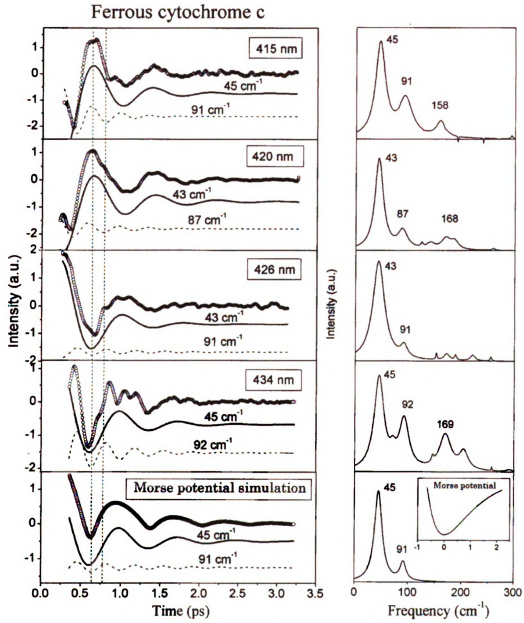

Figure 2.10. Sequence of dynamic-absorption transients using the open band detection scheme on FeCytc. The left panels present the oscillatory part of the signal, and the right panels show the corresponding power spectra. The ~45 cm^{-1} oscillation (solid line and the ~91 nw oscillation (dashed line) used in the fit are shown displaced from the data. The inset in the lower-right panel displays the Morse potential used in the simulation. (Adapted from reference 57.)

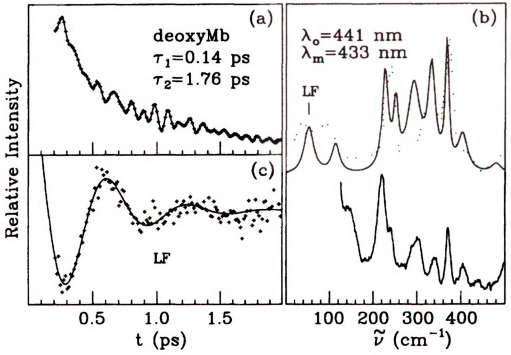

Figure 2.11. Femtosecond dynamic-absorption transients of deoxyMb. The signal (a) is shown along with the LPSVD fit (solid line). The discrete Fourier transform amplitudes (dotted line) and the power spectrum derived from the LPSVD analysis (upper solid line) (b) are compared with the resonance Raman spectrum (lower solid line). The low frequency residual (c) is superimposed with the LPSVD fit that describes its oscillation and decay. (From reference 53.)

2.6 Vibrational Coherence in Bacteriochlorophyll Solutions and Proteins

The experiments that will be discussed in Chapters 3-5 were inspired by work from this laboratory on bacteriochlorophyll *a* (BChl) that suggested a new interpretation for the structural origin of the ~100 cm^{-1} modes coupled to the electron transfer reactions in the photosynthetic reaction center. The results of the experiments suggested that these modes arise from *intermolecular* interactions between the chromophore and the solvent or surrounding protein medium. Experiments on BChl *a* in polar solutions revealed that the vibrational coherence was dominated by rapidly damped modes. These modes exhibited a shift in frequency with a greater than quadratic dependence on the solvent dipole moment. This behavior was consistent with a van der Waals intermolecular potential.[63] Additional experiments on the light-harvesting subunit proteins B777 and B820 revealed that direct attack on the π-electron density of the chromophore by the solvent appeared to be necessary for the intermolecular mode to gain resonance Raman activity. Although the later experimental chapters cover this work in more detail, in the following the main ideas are reviewed.

2.6.1 Vibrational Coherence in Bacteriochlorophyll *a* in Polar solution

Pump-probe experiments with *Q*-band excitation on BChl *a* in pyridine solution revealed two distinct types of components in the low-frequency vibrational coherence.[64] The first were a set of slowly damped components that persisted out to 8 ps. These components had frequencies over a range of 11-206 cm^{-1}; their damping times γ ranged from 800 fs to 1.7 ps. In addition to these components, a very strong, rapidly damped feature was also observed. This component had a much shorter

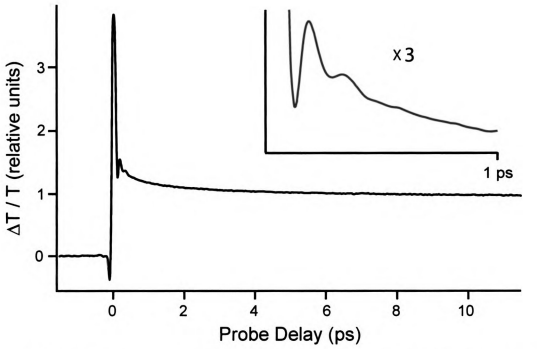

Figure 2.12. Dynamic-absorption transient from BChl *a* in pyridine. The inset shows a magnified view of the first picosecond of the signal. (From reference 63.)

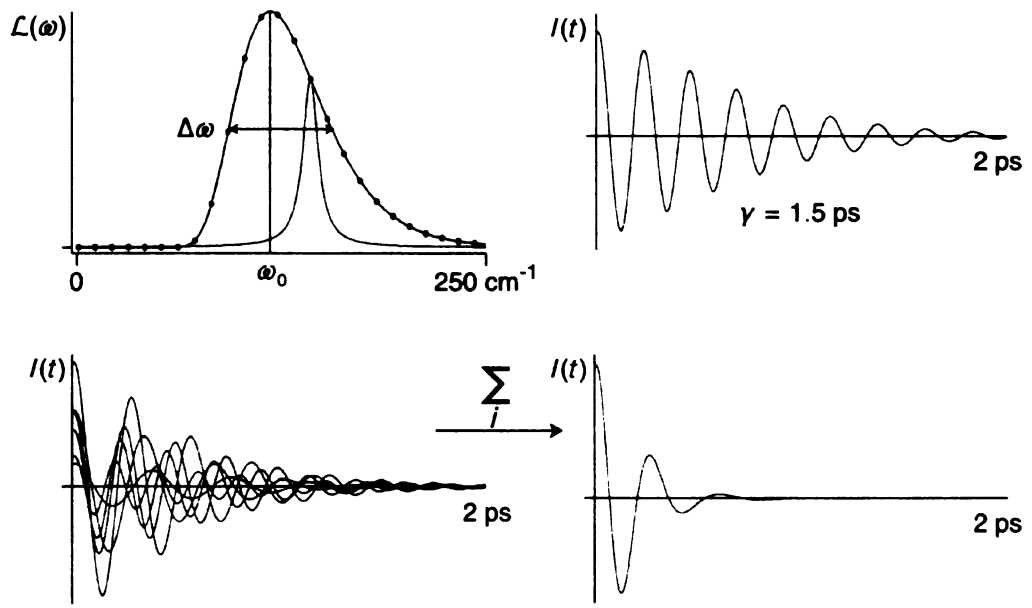

Figure 2.13. Model of the rapidly damped vibrational coherence observed in BChl *a* solutions as a distribution of damped cosinusoids, $\mathcal{L}(\omega)$. A log-normal distribution $\mathcal{L}$ (a), defined by its center frequency ω_0, width $\Delta\omega$ and asymmetry (or skew) ρ, sampled over its full width. Each sample Lorentzian lineshape has its own center frequency ω_{0i}, and corresponds in the time domain to an exponentially damped cosinusoid in the time domain (b) with an intrinsic damping time γ. Summing the set of Lorentzians obtained by sampling over the full width of the log-normal distribution $\mathcal{L}(\omega)$ (c) results in a superposition whose rapidly damped waveform (d) resembles the vibrational coherence observed in BChl solutions. (Adapted from reference 63.)

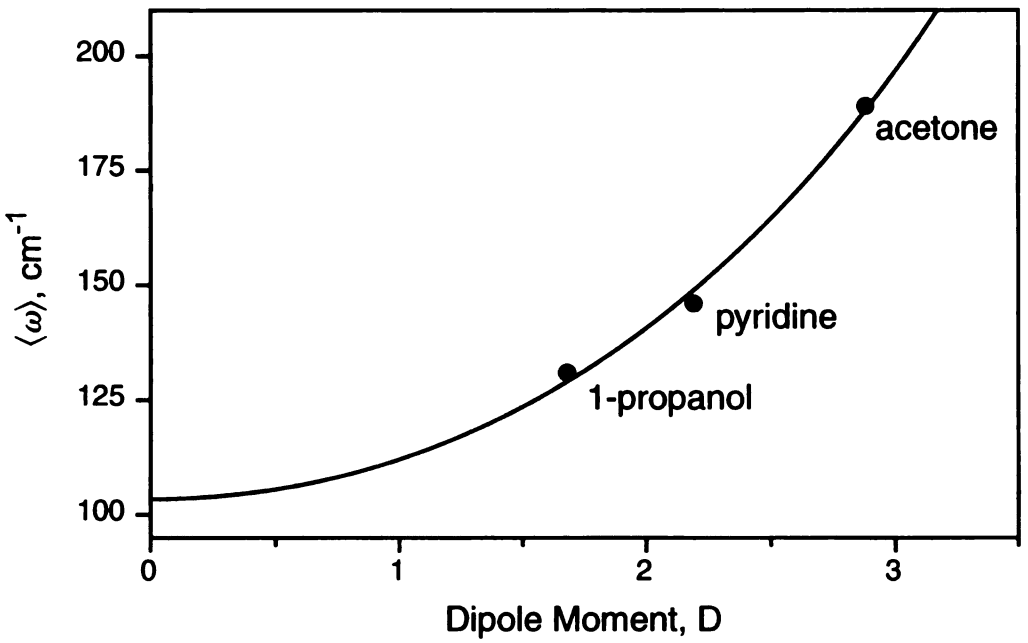

Figure 2.14. Solvent dependence of the mean frequency $\langle\omega\rangle$ of the rapidly damped vibrational coherence observed in BChl *a* solutions in a range of polar solvents on the solvent dipole moment. The data points are superimposed on a model curve derived from an expression for the natural frequency for a 6-12 intermolecular potential for the BChl-solvent mode. The expressions for the intermolecular potential and natural frequency are detailed in reference 63 and in Chapters 3-5 (From reference 63.)

damping time (200 fs), and dominated the early-time portion of the transient absorption signal. It was suggested that this 155 cm^{-1} mode was due to an intermolecular interaction between BChl and a pyridine molecule in the first solvation shell.

Subsequent experiments were performed by Katherine Shelly on BChl *a* in a series of polar solvents.[63] The observed vibrational coherence was again dominated by rapidly damped components (see Figure 2.12). The figure shows the dynamic-absorption transient from BChl *a* in pyridine solution. By far the strongest feature in the vibrational coherence is a rapidly damped component, which is shown in the inset of Figure 2.12. This feature is almost completely damped within the first 500 fs, but it is at least an order of magnitude larger than any other oscillatory component. The lineshapes corresponding to the rapidly damped components exhibited behavior consistent with the superposition of several Lorentzian lineshapes with a distribution of frequencies (see Figure 2.13). In such a picture, the overall lognormal distribution shown in Figure 2.13a arises from the sum of individual Lorentzian lineshapes. This behavior is consistent with a picture where the rapid damping times are due to inhomogeneous line broadening. The individual Lorentzians correspond to the lineshape generated by a single molecule. The local variations between different molecules in the ensemble generate slightly different frequencies. The time-domain superposition of these individual waveforms is a rapidly damped oscillation. The rapidly damped components also exhibited a solvent-dependent frequency shift. The shift followed a trend consistent with a van der Waals intermolecular potential between the chromophore and a nearby solvent molecule (see Figure 2.14). The van der Waals potential is discussed in detail in the experimental chapters 3-5. The frequency of the rapidly damped mode increased with a greater than quadratic dependence on the dipole moment of the solvent. The intermolecular potential was dominated by dipole-dipole interactions. In the nonpolar solvent limit, the mean frequency of the rapidly damped vibrational coherence was extrapolated to be ~100 cm^{-1}. The results further sug-

gested that interactions between the chromophore and clustered, first-shell solvent molecules dominated the low-frequency vibrational coherence. This conclusion provides the movitvation for much of the work that follows in this dissertation.

2.6.2 Intermolecular Vibrational Coherence From B777 and B820

Additional experiments on the light-harvesting subunit proteins B777 and B820 yielded similar results.[65] B820 is a dimer containing a pair of BChl macrocycles (see Figure 2.15). In the purple-bacterial LH1 light-harvesting complex, 15 B820 subunits combine to form a ring around the photosynthetic reaction center.[66] The monomer that pairs to form B820 is known as B777.[67-71] In B777, a single BChl macrocycle binds to an α helix by coordinating the Mg^{II} ion to a histidine residue.[67,72] In the monomeric form, the BChl is directly exposed to the solvent. In B820, the BChl macrocycles form a van der Waals complex. Figure 2.15 shows that in the complex, the BChl macrocycles directly face each other. In this configuration, the macrocyles resemble the special pair in the primary electron donor *P* in the photosynthetic reaction center.[65,73,74]

In B777, the vibrational coherence strongly resembled that of BChl in acetone from the earlier experiments (see Figures 2.16 and 2.17). The rapidly damped portion of the signal was much more intense than the more slowly damped oscillations. The rapidly damped feature could be modeled as the sum of two components. These components were assigned to hindered translational and rotational (librations) modes between the porphyrin chromophore and one of the surrounding solvent molecules.[63,65] In B820, the vibrational coherence, while still dominated by rapidly damped components, was significantly weaker (see Figure 2.18) than in B777. The frequencies of the rapidly damped components were also lowered. These results were consistent with an assignment of the rapidly damped vibrational coherence to intermolecular vibrational modes. In the monomeric B777 direct attack on the π-

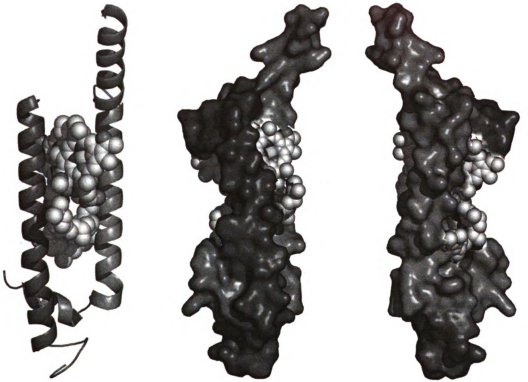

Figure 2.15. The Hu and Schulten[75] model for the B820 subunit in LH1 from *Rhodobacter sphaeroides*, showing the pair of BChl macrocycles and the transmembrane α helices in ribbon and surface renderings. (From reference 65.)

electron density of the chromophore is possible. The B820 dimer, however, shields the chromophore because the BChl macrocycles are paired. As a result, the strength of the intermolecular interaction is significantly attenuated. Additional interactions between the BChl macrocycle and a nearby tryptophan residue and BChl-BChl interactions were also observed in B820. The results further advanced the hypothesis that the intermolecular vibrational modes are the dominant ones in the low-frequency vibrational coherence. They also suggested a mechanism for gaining resonance Raman activity: direct attack on the π-electron density of the chromophore.

2.7 Proposed Experiments

The results from this work on BChl *a*, B777 and B820 suggest further experiments to clarify the nature of this intermolecular vibrational mode. These results suggest that the vibrational coherence from BChl is dominated by intermolecular modes with a clustered, first-shell solvent molecules that attack the π-electron density of the BChl macrocycle. This result should be generalizable to other π-electron containing systems, such as a porphyrin. It is not clear, however, that the intermolecular mode from BChl in polar solution is fully understood; the vibrational coherence lacks normal intramolecular (skeletal) vibrational modes of the porphyrin chromophore. The relative resonance Raman activities of the intramolecular and intermolecular modes cannot be directly compared. In order to compare the two types of modes, both must be present in the vibrational coherence. By varying the solvent environment, the intermolecular van der Waals modes can be distinguished. The Soret-band excitation experiments performed by Champion and co-workers on myoglobin and cytochrome *c* revealed the presence of several skeletal modes in the vibrational coherence,[53-57] so they suggest that other porphyrins or porphyrin-containing proteins might make good candidates for further study.

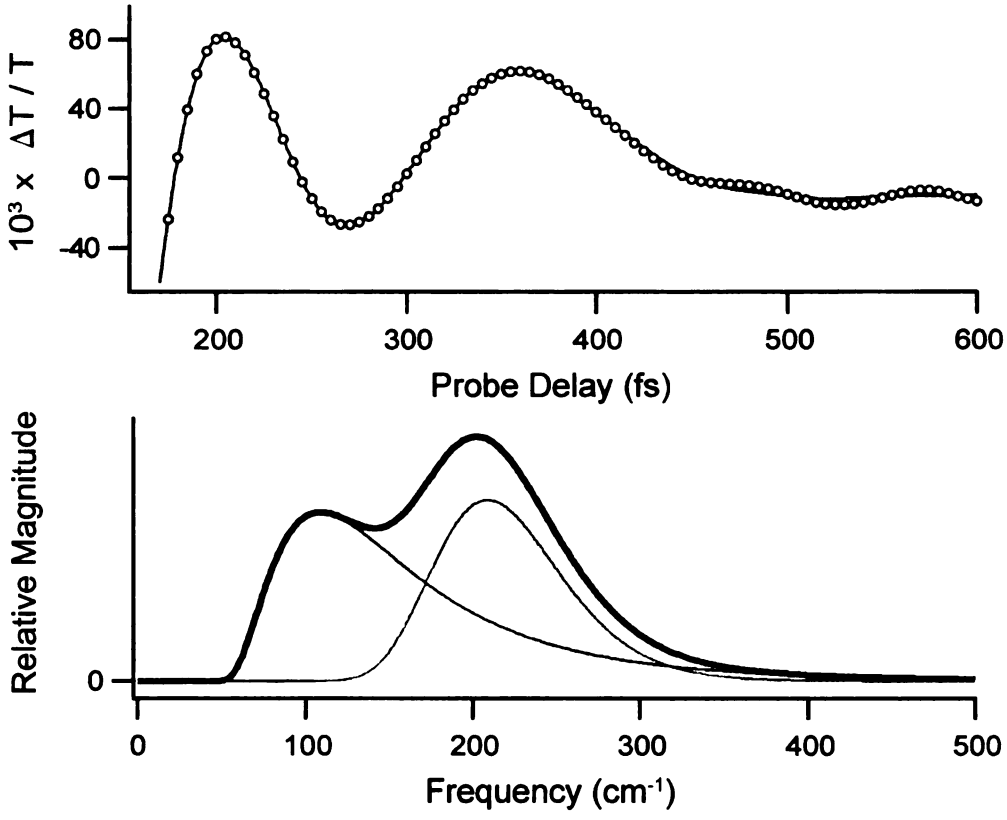

Figure 2.16. Expanded view of the rapidly damped oscillation observed in the dynamic-absorption transient from BChl *a* in acetone. The signal is superimposed with a model defined by the sum of two independent log-normal distributions $\mathcal{L}(\omega)$ of damped cosinusoids. The scaling of the ordinate is relative to the magnitude of the pump-probe ground-state depletion signal. Bottom: Plots of $\mathcal{L}(\omega)$ for the two components observed in acetone and their sum $\mathcal{M}(\omega)$ (thick curve). (From reference 63.)

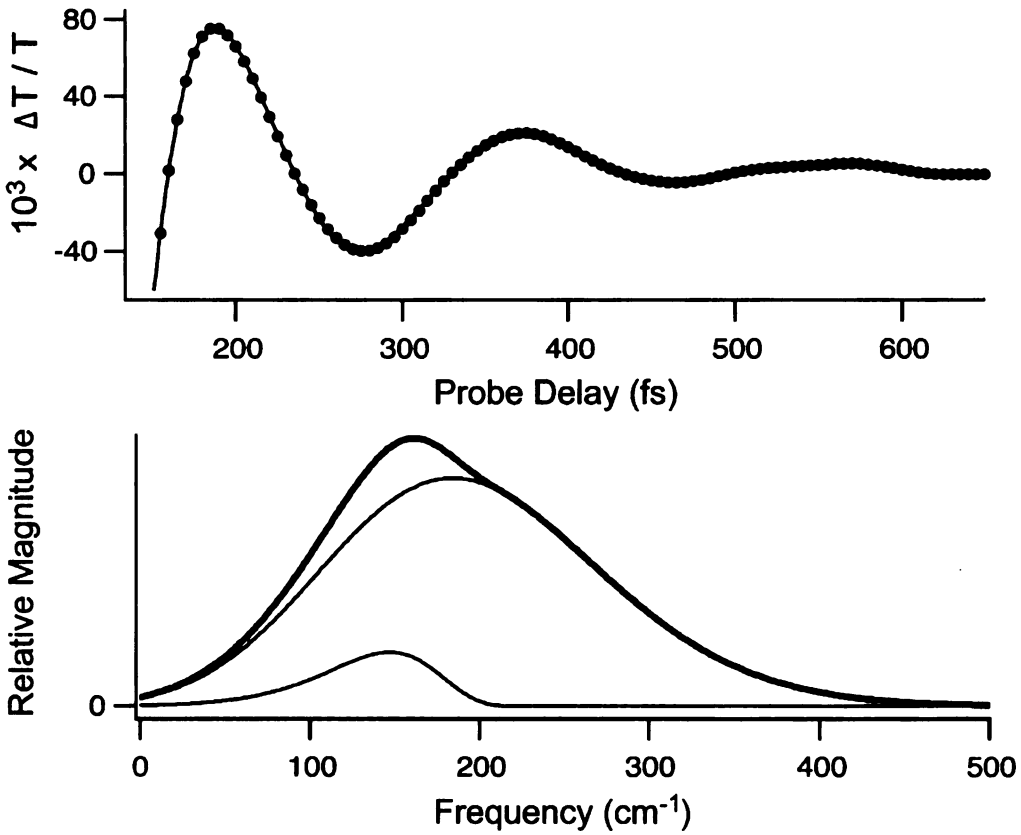

Figure 2.17. Expanded view of the rapidly damped oscillation observed in the dynamic-absorption transient from B777. The signal is superimposed with a model defined by the sum of two independent log-normal distributions $\mathcal{L}(\omega)$ of damped cosinusoids. The scaling of the ordinate is relative to the magnitude of the pump-probe ground-state depletion signal. Bottom: Plots of $\mathcal{L}(\omega)$ for the two components observed in B777 and their sum $\mathcal{M}(\omega)$ (thick curve). (From reference 65.)

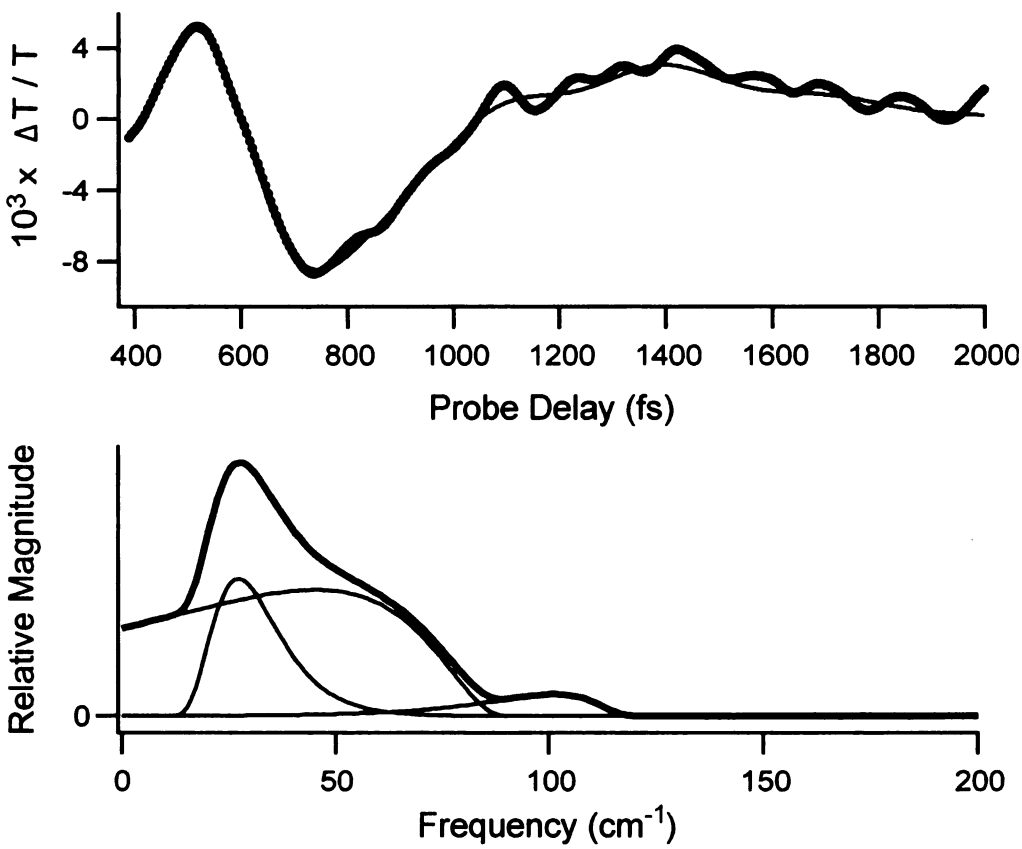

Figure 2.18. Expanded view of the rapidly damped oscillation observed in the dynamic-absorption transient from B820. The signal is superimposed with a model defined by the sum of two independent log-normal distributions $\mathcal{L}(\omega)$ of damped cosinusoids. The scaling of the ordinate is relative to the magnitude of the pump-probe ground-state depletion signal. Bottom: Plots of $\mathcal{L}(\omega)$ for the two components observed in B820 and their sum $\mathcal{M}(\omega)$ (thick curve). (From reference 65.)

We can examine the vibrational coherence from Zn^{II} *meso*-tetrakis(N-methylpyridyl)porphyrin (ZnTMPyP) in a series of polar solutions. These experiments use Soret-band excitation, so they monitor the ground-state vibrational coherence of ZnTMPyP in analogy to the experiments on BChl. By varying the dipole moment of the solvent, we can look for changes in the mean frequency of the rapidly damped mode. We can also compare the vibrational coherence from ZnTMPyP in methanol and perdeuturated methanol solutions to search for evidence of an isotpe effect. ZnTMPyP has a small permanent dipole moment compared to BChl, so the frequency of the rapidly damped mode should be smaller than that observed in the vibrational coherence from BChl solution. The rapidly damped vibrational coherence should still exhibit a solvent dependent shift, and it should be more intense than the slowly damped skeletal modes.

The stimulated-emission experiments by Vos, Martin and co-workers on photosynthetic reaction centers monitored vibrational coherence from the excited state.[45-48,50,51,76] By tuning the laser Q-band of the absorption spectrum, the vibrational coherence from the excited state ZnTMPyP can be similarly monitored. In the excited state, the π-electron density of ZnTMPyP extends over the N-methylpyridyl rings, so the van der Waals intermolecular potential senses charges on the porphyrin. The addition of charges to the intermolecular potential should have a significant effect on the frequency of the intermolecular mode.

We cannot fully characterize the behavior of the van der Waals mode in a protein environment from the B777 and B820 experiments. In B777, the BChl macrocycle is directly exposed to the solvent, while in B820 the BChl forms a dimer to provide shelter from the solvent. A monomeric porphyrin in the interior of a protein may behave differently. The issue of which amino-acid residues in the protein couple to the $\pi \rightarrow \pi^*$ transition of the porphyrin macrocycle must be considered. In a protein such as Zn^{II} cytochrome c (ZnCytc), we can compare the vibrational coherence from

the native and molten-globule states to test the response of the van der Waals mode to a change in the local environment of the porphyrin. The following chapters will address these issues.

CHAPTER 3

Ground-state vibrational coherence in polar solutions of Zn^{II} tetrakis(N-methylpyridyl)porphyrin with Soret-band excitation

3.1 Summary

Ground-state coherent wavepacket motions arising from intermolecular modes with clustered, first-shell solvent molecules were observed using the femtosecond dynamic absorption technique in polar solutions of Zn^{II} *meso*-tetrakis(N-methylpyridyl)porphyrin (ZnTMPyP) with excitation in the Soret absorption band. As was observed previously in bacteriochlorophyll *a* solution, the pump-probe transients in ZnTMPyP solutions are weakly modulated by slowly damped (effective damping time $\gamma > 1$ ps) features that are assigned to intramolecular modes, the skeletal normal modes of vibration of the porphyrin. The 40-cm^{-1} and 215-cm^{-1} modes from the metal-doming and metal–solvent-ligand modes, respectively, are members

of this set of modulation components. A slowly damped 2-4-cm^{-1} component is assigned to the internal rotation of the N-methylpyridyl rings with respect to the porphyrin macrocycle; this mode obtains strong resonance Raman intensity enhancement from an extensive delocalization of π-electron density from the porphyrin in the ground state onto the rings in the π^* excited states. The dominant features observed in the pump-probe transients are a pair of rapidly damped (γ < 250 fs) modulation components arising from intermolecular modes with solvent molecules. This structural assignment is supported by an isotope shift of the average mode frequencies in methanol and perdeuterated methanol. The solvent dependence of the mean intermolecular mode frequency is consistent with a van der Waals intermolecular potential that has significant contributions only from the London dispersion and induction interactions; ion-dipole or ion-induced-dipole terms do not make large contributions because the π-electron density is not extensively delocalized onto the N-methylpyridyl rings. The modulation depth associated with the intermolecular modes exhibits a marked dependence on the electronic structure of the solvent that is probably related to the degree of covalency; the strongest modulations are observed in acetonitrile and dimethylsulfoxide. The results strongly support a structural assignment of the low-frequency modes that are coupled to the primary and secondary electron-transfer reactions in photosynthetic reaction centers to intermolecular modes between the redox-active chromophores and first-solvation shell groups from the surrounding protein, and an important additional function of the intermolecular modes in the stabilization of charged intermediates is suggested.

3.2 Introduction

In the purple-bacterial photosynthetic reaction center, the primary and secondary charge-separation reactions exhibit effectively activationless dynamics ow-

ing to coupling to low-frequency vibrational modes in the 100-cm^{-1} regime.[1,20,22] The main components detected in the vibrational coherence observed in pump-probe[43-46,48-51,76] and fluorescence upconversion[77] transients following impulsive excitation of the primary electron donor, *P*, are modes with frequencies in the 30-100-cm^{-1} range. The possibility that the modes observed in the vibrational coherence are the ones that are coupled to the electron-transfer reaction coordinate has been discussed,[49,78-84] but their structural origin remains indeterminate. Bixon and Jortner[1,20,22] attributed the coupled modes to the protein medium, and Vos, Martin, and coworkers suggested that the modes that are active in the vibrational coherence are delocalized or phonon-like in character.[45,50]

In recent work, the Beck laboratory has advanced an alternative hypothesis that the vibrational modes that control the electron-transfer dynamics in reaction centers are *intermolecular* in origin, between the redox-active chromophores and groups in the first-solvation shell from the surrounding protein medium. This hypothesis is supported by our observations using femtosecond pump-probe spectroscopy of the rapidly damped low-frequency vibrational coherence from bacteriochlorophyll *a* (BChl) in polar solution[63,64] and in the light-harvesting subunit proteins B777 and B820.[65] In solution, BChl exhibits a slowly damped set of modulations over the 100-8000-fs probe delay range; these components exhibit damping times in the >1-ps regime and mode frequencies ranging from 10-220-cm^{-1}. The magnitude spectrum obtained by Fourier transformation is comparable to the low-frequency region of the conventional resonance Raman spectrum from BChl in solution, in films, and in the reaction center,[85,86] so these slowly damped features are assigned to the low-frequency skeletal modes of the BChl macrocycle.[64] By far the strongest features in the vibrational coherence from BChl solutions, however, are a very rapidly damped set of modulation components in the sub-ps time scale. These features are well described by time-domain models that correspond in the frequency domain to inhomo-

geneously broadened lineshapes with very broad, asymmetric Gaussian profiles. The mean frequency of the rapidly damped vibrational coherence exhibits a greater than quadratic dependence on the gas-phase dipole moment of the solvent. This trend is consistent with a van der Waals intermolecular potential in which the London-dispersion and dipole–dipole interactions make large contributions; the extrapolated 100-cm^{-1} frequency in the nonpolar limit arises predominantly from the London-dispersion term.[63] The rapidly damped vibrational coherence observed in the B777 system is comparable to that observed with BChl in acetone solution because the BChl macrocycles are exposed to the polar head groups of the surrounding nonionic detergent. In the paired BChl system called B820 that forms when two B777 monomers associate, however, the supporting α helices sterically protect the BChl macrocycles from direct attack by the surrounding detergent. The vibrational coherence then reveals weaker and more slowly damped components at 28 cm^{-1} and 46 cm^{-1} that are assigned to BChl–tryptophan and BChl–BChl intermolecular modes.[65]

The intermolecular modes that contribute to the vibrational coherence in BChl-containing systems modulate the pump-probe ground-state depletion signal owing to the resonant impulsive stimulated Raman scattering (RISRS) mechanism.[24-26,30,32,33] It was suggested that these modes are resonance Raman active because molecules in the first solvation shell make a direct attack on the π-electron density above and below the macrocycle and are displaced by the $\pi \rightarrow \pi^*$ transition.[63,65] This hypothesis suggests that the spatial organization of the π-electron density in the ground state selects the first-shell solvent molecules that contribute to the vibrational coherence. As a test of these ideas, we discuss in this chapter the low-frequency ground-state vibrational coherence in polar solutions of Zn^{II} *meso*-tetrakis(N-methylpyridyl)porphyrin (ZnTMPyP, see Figure 3.1). Owing to the nominal C_4 symmetry axis normal to the macrocycle, ZnTMPyP has a small net dipole moment; with a single methanol (CH_3OH) axially ligated to the Zn^{II} ion, the calculated

dipole moment is only 0.66 D (see Figure 3.1). ZnTMPyP is nevertheless soluble in a range of polar solvents because the peripheral N-methylpyridyl rings each carry a positive charge. Because the π-electron density in the ground state (see Figure 3.1a) is mostly confined to the region of the porphyrin, however, the resonance Raman active solvent molecules are effectively held at some distance from the peripheral charges, so charge-dependent terms will make only a small contribution to the intermolecular potential. In short, the ground-state intermolecular mode frequency in ZnTMPyP solution should be smaller than detected in the same solvents in BChl solution because the only terms in the intermolecular potential that will make large contributions are those that depend on the polarizability of the porphyrin: the London-dispersion and solvent-dipole–induced-dipole terms.

The results show that the vibrational coherence from ZnTMPyP detected with Soret-band excitation contains dominant contributions from rapidly damped features arising from intermolecular modes with clustered solvent molecules. The components arising from intramolecular modes, from the porphyrin macrocycle proper or from the metal–axial-ligand interaction, can be distinguished from the intermolecular modes because they exhibit long damping times and narrow lineshapes. The intermolecular mode frequency follows the expected dependence on the solvent's dipole moment; the 70-cm^{-1} frequency in the nonpolar limit and the observation of a isotope shift in perdeuterated methanol are consistent with the hypothesis discussed above. In addition to supporting a structural assignment of the low-frequency modes that are coupled to the electron-transfer reactions in photosynthetic reaction centers, the results have additional significance because they suggest a role for intermolecular modes in the stabilization of charged intermediates in redox catalysis in proteins. The results described in this chapter were previously published in the *Journal of Physical Chemistry* (see reference 88.)

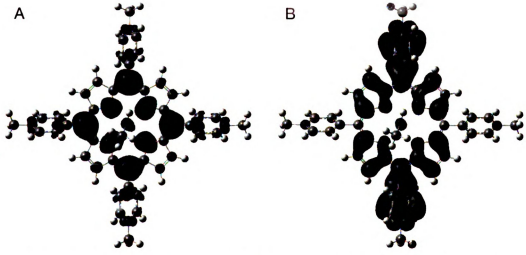

Figure 3.1. Optimized structure of Zn^{II} *meso*-tetrakis(N-methylpyridyl)porphyrin (ZnTMPyP) complexed with a single methanol molecule as an axial ligand to the Zn^{II} ion. The structure was obtained from a B3LYP hybrid density functional electronic structure calculation with Gaussian 03[87] at the 6-31G level of theory. The ball-and-stick structures are shown superimposed with density surfaces for (a) the highest occupied molecular orbital (HOMO) and for (b) the lowest unoccupied molecular orbital (LUMO).

3.3 Experimental

3.3.1 Sample Preparation

ZnTMPyP (CAS 28850-44-4) was used as received from Sigma-Aldrich. CH_3OH (spectrophotometric grade) and CD_3OD (99.8 atom %D) were obtained from Sigma-Aldrich. CH_3OD (99 atom %D) was obtained from Cambridge Isotope Labs. Acetonitrile (CH_3CN, from Mallinkrodt, spectrophotometric grade), dimethylsulfoxide (DMSO, from EMD, ACS grade), and N,N-dimethylformamide (DMF, from Jade Scientific, reagent ACS grade) were used as received.

For use in the femtosecond pump-probe experiments, solutions of ZnTMPyP were prepared by dissolving the dry ZnTMPyP powder in the indicated solvent to obtain an absorbance of 0.4 for a path length of 1.0 mm at the center of the laser spectrum at 420 nm, as detailed below; with the methanols and DMSO, the solution was passed through a 0.22-μm microfilter prior to checking the absorbance. The samples were held in the femtosecond pump-probe spectrometer at room temperature (23 °C) in a fused-silica flow cuvette (0.5-mm path length). A peristaltic pump was used to circulate a 10-mL reservoir of sample solution through the cuvette at 2.75 mL/min. The sample's absorption spectrum was monitored during the experiment for changes arising from photochemistry or permanent photobleaching. The sample reservoir was exchanged with fresh solution several times during each run.

3.3.2 Continuous-Wave Absorption and Fluorescence Spectroscopy

Absorption spectra were obtained at 23 °C with a Hitachi U-2000 spectrophotometer (2-nm band pass). Fluorescence spectra were acquired at 23 °C with a Hitachi F-4500 spectrofluorimeter (5-nm band pass for the excitation and emission monochromators). As presented as a function of wavenumber, the fluorescence intensities are

multiplied by the square of the wavelength in order to compensate for the fixed (in wavelength units) spectral bandpass of the emission spectrometer.[89]

3.3.3 Femtosecond Spectroscopy

Femtosecond pump–probe transients with impulsive excitation were recorded using the dynamic-absorption technique[26,32,35–37] with a pump–probe spectrometer (see Figure 3.2) consisting of a frequency doubled, self-mode-locked Ti:sapphire oscillator (Coherent Mira-F oscillator and Verdi V5 (5 W) Nd:YVO_4 pump laser, Coherent/Inrad 5-050 second-harmonic generator), a SF10 Brewster prism-pair pulse compressor, and a rapid-scanning, modified Mach-Zehnder interferometer with confocal sample and autocorrelation-crystal positions. The present experiments employ 50-fs pulses with intensity spectra centered at 420 nm (4-nm FWHM, as measured with an Ocean Optics USB-2000 spectrometer/CCD detector with a 0.5-nm bandpass), and a fairly narrow bandpass (0.5 nm) of the transmitted probe beam. This approach corresponds to that used by Champion and coworkers in their studies of low-frequency vibrational coherence in heme proteins.[53,55,62]

The apparatus and methodology used in this work is largely that described in our recent study of rapidly damped vibrational coherence in BChl solutions with *Q*-band (780-nm) excitation,[63] but a number of changes were required to permit work in the blue part of the spectrum. A 76-MHz train of 840-nm pulses is generated by a Coherent Mira 900F Ti:sapphire oscillator equipped with Coherent's X-wave broad-tuning-range (690–1020-nm) cavity optics; the oscillator is pumped by a Coherent Verdi pump laser (5-W output). As shown in Figure 3.2, these red pulses first enter a pulse-compression system composed of a double-passed pair of SF10 Brewster-angled prisms and an adjustable interprism path length. The output pulses are directed to a Coherent/Inrad 5-050 second-harmonic generator, which is fitted with a

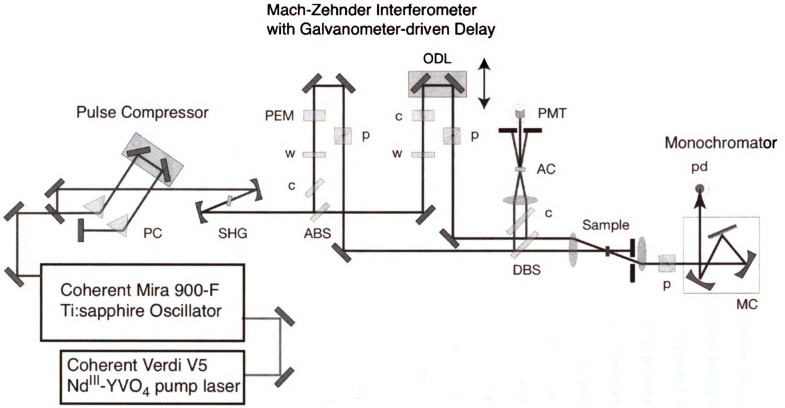

Figure 3.2. Femtosecond pump–probe spectrometer, consisting of a prism-pair pulse compressor (PC), second-harmonic generator (SHG), and a modified Mach-Zehnder interferometer. Other symbols: ABS, autocorrelator beamsplitter; c, compensating beamsplitter or modulator substrate; w, $\lambda/2$-retarder waveplate; PEM, photoelastic modulator; p, Glan-laser calcite polarizer; ODL, galvanometer-driven optical delay line for probe beam; DBS, dichroic beamsplitter; AC, β-barium borate autocorrelation crystal; PMT, photomultiplier tube; MC, Acton-Research SP-150 monochromator; pd, photodiode.

type I β-barium borate (BBO) second-harmonic generation (SHG) crystal (1-mm path length).

The co-propagating 420 and 840-nm output beams that radiate from the BBO crystal are then directed to a modified Mach-Zehnder pump-probe interferometer. For this work, the interferometer was redesigned to support a *dichroic* mode of operation that allows us to control and characterize pump-probe pairs of blue pulses in the 350–500-nm region of the spectrum. The interferometer employs a femtosecond autocorrelator beamsplitter (CVI Laser, FABS-800-45S) to split the input beam into pump and delayed probe pulses; as specified, the 800-nm beamsplitter divides the *s*-polarized 840-nm light evenly into two beams, but the *p*-polarized 420-nm light is divided by the beamsplitter into two beams with a 3:1 pump:probe intensity ratio. The pump-probe delay is scanned continuously by a galvanometer-driven retroreflector (Clark-MXR, ODL-150) mounted in the probe beam's arm of the interferometer. The pump beam's intensity is modulated at 100 kHz by a $\lambda/2$-retarding (at 420 nm) photoelastic modulator (Hinds Instruments) and a calcite polarizer (Karl Lambrecht), in series.[90] Because the planes of polarization of the 420-nm and 840-nm components are *orthogonal* as they enter the photoelastic modulator owing to the use of the Type I SHG crystal, the 420-nm and 840-nm beams that emerge from the calcite polarizer exhibit amplitude-modulation envelopes that are 90° out-of-phase with respect to each other, but no their planes of polarization are *parallel*, as analyzed by the polarizer. The compensating calcite polarizer in the probe beam is oriented 45° with respect to the pump-beam's polarizer, so the two orthogonally polarized colors are analyzed equivalently, and the output planes of polarization are parallel.

Finally, a single dichroic beamsplitter removed from the Coherent/Inrad 5-050 SHG unit is mounted to separate the 420-nm and 840-nm light in the pump and probe beams, which propagate along parallel paths on the optical table as they exit the delay arms of the Mach-Zehnder interferometer. A fused-silica singlet lens (5-

cm focal length) is employed to focus the 420-nm pump and probe beams onto the sample; the 840-nm pump and probe beams are focused onto a thin (100μm thickness) BBO autocorrelation crystal by a matching lens. After it emerges from the sample, the probe beam is analyzed by a calcite polarizer oriented at 90° with respect to the pump-beam's plane of polarization, and then the residual probe light enters an Acton-Research SP-150 monochromator. An amplified photodiode (Thorlabs PDA55) and a lock-in amplifier (SRS, SR850) referenced to the pump-modulation frequency are used to detect the pump–probe signal from a 0.5-nm bandpass of the probe beam. A photomultiplier (1P28, in a Clark-MXR housing) and a lock-in amplifier (Femto, LIA-MV-200H) are used to detect the background-free autocorrelation signal that is generated by the 840-nm pump–probe beams incident upon the BBO autocorrelation crystal. The pump–probe and autocorrelation signals are recorded and averaged simultaneously by a sample-and-hold amplifier and transient recording system, as described previously.[29] In the present work, the probe delay is linearly scanned at 1.0 Hz over the −3 to +27 ps range. The pump–probe and autocorrelation signals are sampled at 17 kHz, and there are 13000 points in each scan; the effective dwell time during data acquisition is 2.3 fs/point.

The autocorrelation signal obtained from the 840-nm pump and probe beams is used in the characterization of the group-delay dispersion of the entire apparatus. The effective instrument-response function for the 420-nm pump and probe pulses is minimized by adjusting the distance between the pair of Brewster prisms; the width of the 840-nm autocorrelation and the pump–probe photobleaching rise time obtained with the 420-nm pulses are monitored simultaneously. The autocorrelation signal is also used as a reference timing pulse for the transient recorder[29] that is used to acquire simultaneously the autocorrelation signal and the pump–probe signal. The autocorrelation pulse is precisely correlated on the probe-delay axis with the zero of time, where the 420-nm pump and probe pulses overlap temporally in the sample,

so its timing is used to cancel the temperature-induced drift in the dimensions of the pump and probe arms of the interferometer and to compensate for jitter in the scanning of the probe-delay line. The use of the fundamental (red) pulses in the autocorrelation arm of the instrument permits us to operate this instrument with the blue pump and probe pulses tuned well into the ultraviolet. If the blue pulses were used directly to obtain the autocorrelation, the 200-nm transmission cutoff of the BBO crystal would not permit tuning of the pump and probe pulses below 400 nm.

Each dynamic-absorption transient that is presented here and in the subsequent chapters is the result of averaging together several scans. For each probe delay point, the mean and standard deviation from the set of individual scans were recorded. Statistical filtering was used to reject outlying points. The transients effectively represent the result of several days worth of repeated experiments for each type of sample.

3.4 Results

Figure 3.3 shows continuous-wave absorption and fluorescence spectra from ZnTMPyP in methanol (CH_3OH) at 23 °C. The spectra are plotted as relative dipole strengths[89,91,92] as a function of wavenumber ν, $A(\nu)/\nu$ and $F(\nu)/\nu^3$, respectively. The absorption spectrum features two bands, the Soret (or B) band and the Q band, in the blue and red parts of the spectrum, respectively. The fluorescence spectrum extends to the red of the Q band. Figure 3.4 shows the solvent dependence of the Soret-band region from solutions of ZnTMPyP in CH_3OH, dimethylformamide (DMF), acetonitrile (CH_3CN), and dimethylsulfoxide (DMSO) at 23°C. Also shown in Figure 3 is the output spectrum from the frequency doubled Ti:sapphire oscillator as it was tuned for the dynamic-absorption experiments to 420 nm. The detected probe bandpass was obtained from the red side of the laser spectrum (422 nm).

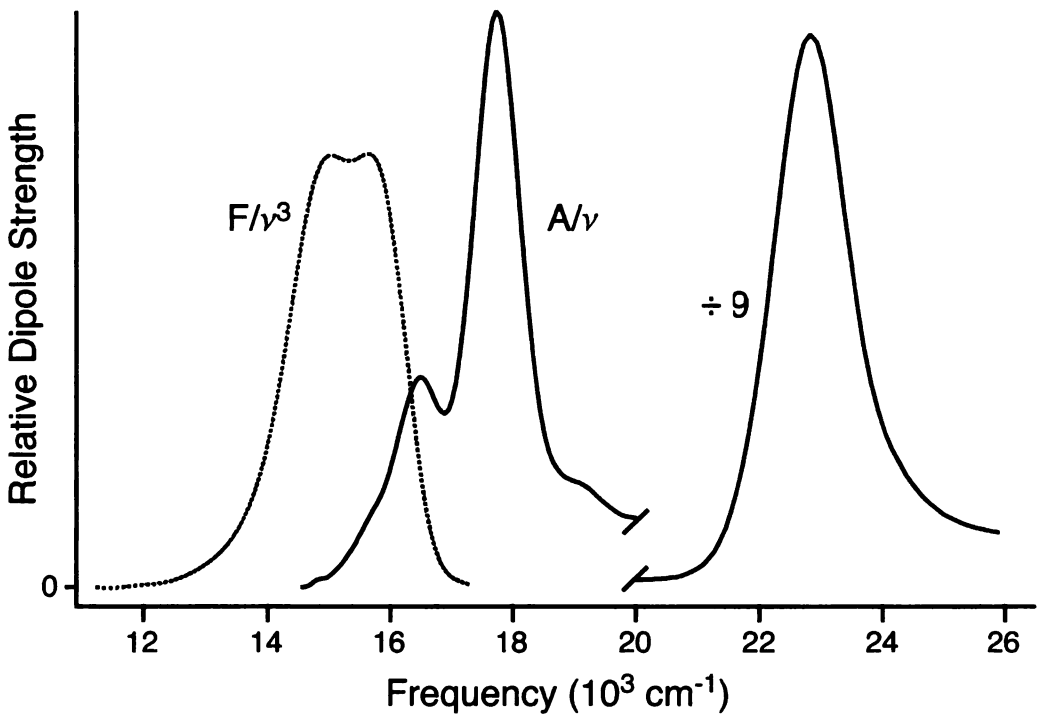

Figure 3.3. Soret ($\nu > 20000$ cm^{-1}) and Q-band region of the continuous-wave absorption (solid curve) and fluorescence (dotted curve) spectra from ZnTMPyP in CH_3OH at room temperature (23 °C), plotted as the dipole strength, A/ν and F/ν^3, respectively, and normalized to unit area with respect to the fluorescence spectrum and Q band.

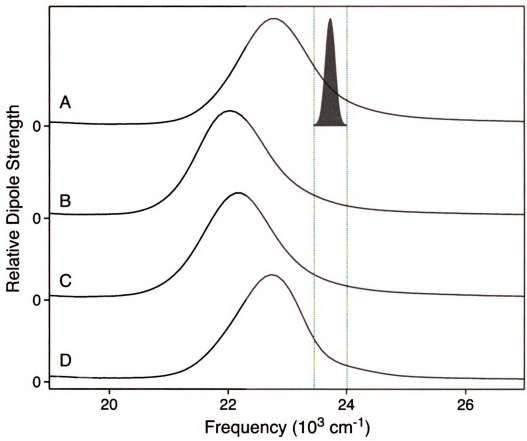

Figure 3.4. Soret-band absorption dipole-strength (A/ν) spectra from ZnTMPyP in (a) CH_3OH, (b) DMF, (c) CH_3CN, and (d) DMSO. Superimposed with arbitrary scaling on (a) is the intensity spectrum of the 420-nm, 50-fs pulses used in all of the pump-probe experiments.

The dynamic-absorption transients obtained from the ZnTMPyP solutions under these experimental conditions are shown in Figure 3.5. Following an intense coherence spike that goes off the plotted scale,[93-95] the transients exhibit a pattern of cosinusoidal modulations nearly all the way to the end of the 25-ps recording that is superimposed upon a single or double exponential decay function. The modulation pattern includes a strong very low-frequency component with positive-going recurrences at ~2 ps and ~18 ps; this oscillation carries a less intense set of higher frequency modulations that are even more slowly damped. Lastly, a very rapidly damped modulation contributes primarily to the 250-600-fs region of the transient. This portion of the signal is similar in character to the rapidly damped vibrational coherence observed in polar solutions of BChl, where the slowly damped portion of the signal is perhaps ten times weaker than observed in the ZnTMPyP transient.[63]

The dynamic-absorption signals from ZnTMPyP were fit in the time domain to a model consisting of a single- or double-exponential decay and an oscillatory portion containing slowly and rapidly damped parts. The models used previously with the signals observed in BChl solution and in the B820 or B777 systems were intended to handle only the rapidly damped components in the modulation pattern.[63-65] After truncation of the signal prior to the 250-fs delay point in order to avoid contributions from the tail of the coherence spike and from nonresonant background signals,[95] the oscillatory part was isolated by subtracting a fitted single- or double-exponential function:

$$I(t) = A_0(1 + A_1 e^{-t/\tau 1} + A_2 e^{-t/\tau 2}) \qquad (3.1)$$

The fit parameters are listed in Table 3.1. The transients and fits were normalized by dividing by A_0 in order to compare the amplitude of the modulation components to the intensity of the pump-induced ground-state depletion signal, which is effectively constant on the 0-25-ps time scale.

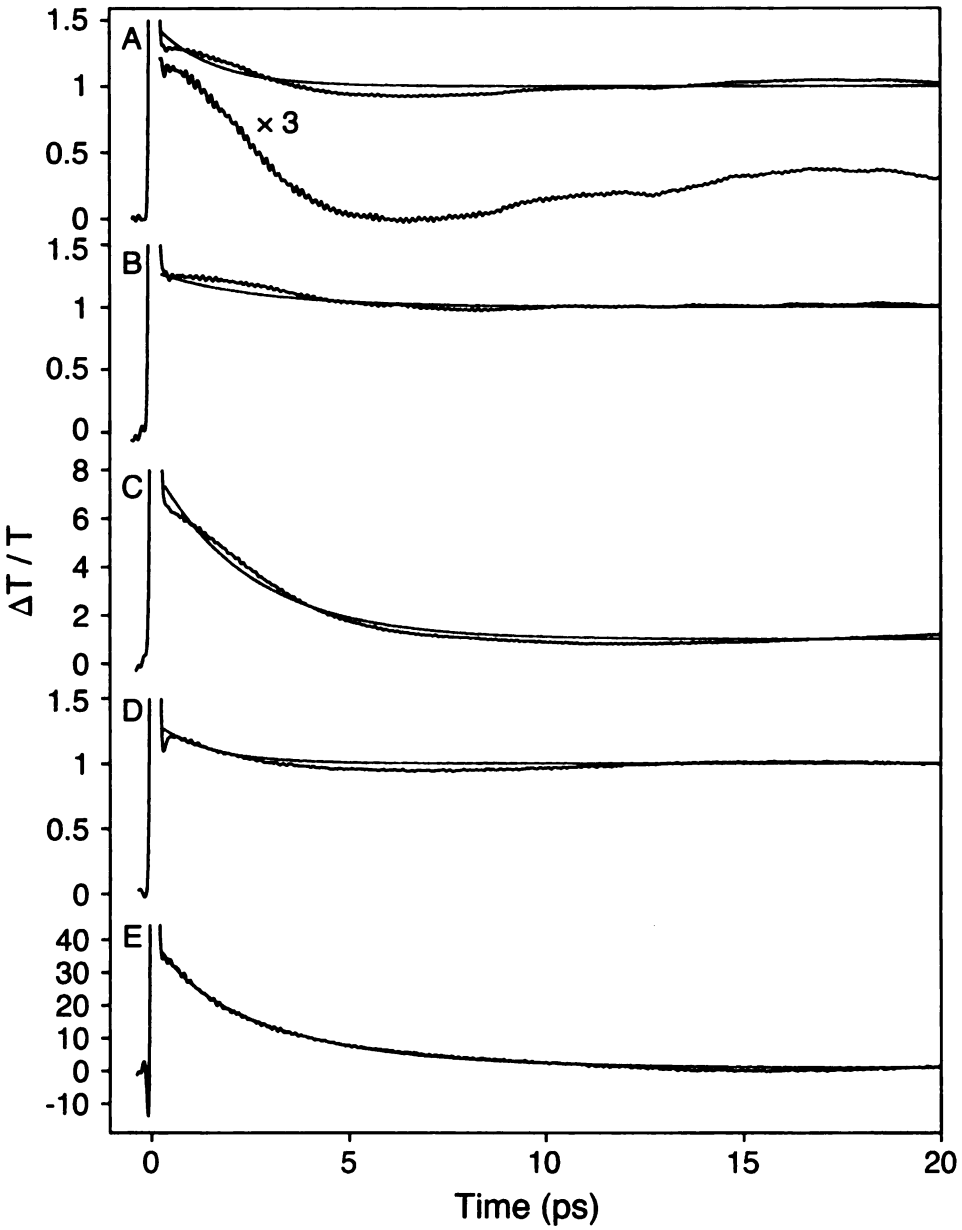

Figure 3.5. Femtosecond pump-probe dynamic-absorption transients detected at 422 nm (0.5-nm bandpass) with ZnTMPyP solutions in (a) CH_3OH, (b) CD_3OD, (c) DMF, (d) CH_3CN, and (e) DMSO. The >250-fs portion of the signal in CH_3OH is also shown in a ×3 expanded view. The signal traces are shown superimposed on single- or double-exponential fit functions of the form $A_0(1 + A_1e^{-t/\tau 1} + A_2e^{-t/\tau 2})$ for the 250-fs–25-ps range. The fit parameters are provided in Table 3.1. As plotted, the signals are normalized by dividing by the non-decaying fraction, A_0.

Table 3.1. Model parameters[a] for the exponential decays in the pump-probe transients[b] in ZnTMPyP solutions at 22 °C.

Solvent	A_1	τ_1 (ps)	A_2	τ_2 (ps)
CH_3OH	0.194	1.4	—	—
CD_3OD	0.260	2.5	—	—
DMF	2.32	2.4	—	—
CH_3CN	0.160	1.2	0.293	1.4
DMSO	1.64	0.8	5.78	3.2

[a] $I(t) = A_0(1 + A_1 e^{-t/\tau 1} + A_2 e^{-t/\tau 2})$; A_0 is a normalization constant.

[b] See Figure 3.5.

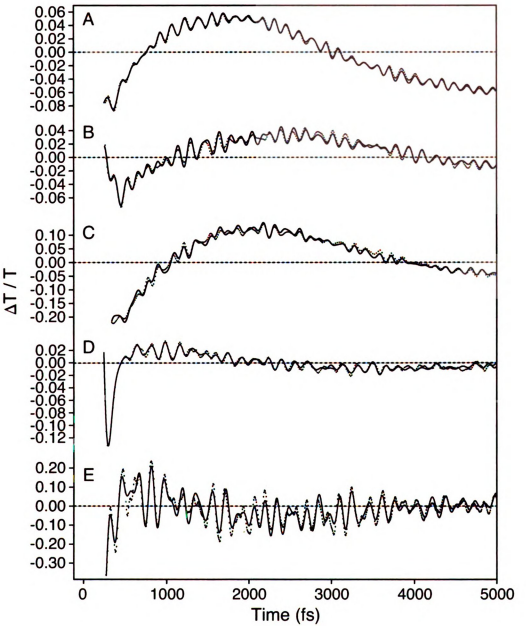

Figure 3.6. Oscillatory signals obtained from the pump–probe transients from ZnTMPyP solutions (see Figure 3.5) as the difference between the normalized signal and the fitted exponential decay functions: in (a) CH_3OH, (b) CD_3OD, (c) DMF, (d) CH_3CN, and (e) DMSO. The data points are shown superimposed on a time-domain model composed of slowly damped and rapidly damped components (see Equations 3.2–3.6). The model parameters are listed in Tables 3.2 and 3.3.

The oscillatory residuals, the difference between the normalized signal and the fitted decay function, were then fit by a multicomponent model that contains both slowly damped and rapidly damped oscillatory components (see Figure 3.6). The slowly damped part was modeled over the 250–7000-fs range as a sum of damped cosinusoids of the form

$$I_i(t) = A_i \, e^{-t^2\sigma_i^2/2} \cos(\omega_{0i}t - \phi_i) \, / \sqrt{2\pi} \tag{3.2}$$

with each modulation component i having a center frequency ω_{0i} and phase ϕ_i. These waveforms correspond to Gaussian lineshapes in the frequency domain,

$$I_i(\omega) = A_i \, e^{-(\omega-\omega_{0i})^2/(2\sigma_i^2)} \, / \, (\sigma_i\sqrt{2\pi}) \tag{3.3}$$

where the linewidth is controlled by the standard deviation, $\sigma_i = \Delta\omega_i / 2\sqrt{2 \ln 2}$, with $\Delta\omega_i$ representing the full width at half maximum. Equations 3.2 and 3.3 are normalized so that the amplitude A_i corresponds to the area of the lineshape in the frequency domain and to the intensity of the signal in the time domain; Equation 3.2 corresponds to the Fourier transform of Equation 3.3. As discussed below, an approximate description of the signal can be obtained with components described by exponentially damped cosinusoids,

$$I_i(t) = A_i \, e^{-t/\gamma_i} \cos(\omega_{0i}t - \phi_i) \tag{3.4}$$

which correspond to Lorentzians in the frequency domain, but a poorer fit to the signal was obtained especially at long delays t; the model walks out-of-phase with respect to the experimental signal, and the time dependence of the amplitude is poorly described.

The rapidly damped part of the oscillatory residuals (Figure 3.6) was modeled in the time domain as the sum of two inhomogeneously broadened components with asymmetric Gaussian lineshapes. It was previously shown that such a model provides a good description of the rapidly damped vibrational coherence from BChl in

polar solution;[63,64] the reader is directed to that work for a detailed discussion and for tests of the model. The two rapidly damped components are assigned, in order of frequency, to the hindered translational and librational (hindered rotational) intermolecular modes between the porphyrin or chlorophyll macrocycle and its clustered, first-solvation-shell solvent molecules.[63,96,97]

In the work on BChl solutions, each rapidly damped component was described in the time domain by an integral over a distribution of exponentially damped cosinusoids with an intrinsic (or homogeneous) damping time γ; the intensities of the cosinusoids are scaled by a lognormal lineshape,[98] $\mathcal{L}(\omega)$:

$$I_i(t) = \int_0^\infty d\omega\, \mathcal{L}(\omega)\, \cos(\omega t - \phi_i)\, e^{-t/\gamma} \tag{3.5}$$

$\mathcal{L}(\omega)$ is parameterized by its area, A_i, its center frequency, ω_{0i}, its width , $\Delta\omega_i$, and an asymmetry (or skew) parameter, ρ_i.

In the present work, the $\mathcal{L}(\omega)$ distribution function was approximated with the piecewise sum of two half-Gaussian lineshapes, $\mathcal{G}(\omega, A_i, \omega_{0i}, \sigma_i, \rho_i)$, and the integral is replaced by a sum over an evenly spaced set of sub-Gaussian components $I_j(t)$ of width $\sigma_i/4$ spaced by $\sigma_i/2$:

$$I_i(t) = \sum_{j=0}^{22} \mathcal{G}(\omega_{0j} = \omega_{0i} + (j-8)\sigma_j, A_i, \omega_{0i}, \sigma_i, \rho_i)\, I_j(t, \omega_{0j}, \sigma_j = \sigma_i/4) \tag{3.6}$$

The j sub-Gaussians are expressed in the time and frequency domain by expressions analogous to Equations 3.2 and 3.3; in the sum, they are scaled by the intensity of $\mathcal{G}(\omega)$ sampled at their center frequencies, ω_{0j}. The right- and left-side widths $\sigma_{r,l}$ of $\mathcal{G}(\omega)$ are determined by the overall width of the distribution σ_i and its asymmetry ρ_i as

$$\sigma_i = (\sigma_l + \sigma_r)/2 = \sigma_l(1 + \rho_i)/2 \tag{3.7}$$

The widths σ_r and σ_l are related by $\rho_i = \sigma_r/\sigma_l$; the left- ($l$) and right-hand ($r$) half-Gaussians are defined by Equation 3.3 over $\omega < \omega_{0i}$ and $\omega \geq \omega_{0i}$, respectively. Note

that the choice of the width and spacing of the sub-Gaussians determines the number required (here, 23) to obtain a smooth approximation of a lognormal distribution. The sum in Equation 3.6 was truncated at 0 cm^{-1}, if necessary, in order to avoid the addition of negative frequencies to the waveform, and it was normalized so that the area of the lineshape in the frequency domain was set to the amplitude parameter A_i. The resulting rapidly damped waveform and lineshape are indistinguishable from those obtained in the previous work for a given set of parameters, but the nonlinear optimization program runs perhaps two orders of magnitude faster than before because the lognormal lineshape function itself[98] is avoided and the number of sub-Gaussians in the sum is small. A further benefit is that no assumption of the intrinsic damping time γ is required—a Raman echo experiment would be required to obtain a discrete measurement of the homogeneous linebroadening.[99,100]

The slowly and rapidly damped portions of the signal were modeled separately in order to simplify the optimization procedure. The slowly damped part of the residual oscillatory signal was modeled first using a set of components constrained to have narrow lineshapes ($\Delta\omega_i < 10$ cm^{-1}). Starting frequencies and widths for these components were obtained from a Hanning-windowed Fourier-transform spectrum (see Figure 3.7); the window function attenuates the rapidly damped portion of the signal.[92] The twelve most intense components in the Fourier-transform spectrum were included in the slowly damped part of the model. The converged model produced a Hanning-windowed Fourier transform spectrum that matched the experimental spectrum; the frequencies, widths, and relative amplitudes are particularly well defined because the linewidths are narrow. The rapidly damped model discussed above was then constrained during the second phase of the optimization process to return only broad lineshapes ($\Delta\omega_i > 10$ cm^{-1}). In all the solvents studied, the sum of two rapidly damped asymmetric Gaussian components provided a good description of the rapidly damped residual function.

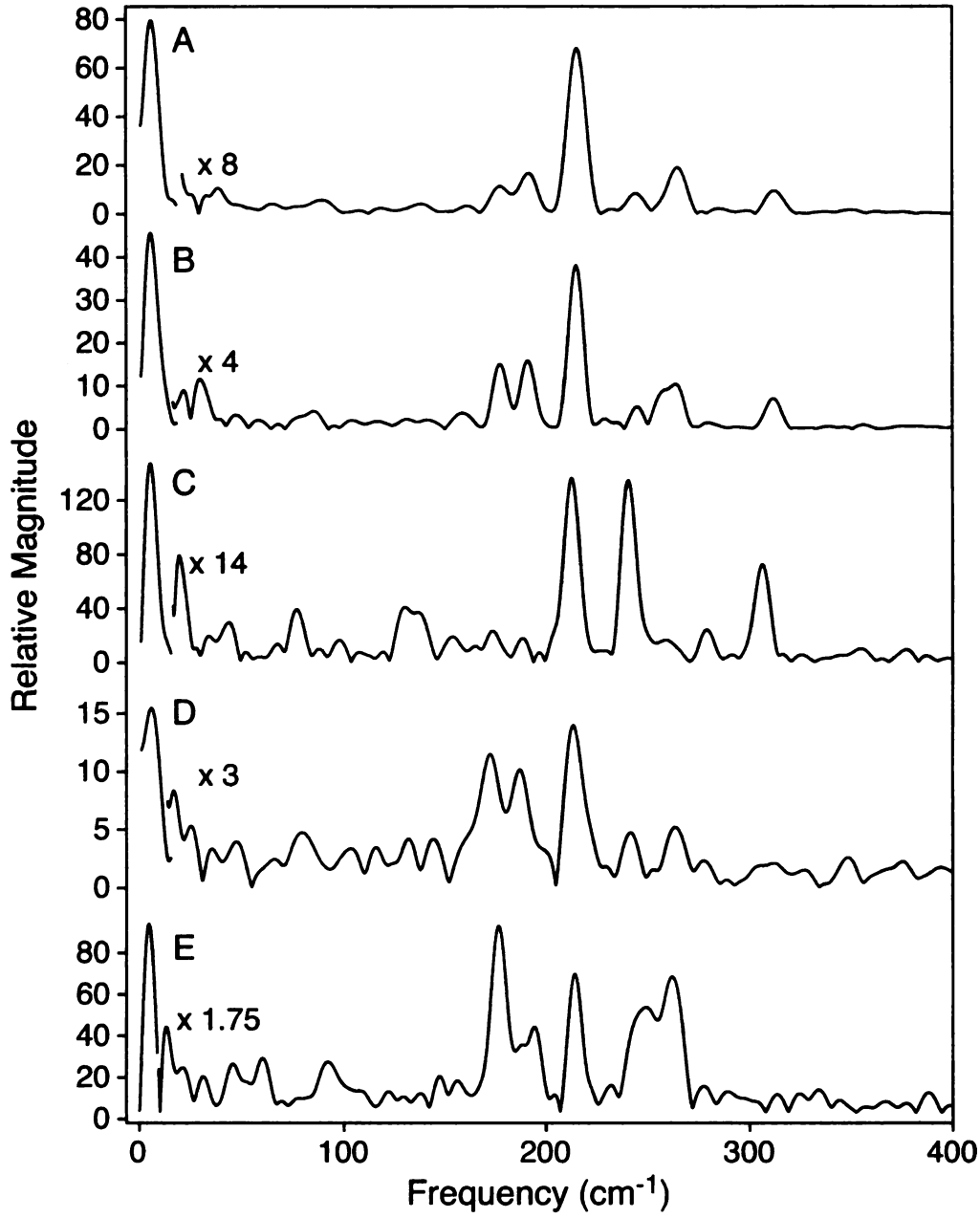

Figure 3.7. Fourier transform magnitude spectra from the oscillatory residuals (see Figure 3.6) of the pump-probe signals from ZnTMPyP solutions in (a) CH_3OH, (b) CD_3OD, (c) DMF, (d) CH_3CN, and (e) DMSO. The Fourier transform was applied to the oscillatory input signals after a Hanning window was applied over the 250-7000-fs range.

Table 3.2. Solvent dependence of the asymmetric Gaussian lineshape parameters for the rapidly damped components observed in the vibrational coherence from ZnTMPyP.

Component	Parameter[a]	Solvent CH_3OH	CD_3OD	DMF	CH_3CN	DMSO
1	ω_0, cm^{-1}	68	63	82	80	100
	$\Delta\omega$, cm^{-1}	49	55	59	50	48
	A^b	9.81	10.1	7.67	69.8	62.2
	ρ	1.18	1.17	1.45	1.21	1.17
2	ω_0, cm^{-1}	81	73	94	119	124
	$\Delta\omega$, cm^{-1}	59	45	50	59	56
	A^b	15.1	17.2	8.10	82.3	125
	ρ	1.18	1.18	1.29	1.15	1.55
Sum	$\langle\omega\rangle$, cm^{-1}	79	74	95	106	125
	$\sum_i A_i$	24.9	27.3	15.8	152	187

[a] See Equations 3.2-3.6 and the text.

[b] Normalized to the intensity of the ~215-cm^{-1} slowly damped component in each solvent.

Table 3.3. Gaussian lineshape parameters[a] for the slowly damped modulation components observed in ZnTMPyP pump-probe transients.

Component	Solvent				
	CH_3OH	CD_3OD	DMF	CH_3CN	DMSO
1	3, 3.47, 25	3, 1.74, 12	2, 10.6, 77	3, 3.66, 3.2	4, 3.14, 2.9
2	21, 8.88, 1.5	23, 16.8, 1.2	19, 6.87, 2.4	19, 11.8, 1.5	13, 2.37, 0.41
3	38, 2.03, 0.16	29, 2.35, 0.32	43, 3.13, 0.22	47, 0.697, 0.15	46, 2.40, 0.19
4	89, 2.39, 0.096	85, 2.35, 0.13	76, 417, 0.39	79, 1.00, 0.27	93, 4.18, 0.28
5	138, 2.78, 0.071	131, 2.35, 0.064	134, 8.24, 2.0	131, 2.01, 0.23	148, 2.86, 0.21
6	177, 2.96, 0.21	177, 4.05, 0.75	174, 2.01, 0.090	172, 2.42, 0.41	177, 3.19, 1.4
7	191, 2.78, 0.31	190, 4.23, 0.53	188, 2.52, 0.091	186, 4.45, 0.81	195, 5.88, 1.7
8	215, 1.67, 1.0	214, 1.77, 1.0	212, 3.35, 1.0	213, 3.53, 1.0	214, 2.56, 1.0
9	244, 1.90, 0.13	244, 2.35, 0.15	240, 2.25, 0.81	241, 2.34, 0.18	249, 2.36, 0.52
10	264, 3.62, 0.43	263, 7.06, 1.5	259, 3.16, 0.13	263, 3.02, 0.14	262, 4.24, 1.5
11	284, 3.16, 0.42	279, 6.04, 0.12	278, 3.28, 0.17	277, 4.17, 0.020	290, 4.48, 0.13
12	312, 3.24, 0.19	311, 2.06, 0.20	306, 4.91, 0.89	312, 3.93, 0.17	314, 1.61, 0.20
A_8[b]	0.016	0.016	0.025	0.015	0.089

[a] (ω_0, cm^{-1}; $\Delta\omega_0$, cm^{-1}; A_i); see Equations 3.2-3.6 and the text. The amplitudes A_i are normalized by that of component 8.

[b] Raw amplitude for component 8 relative to normalized pump-probe transient (see Figure 3.5).

The sum of the rapidly damped and slowly damped models is superimposed on the data points in Figure 3.6. Both the slowly damped and rapidly damped portions of the model were found to be robust with respect to the starting parameters used in both parts of the nonlinear optimization procedure. The final fitted amplitudes A_i have estimated confidence intervals that are no worse than ±5%, and the center frequencies ω_{0i} are known with confidence intervals of ±2 cm^{-1}. The parameters for the optimized time-domain models shown in Figure 3.6 are tabulated in Tables 3.2 and 3.3. The tabulated amplitudes A_i are normalized with respect to the intensity of the ground-state depletion part of the signal (see the ordinate scaling for Figure 3.5) and to the amplitude for the ~215-cm^{-1} component, the strongest slowly-damped, high-frequency (ω_{0i} > 100 cm^{-1}) component in all of the solvents but DMSO, where the 195-cm^{-1} component is the strongest.

Effective exponential damping times for the Gaussian or asymmetric Gaussian modulation components were estimated by fitting an exponentially damped cosinusoid (see Equation 3.4) to the Gaussian waveform for each component in the model. This exercise corresponds in the frequency domain to optimizing a Lorentzian lineshape to the corresponding Gaussian lineshape. As an example, the Gaussian linewidths, $\Delta\omega_0$, and the exponential damping times, γ, are compared for ZnTMPyP in CH_3OH in Table 3.4; similar results (not shown) are obtained in the other solvents. Figure 3.8 compares the Gaussian and fitted Lorentzian waveforms for the 3, 38, and 215-cm^{-1} components. The Lorentzian waveforms were optimized over the 250-7000-fs range, as in Figure 3.6, but the results are comparable when the entire 150-25000-fs range shown in Figure 3.8 is fit. In general, the fitted Lorentzian waveform is more intense than Gaussian waveform at the beginning and end of the waveform; if the Lorentzian waveform is constrained to fit the Gaussian waveform at the end of the modulation pattern, the resulting damping time is longer. This issue is especially important for the slowly damped 3-cm^{-1} asymmetric Gaussian component, which

Table 3.4. Comparison of Gaussian linewidths and effective exponential damping times[a] for the modulation components observed in the vibrational coherence from ZnTMPyP in CH_3OH.

ω_0, cm^{-1}	$\Delta\omega$, cm^{-1}	γ, ps
3	3.47	2.94[b,c]
21	8.88	1.36
38	2.03	6.71[c]
68[d]	49	0.223
81[d]	59	0.182
89	2.39	5.64
138	2.78	4.85
177	2.96	4.57
191	2.78	4.87
215	1.67	8.14[c]
244	1.90	7.16
264	3.62	3.58
284	3.16	4.11
312	3.24	4.16

[a] See Equation 3.4 and Figure 3.8.

[b] Lower limit; an upper limit of γ = 21.6 ps is obtained by fitting to the $t > 15$ ps portion of the signal.

[c] See Figure 3.8.

[d] Rapidly damped component, see Equation 3.6 and the text.

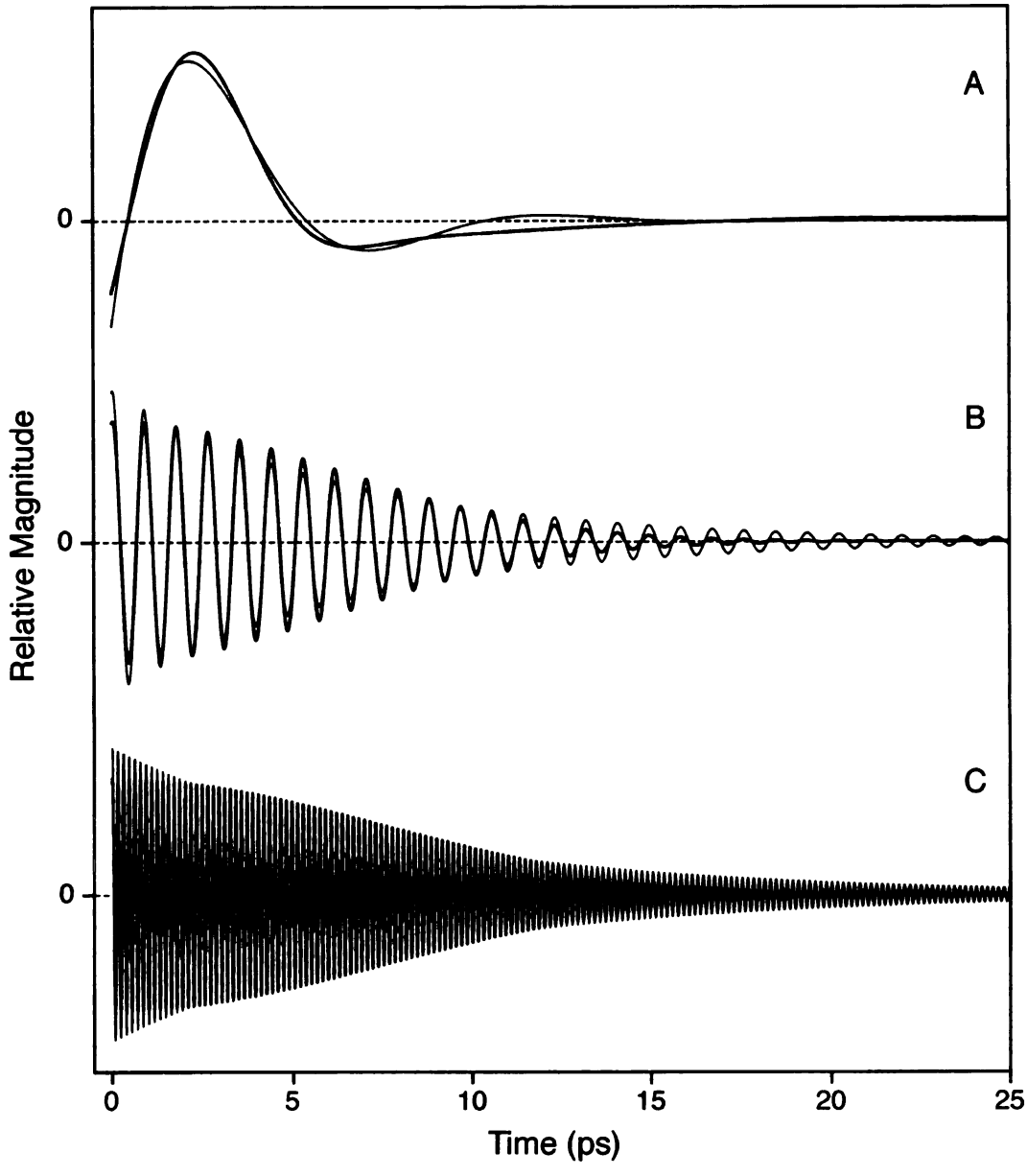

Figure 3.8. Comparison of the Gaussian waveforms (thick curves) obtained for the 3, 38, and 215-cm^{-1} components in the oscillatory signals observed from ZnTMPyP in CH_3OH solution with fitted exponentially damped waveforms (thin curves, see Equation 3.4). The Gaussian linewidths and damping times are listed in Table 3.4.

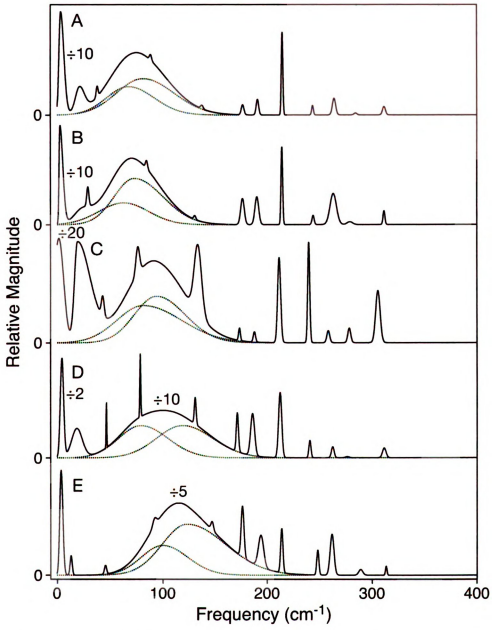

Figure 3.9. Frequency domain representation of the time-domain models of the oscillatory signals (see Figure 3.6) observed in ZnTMPyP solution: in (a) CH_3OH, (b) CD_3OD, (c) DMF, (d) CH_3CN, and (e) DMSO. The broad features in the 50-200-cm^{-1} regime are shown superimposed with the spectra (dotted lines) of their underlying components; in (d) and (e) these features are attenuated in order to keep them on scale. The spectrum from the 2-4-cm^{-1} slowly damped component in (a)-(d) is also attenuated.

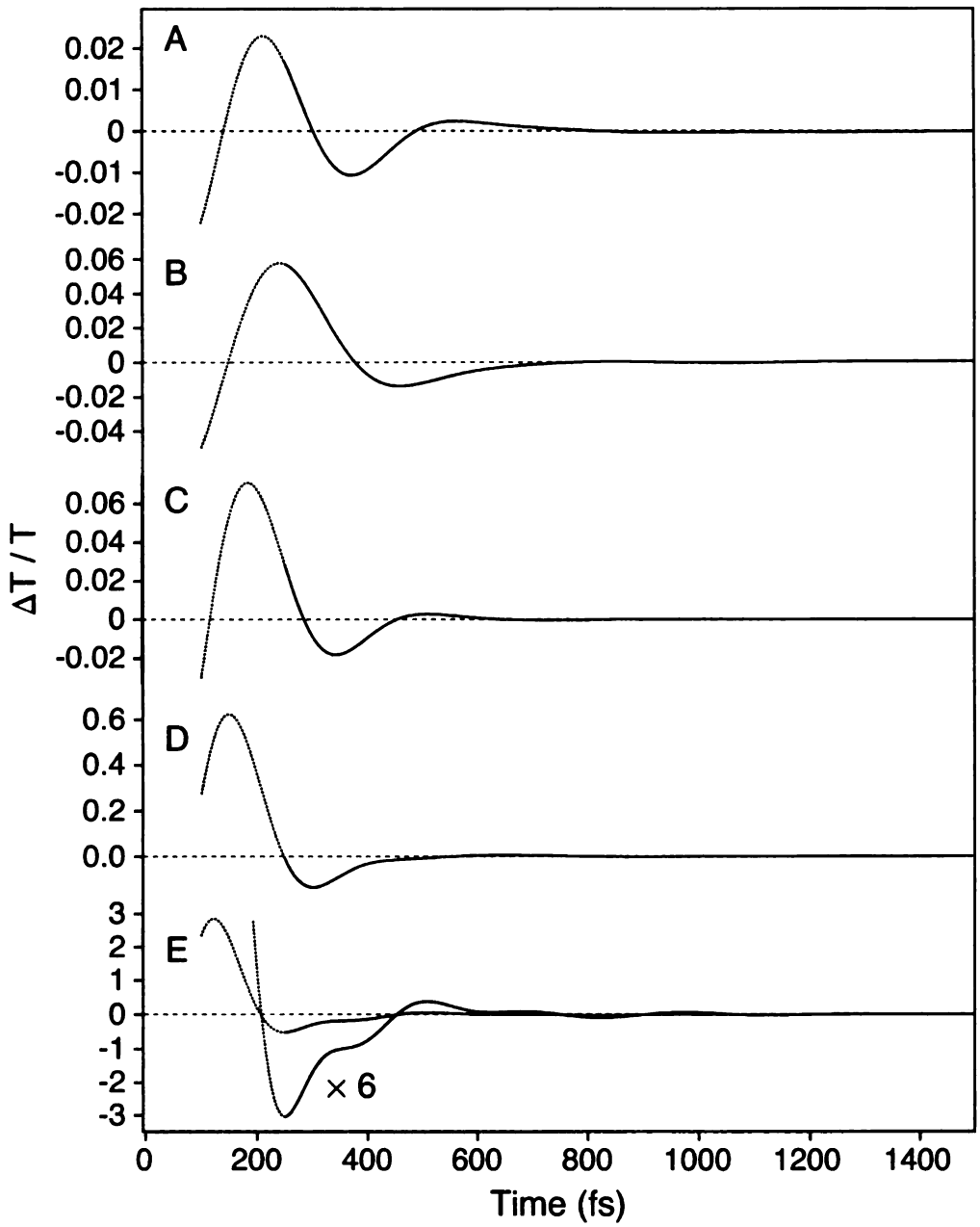

Figure 3.10. Time-domain representation of the rapidly damped oscillatory components (see Figures 3.6 and 3.9) in the pump-probe signals from ZnTMPyP solutions in (a) CH_3OH, (b) CD_3OD, (c) DMF, (d) CH_3CN, and (e) DMSO. The dotted portion of the signal is extrapolated from the fitted region of time (see Figure 3.6).

exhibits a 2.94-ps damping time if the overall waveform is fitted, but if the fit is constrained to the >10-ps region, a 21.6 ps damping time is obtained. As mentioned above, we find that Lorentzian waveforms result in a poor overall model for the oscillatory residuals even if constrained over the 250–6000-fs region, so the damping times in Table 3.4 have to be regarded as crude lower-limit estimates of the damping time. Given that Gaussian lineshapes are observed, and that these lineshapes inherently report inhomogeneous broadening, the true homogeneous damping times may be significantly longer.

Figure 3.9 shows the frequency domain representation of the overall time-domain model for the oscillatory residuals shown in Figure 3.6. The spectra are dominated by the broad lineshapes from the rapidly damped components over the 50–200-cm^{-1} region. The slowly damped component whose lineshape is centered at 2–4 cm^{-1} is, however, comparable in intensity to the sum of the two rapidly damped components (see Tables 3.2 and 3.3). The other slowly damped components are an order of magnitude less intense.

Figure 3.10 shows a time-domain representation of the summed rapidly damped components from the models shown in Figure 3.6. Because the effective damping time for both of the rapidly damped components is <250 fs in all of the solvents, a great deal of the amplitude of this component lies in the early-time truncated portion of the pump-probe transient (see Figures 3.5 and 3.6). As extrapolated in Figure 3.10, the waveforms in CH_3OH and CD_3OD are very similar to the rapidly damped vibrational coherence observed previously in polar solutions of BChl, where the intramolecular, slowly damped vibrational coherence is comparatively weak.[63,64] The strong positive-going recurrence at ~200 fs for the waveform in CH_3OH is only partially observed in the analyzed time region of the residual; a weaker second recurrence at ~600 fs is followed by a broad negative-going trough at ~900 fs that recovers to the baseline over the 1000–1500-fs range. As the solvent is varied, the

extent in time of the rapidly damped waveform contracts as the mean frequency, $\langle\omega\rangle$, increases (see Figure 3.10). From the sum of the two underlining component lineshapes (see Figure 3.9), $\mathcal{M}(\omega) = I_1(\omega) + I_2(\omega)$, the mean frequency obtained using a normalized mean-value relation,

$$\langle\omega\rangle = \frac{\int_0^\infty d\omega\, \mathcal{M}(\omega)\omega}{\int_0^\infty d\omega\, \mathcal{M}(\omega)} \tag{3.8}$$

shifts over the 79–125-cm^{-1} range as the solvent is varied (see Table 3.2 and Figure 3.11). As compared to those observed in CH_3OH, the spectra of the two rapidly damped components in CD_3OD (see Figure 3.9) are downshifted by 5 and 8 cm^{-1} and the mean frequency is downshifted by 5 cm^{-1} (see Table 3.2).

3.5 Discussion

The femtosecond pump–probe, dynamic-absorption transients obtained with Soret-band excitation of polar solutions of ZnTMPyP (see Figure 3.5) exhibit a complex modulated signal superimposed on an exponential or double-exponential decay function with a ~2-ps time constant leading to a non-decaying offset over the 0–25-ps time range. Similar decay components and time constants are attributed to the $S_2 \rightarrow S_1$ internal-conversion process in pump–probe or fluorescence-upconversion experiments with Zn^{II} tetraphenylporphyrin (ZnTPP) in nonpolar solvents,[101,102] but for ZnTMPyP in polar solvents the decays arise from vibrational relaxation and vibrational energy transfer to the solvent in the S_1 state following an ultrafast ($\tau \leq$ 100-fs) internal-conversion process. In femtosecond transient-absorption experiments employing continuum probe pulses and 150-fs pump pulses in the Soret band at 404 nm, Fontaine-Aupart and co-workers[103] failed to detect an S_2-state stimulated-emission band from ZnTMPyP in aqueous solution, so the S_2-state population relaxes to the S_1-state vibronic manifold almost as rapidly as it is prepared by the pump pulse. In contrast, a distinct stimulated-emission band was observed for ZnTPP under the

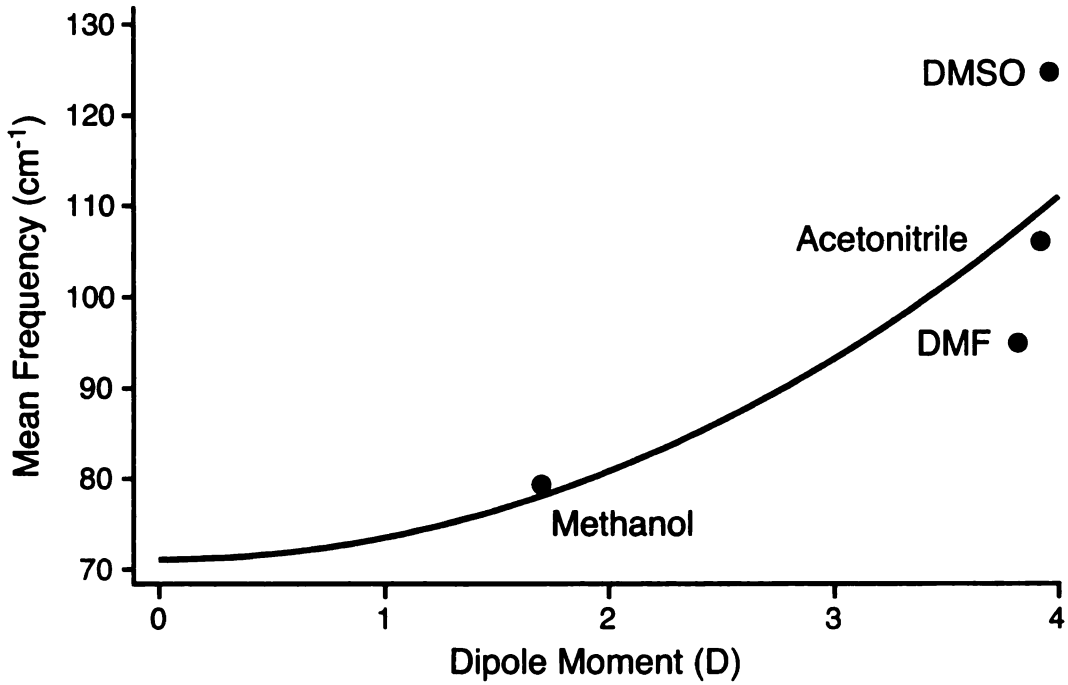

Figure 3.11. Dependence of the mean frequency of the rapidly damped oscillatory components (see Figures 3.6 and 3.9) observed in the pump-probe signals from ZnTMPyP solutions in CH_3OH, DMF, CH_3CN, and DMSO. The data points are shown superimposed with a trend fitted to Equation 3.12.

same optical conditions; the intensity of the stimulated emission decays with a 2-ps time constant as the S_2-state population relaxes to the S_1-state. In ZnTMPyP, population deposited in excited vibronic levels of the S_1-state manifold by the $S_2 \rightarrow S_1$ internal-conversion process is detected in terms of excited-state absorption (ESA) transitions to vibronic levels in the Soret band (states S_n). The time-resolved pump-probe spectra observed by Fontaine-Aupart and co-workers exhibit a broad-region of long-lived (>5 ps) excited-state absorption at wavelengths above 450 nm; the relatively sharp, ground-state depletion band that lies to the blue has a maximum at 435 nm and extends to ~ 405 nm.[103] At wavelengths below 435 nm, however, it is likely that the ground-state depletion and ESA bands overlap extensively. Thus, in our experiments, the net ground-state depletion signal decreases in intensity as the S_1-state population cools on the ps time scale because the ESA band shifts to the blue and overlaps more strongly with the static ground-state depletion band at the 422-nm probe bandpass.

The intensity of the decays we observe in the ZnTMPyP pump-probe signals are solvent dependent, and the decay in two of the solvents (CH_3CN and DMSO) is biexponential. The decays observed for ZnTMPyP in DMSO and CH_3OH are not significantly altered (not shown) when the laser is tuned to 425 nm, closer to the Soret band's maximum but still on the blue side. These observations show that the observed dynamics are less dependent on the initial vibronic state prepared in the S_2-state manifold than they are on the nature of the solvent. Given that dynamic solvation does not contribute to the signal because the S_2 state persists for such a short period following absorption of the pump pulse, the rate at which the excess vibrational energy of the S_1 state is dissipated is solvent dependent. Biexponentiality would arise in this case from the presence of two ensembles of ZnTMPyP with different first-solvation shell structures. A similar explanation was invoked by Zewail and coworkers to account for the biexponential internal conversion for ZnTPP in methylene chloride.[101]

The conclusion that the S_2 state of ZnTMPyP decays to the S_1 state via an internal-conversion process on the $\leq$ 100-fs time scale is especially significant with respect to the present work because it restricts assignment of the modulation components observed in the pump-probe signals to coherent wavepacket motions on the ground-state potential-energy surface. Table 3.4 shows that all of the slowly damped modulation components have effective damping times that are >1 ps; even the two rapidly damped components have effective damping times that are >150 fs. It is unlikely that the ESA transitions that overlap with the probed region of the spectrum contribute to the modulated signal; the $S_2 \rightarrow S_1$ internal-conversion process would be expected to be incoherent with respect to the initial vibrational phase prepared by the pump pulses.[104]

Except for the 2-4-cm^{-1} component, the modulation components with the largest amplitudes A_i are observed in the 200-cm^{-1} region of the spectrum. This pattern of amplitudes is consistent with an assignment to coherent wavepacket motions on the ground-state potential energy surface because these experiments employed 50-fs pump pulses. If the ground- and excited-state potential-energy surfaces of the system are displaced with respect to the coordinate of a normal mode of vibration, moving wavepackets on the ground- and excited-state potential surfaces are generated by two successive actions of the the pump field.[24-26,33] The ground-state wavepacket is created by a process that directly corresponds to resonance Raman scattering. The duration of the pump pulse controls the displacement and momentum of the ground-state wavepacket because it places a limit on the time interval between the first action of the pump field that prepares the ground-excited-state polarization and the second action that materializes the wavepacket on the ground-state surface. The pump-probe signal is modulated optimally by ground-state wavepacket motion when the pump-pulse duration is about one-third of the mode's period; with pulses that are shorter than the optimum, the wavepacket is not displaced very far away

from the Franck-Condon geometry, so only a small modulation of the transmitted probe signal results. Of course, the depth of modulation of the pump-probe signal decreases as the pump-pulse duration increases beyond the optimum duration towards the mode's period.[33] With the 50-fs pulses used in the present experiments, the optimum mode frequency is 222 cm^{-1}; the relative strength of the ~215-cm^{-1} component observed in each solvent is probably due to the close matching of the pump-pulse duration with the mode frequency. Even though the measured amplitude of the 312-cm^{-1} mode is only about one-fifth that of the 215-cm^{-1} mode (see Table 3.3), the relative resonance Raman activities of the two modes are comparable if one considers that the optimum pulse duration that would drive a 312-cm^{-1} wavepacket is ~32 fs.

The unusually large amplitude of the very low frequency, 2-4-cm^{-1} modulation component would seem to be in conflict with an assignment to a ground-state wavepacket motion. The modulation depth that would be expected with 50-fs pump pulses would be close to zero for such a low frequency mode unless it is characterized by an unusually large excited-state displacement. Most of the intramolecular vibrational modes of ZnTMPyP would be expected to exhibit comparable displacements, with the strongest modes associated with the π-electron density in the porphyrin macrocycle, so the rule-of-thumb about the optimum pulse duration discussed above would reasonably apply.[33] An exception might be anticipated for the internal rotation of the peripheral N-methylpyridyl rings (see Figure 3.1). In the ground state, the rings are rotated well away from the the plane of the porphyrin; in the excited state, owing to the flow of the π-electron density from the porphyrin region, the minimum-energy geometry would extend the conjugated region by making the rings and porphyrin coplanar. Thus, an internal rotation of the rings is launched in the excited state by resonant excitation of the Soret band because the S_2-state potential-energy surface is sloped in the Franck-Condon region along that coordi-

nate; the internal rotation would obtain significant momentum prior to preparation of the ground-state wavepacket on the ground-state surface, where the rotation is bound only owing to the poor delocalization of the π-electron density and owing to steric hindrance. This assignment of the 2–4-cm^{-1} mode is also prompted by its significant solvent dependence (see Table 3.3); the highest frequency (4 cm^{-1}) is observed in the most viscous solvent (DMSO), and perhaps the large amplitude in DMF relates to a specific clustering around the rings.

The frequencies, linewidths, and relative intensities of the the other slowly damped modulation components are relatively insensitive to the choice of solvent (see Table 3.3). These components are well modeled (see Figure 3.6) by relatively narrow Gaussian components (Equation 3.2). The solvent independence of the modulation frequencies supports a structural assignment of all of these features to the intramolecular, skeletal modes of the Zn^{II}-porphyrin macrocycle. Normal-mode calculations using the B3LYP hybrid density functional for the ZnTMPyP–methanol complex (see Figure 3.1) are consistent with an assignment of the ~40-cm^{-1} and ~215-cm^{-1} components to the metal-doming and Zn^{II}–axial-ligand stretching modes, respectively; somewhat higher frequencies are assigned to these modes in Fe^{II}–porphyrins.[105] Of these, the former is evidently more solvent sensitive, but it should be kept in mind that the frequencies and intensities of the very lowest frequency components in the slowly damped set of features are known with less confidence than for the higher-frequency or more rapidly damped features. As compared to the amplitude of the rapidly damped components, the slowly damped components are much stronger in ZnTMPyP with Soret-band excitation than observed with *Q*-band excitation of BChl solution; the resonance Raman intensities of the intramolecular modes of porphyrins are strongly enhanced by excitation in the Soret band.[106]

The rapidly damped (γ < 1 ps) part of the vibrational coherence observed in ZnTMPyP solution exhibits solvent-dependent time-domain waveforms that are very

similar to those observed in BChl solution. In the frequency domain, the two rapidly damped components present inhomogeneously broadened lineshapes that are analogous to the ones assigned to the hindered translational and librational modes in instantaneous normal mode analyses of molecular dynamics simulations of polar liquids.[96,97,107] A structural assignment of these components to intermolecular modes between the Zn-porphyrin and the clustered solvent molecules in the first solvation shell is directly supported by the observation of an isotope shift in methanol and perdeuterated methanol solution (see Table 3.2 and Figure 3.9) of approximately the right magnitude. The mean frequency observed in CH_3OH is 79 cm^{-1}; in the harmonic-oscillator limit, if the mode involves an intermolecular mode between a single CH_3OH molecule and the ZnTMPyP molecule, the mode should exhibit a downshift to 74.7 cm^{-1} using the $\omega_D = \omega_H(\mu_H/\mu_D)^{0.5}$ relationship[108] between the frequency ω_D of the deuterated species and the frequency ω_H of the protonated species and their reduced masses μ_D and μ_H, respectively. The observation of a slightly lower mean frequency, 74 cm^{-1}, might indicate the presence of some higher molecular weight species, perhaps from hydrogen-bonded chains,[109-112] but the confidence interval (± 2 cm^{-1}) is larger than this discrepancy. Consistent with the intermolecular mode assignment, a smaller isotope shift was observed in the presence of CH_3OD than in CH_3OH (results not shown); the observed mean frequency of 76 cm^{-1} in CH_3OD is within the confidence interval of the expected value of 77.9 cm^{-1}.

As noted in the Introduction, the solvent dependence of the rapidly damped components (see Table 3.2 and Figure 3.9) provides a test of the form of the van der Waals potential introduced in the previous work on BChl solutions,[63]

$$V_0(r) = a/r^{12} - \left(b\alpha_1\alpha_2 + \frac{c|\boldsymbol{\mu}_1|^2|\boldsymbol{\mu}_2|^2}{(4\pi\varepsilon_0)^2} + \frac{\alpha_2|\boldsymbol{\mu}_1|^2 + \alpha_1|\boldsymbol{\mu}_2|^2}{4\pi\varepsilon_0} \right) \Big/ D^2 r^6 \qquad (3.9)$$

A relation for the natural frequency of the intermolecular mode in the limit of small displacements from the equilibrium structure,

$$\nu = \frac{3}{(2a)^{2/3}}\left(b\alpha_1\alpha_2 + \frac{c|\boldsymbol{\mu}_1|^2|\boldsymbol{\mu}_2|^2}{(4\pi\varepsilon_0)^2} + \frac{\alpha_2|\boldsymbol{\mu}_1|^2 + \alpha_1|\boldsymbol{\mu}_2|^2}{4\pi\varepsilon_0}\right)^{7/6} \Big/ 2\pi D^{7/3}\mu^{1/2} \tag{3.10}$$

is obtained from a Taylor series expansion of Equation 3.9. Both expressions contain a series of terms arising from the physical components of the interaction: the constant a scales the Pauli exchange interaction, the London-dispersion interaction is scaled by the constant $b = 3I_1I_2/2(I_1 + I_2)$, with $I_{1,2}$ representing the ionization potentials for the two molecules, $c = 2/3k_BT$ scales the dipole-dipole interaction, and the $\alpha_2|\boldsymbol{\mu}_1|^2$ and $\alpha_1|\boldsymbol{\mu}_2|^2$ terms arise from the solute-dipole and solvent-dipole induced-dipole interactions, respectively.[113-116] In these equations, $\boldsymbol{\mu}_i$ and α_i correspond to the dipole moment and polarizability for the solute (subscript 1) and solvent (subscript 2); r is the distance between the two molecules, μ is the reduced mass for the intermolecular oscillator, D represents the dielectric constant for the solvent, and ε_0 relates the permittivity of free space.

If the solute chromophore is charged, the intermolecular potential gains two additional terms, for the ion-dipole and ion-induced dipole interactions:

$$V_Q(r) = V_0 - \left(\frac{cQ|\boldsymbol{\mu}_2|^2}{(4\pi\varepsilon_0)^2} + \frac{\alpha_2Q^2}{4\pi\varepsilon_0}\right) \Big/ 2D^2r^4 \tag{3.11}$$

The ion-dipole term depends linearly on the charge Q of the solute and on the square of the solvent's dipole moment, $\boldsymbol{\mu}_2$; the ion-induced-dipole term contains the polarizability α_2 of the solvent and the square of the charge, Q^2. Both terms depend on r^{-4}, so they decay much less rapidly with increasing distance than the rest of the terms in the intermolecular potential. The mode frequency expression that follows from Equation 3.11 is too lengthy to be included here, but it predicts that the charge-dependent terms significantly increase the mode frequency over that predicted by Equation 3.10.

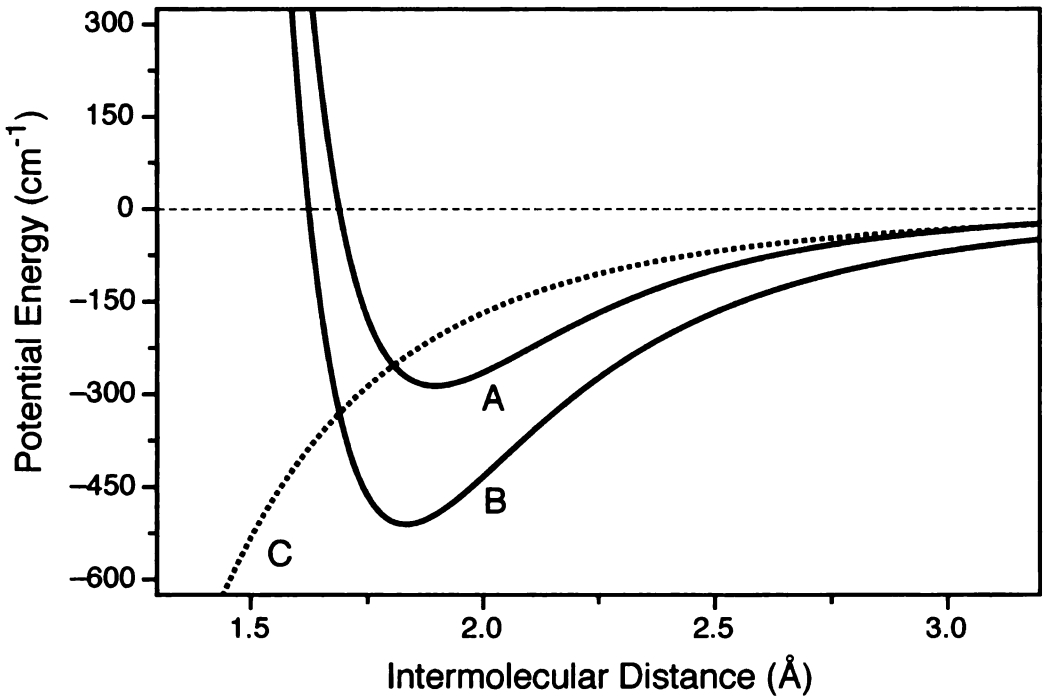

Figure 3.12. Model potential-energy curves for the ZnTMPyP-CH_3OH complex calculated using Equation 3.11 and the experimentally observed mean intermolecular mode frequency, 79 cm^{-1} (see Table 3.2): (a) $Q = 0$; (b) $Q = 1$; and (c) the attractive, charge-dependent terms for $Q = 1$. Table 3.5 lists the other parameters for the potential curves and compares r_{eq} and V_{min} for curves (a) and (b).

Table 3.5. Parameters for the model ZnTMPyP-CH_3OH intermolecular potentials shown in Figure 3.12

Parameter[a]	Value
exchange (Pauli) interaction coefficient, a	76.2 eV Å^{12}
London-dispersion interaction coefficient, $b = 3I_1I_2/2(I_1 + I_2)$	9.35 eV[b,c]
ZnTMPyP dipole moment, $\|\mu_1\|$	0.663 D[b]
CH_3OH dipole moment, $\|\mu_2\|$	1.70 D[c]
ZnTMPyP polarizability, α_1	109.8 Å^3[b]
CH_3OH polarizability, α_2	3.29 Å^3[c]
ZnTMPyP-CH_3OH reduced mass, μ	30.7 Da
CH_3OH dielectric constant, D	33[c]
r_{eq} $(Q = 0)$	1.90 Å
V_{min} $(Q = 0)$	286 cm^{-1}
r_{eq} $(Q = 1)$	1.83 Å
V_{min} $(Q = 1)$	510 cm^{-1}

[a] See Equations 3.9 and 3.11 and the text.

[b] From B3LYP 6-31G electronic structure calculation.

[c] From reference 117.

Figure 3.12 shows a pair of model potentials for the ZnTMPyP-CH_3OH intermolecular mode that illustrates the effect of turning on the charge-dependent terms in Equation 3.11 and of changing the intermolecular distance. The only parameter in the intermolecular potential that is not known from the literature, from a calculation, or from experiment is that for the exchange interaction, a, but it can be estimated given an experimental measurement of the mode frequency and an initial assumption of $Q = 0$ so that the charge-dependent terms are inactive. Combination of Equations 3.9 and 3.10 and the observed mean frequency of 79 cm^{-1} (see Table 3.2) returns a value for a of 76.2 eV $Å^{12}$; the rest of the parameters used in Figure 3.12 are listed in Table 3.5 along with estimates for the equilibrium bond distance, r_{eq}, and the bond-dissociation energy, V_{min}, with $Q = 0$ and $Q = 1$. If a is held constant, the effect of changing Q from 0 to 1 is a sharpening of the potential near the minimum, which indicates an increased mode frequency, almost a doubling of V_{min}, and a modest 0.07 Å reduction in r_{eq} (compare curves (a) and (b) in Figure 3.12). Curve (c) in Figure 3.12 shows the magnitude of the charge-dependent terms in Equation 3.11, as calculated for the $Q = 1$ potential. This curve can be used to gauge the contribution of the charged terms to the stabilization and mode frequency when the charges are located at some distance from the clustered solvent molecules. The ones that interact with the π-electron density in the ground state are those that contribute to the ground-state vibrational coherence, and on average these solvent molecules are constrained to be more than 2.5 Å from the charges on the N-methylpyridyl rings. This distance estimate is based on the assumption that the charge is localized on the nearest carbon atom of the N-methylpyridyl ring and that the solvent molecule is fixed at r_{eq} for the $Q = 0$ case normal to the porphyrin ring above the adjacent *meso* carbon atom, to which the N-methylpyridyl rings are attached. At this distance, the charge-dependent terms account for a 70-cm^{-1} stabilization, about 25% of V_{min} for $Q = 0$. Given that the charge is actually delocalized over the N-methylpyridyl ring in

the ground state, the integrated interaction energy will be considerably smaller than this worst-case estimate. We conclude that it is a good approximation to neglect the charge-dependent terms in the ground-state intermolecular potential. In the excited state, because the π-electron density is extensively delocalized from the porphyrin region onto the N-methylpyridyl rings, the intermolecular mode frequency should be significantly increased from that in the ground state owing to a larger contribution of the charge-dependent terms in Equation 3.11.

The expression for the intermolecular mode frequency in the absence of charge-dependent terms, Equation 3.10, can be simplified to give a relation for the dependence on the dipole moment of the solvent as

$$\nu = (C_1 + C_2|\mu_2|^2)^{7/6} \tag{3.12}$$

where C_1 and C_2 are constants. This expression follows directly from Equation 3.10 with the assumption that all of the parameters other than the dipole moment of the solvent molecule are fixed; a simpler, approximate form was used in the previous work on BChl solutions.[63] Figure 3.11 plots the mean frequency of the rapidly damped components observed in the ZnTMPyP solutions as a function of the gas-phase dipole moment of the solvent. The mode frequency increases as the dipole moment increases in a manner that is consistent with the form of Equation 3.12. The fit of the mode frequencies to Equation 3.12 extrapolates to a mode frequency near 70 cm^{-1} in the nonpolar limit. As anticipated in the Introduction, this y-intercept value is significantly lower than the value of ~100 cm^{-1} observed in BChl solution. ZnTMPyP's four-fold symmetry results in a dipole moment of zero in the plane of the porphyrin; the out-of-plane doming of the Zn^{II} ion due to the axial coordination of a solvent ligand results in a small dipole-moment component orthogonal to the plane of the porphyrin (0.66 D, as obtained from the B3LYP 6-31G electronic structure calculation for the methanol complex, see Figure 3.1). The dipole moment of BChl is significantly larger (3.6 D,[118] so the $\alpha_2|\mu_1|^2$ induction term in Equations 3.9

and 3.10 that contributes to the y-intercept constant C_1 in Equation 3.12 is more than 25 times smaller for ZnTMPyP since this term scales as the square of the dipole moment. The remaining term in Equations 3.9 and 3.10 that contributes to the y-intercept term of Equation 3.12 is the London-dispersion term, $b\alpha_1\alpha_2$. Thus, a great deal of the residual 70 cm^{-1} of the y-intercept value obtained for ZnTMPyP is due to the London-dispersion term. This conclusion is consistent with the general observation that the dipole-dipole and London-dispersion terms in the intermolecular potential are perhaps 10 times larger than either of the induction terms.[113-116]

Some of the molecular details of the interaction between ZnTMPyP and the surrounding solvent are suggested by deviations from the fitted curve shown in Figure 3.11 and by the dependence of the resonance Raman activity for the intermolecular mode on the solvent. The reduction of Equation 3.10 to Equation 3.12 requires that the polarizability α_2 for the solvent molecule is constant as the dipole moment μ_2 varies. The dispersion of the points for the solvents DMSO, CH_3CN, and DMF from the fitted curve in Figure 3.11 suggests a possible contribution of the solvent polarizability in the strength of the intermolecular interaction with the ZnTMPyP solute. These solvents have similar dipole moments, yet the mean frequency of the intermolecular mode varies in them over the 95-125-cm^{-1} range, a span of about one-fifth of the mean value. The increase of the mean frequency from that observed in methanol (α_2 = 3.29 $Å^3$ [117]), 79 cm^{-1}, to that for acetonitrile (α_2 = 4.4 $Å^3$ [117]), 106 cm^{-1}, depends mostly on the induction term $\alpha_1|\mu_2|^2$ since the dipole-dipole term $c|\mu_1|^2|\mu_2|^2$ is relatively small owing to the small dipole moment of ZnTMPyP. The induction term is relatively large in porphyrin and BChl solutions because of the large polarizabilities (α_1) of these solutes. The difference between the mean frequency observed in acetonitrile and DMSO (α_2 = 8.87 $Å^3$ [119]), however, probably arises largely from the enhanced polarizability of the sulfonyl group over that of the carbonyl. Further, the decreased mean frequency in DMF (α_2 = 7.81 $Å^3$ [117]) has

to be attributed to a specific solvent effect that decreases the strength of the intermolecular interaction given that the polarizability of DMF is almost as large as that of DMSO.

The solvent dependence of the *amplitude* of the rapidly damped modulation components (see Table 3.2) suggests that the resonance Raman intensity enhancement for the intermolecular mode partly depends on the covalency of the interaction, the degree to which the π-electron density of the solute chromophore is mixed with that of the clustered solvent molecule. The use of a van der Waals potential to follow trends in the mode frequency invokes a purely electrostatic picture, of course, but some involvement of covalency is suggested by the observation that the strongest modulation amplitudes occur in CH_3CN and DMSO, which feature cyanide/nitrile and sulfonyl groups, respectively. This observation follows the same trend observed with *Q*-band excitation of polar solutions of BChl; the amplitude of the intermolecular vibrational coherence was strongest by far in pyridine solution.[63] As mentioned above, DMF seems to be an outlier; the intermolecular modes in DMF and CH_3OH have comparable amplitudes even though the former contains delocalized π-electron density over the amide group. It follows that both the Albrecht A- and B-terms[120,121] contribute to the resonance Raman intensity. The A-term would primarily include effects from the change of shape and extent of the π-electron density that yield a gradient in the excited-state potential-energy surface in the Franck-Condon region, whereas the B-term would include couplings of the excited state to nearby states. The part of the A-term enhancement that arises from the redistribution of π-electron density in ZnTMPyP's excited state (see Figure 3.1) is likely to be small given that the intermolecular modes are easily observed in BChl, which lacks a comparable ground-to-excited-state displacement of electron density.

3.5.1 Conclusions

The results discussed in this chapter support the hypothesis that intermolecular modes between porphyrin or chlorophyll macrocycles and clustered molecules in the first shell of solvent contribute the most intense components to the low-frequency (0–300-cm^{-1}) vibrational coherence in polar media. The corresponding mode frequencies fall in the right range to account for the modes that dominate the Marcus reorganization energy for electron-transfer reactions in photosynthetic reaction centers. In comparison to the intermolecular modes, the intramolecular modes from the porphyrin or chlorophyll macrocycle account for features in the vibrational coherence that are at least an order of magnitude weaker. Further, an analysis of the electronic structure of ZnTMPyP suggests that there should be a significant ground-to-excited-state change in the mode frequency and stabilization of the intermolecular modes owing to the change in shape of the π-electron density. The contribution of ion–dipole and ion–induced-dipole terms to the intermolecular potential in the excited state of ZnTMPyP should result in a significantly higher intermolecular mode frequency. These projections suggest an important role for intermolecular modes between the prosthetic groups and their first-solvation-shell surroundings in the stabilization of the charged intermediate and product species that occur in proteins during redox catalysis.

CHAPTER 4

Excited-state vibrational coherence in methanol solution of Zn^{II} tetrakis(N-methylpyridyl)porphyrin

4.1 Summary

We have employed femtosecond dynamic-absorption spectroscopy to observe excited-state wavepacket motions in Zn^{II} *meso*-tetrakis(N-methylpyridyl)porphyrin (ZnTMPyP) in methanol solution. The pump-probe transients observed in ZnTMPyP solution with Q-band excitation exhibit a net excited-state absorption character. The signals are weakly modulated by slowly damped (effective damping time γ>1.5 ps) components that correspond to skeletal normal modes of the porphyrin macrocycle, but by far the dominant modulation features are a pair of rapidly damped (γ<400 fs) components arising from intermolecular modes with first-shell solvent molecules. The 256 cm^{-1} mean frequency of the rapidly damped components is significantly higher than observed previously in the ground state, 79 cm^{-1}. This increase in frequency arises from an extensive delocalization of the π-electron density from the

porphyrin region to the singly charged N-methylpyridyl rings. In the excited state, the van der Waals intermolecular potential accordingly obtains large ion-dipole and ion-induced-dipole terms that account for the increased mode frequency and result in a significant stabilization of the equilibrium structure. These results suggest an especially important functional role for the intermolecular modes between the redox chromophores and the surrounding protein medium in photosynthetic reaction centers that involves trapping of charged intermediates.

4.2 Introduction

The observation of vibrational coherence in femtosecond pump-probe experiments with impulsive excitation of electronic chromophores in solution[24,26,29,33,35,122,123] is usually associated with resonance Raman activity arising from an excited-state displacement of a small number of skeletal normal modes of the chromophore. In several classes of proteins where light-induced chemistry occurs, vibrational coherence in the skeletal modes of a prosthetic group is associated with the reaction coordinate. Shank, Mathies, and coworkers characterized coherent wavepacket motion in retinal's torsional modes associated with formation of the photoisomerization product state in bacteriorhodopsin and rhodopsin.[26,32,36,39-42] Champion and coworkers observed an analogous reaction-driven vibrational coherence in the ground-state out-of-plane porphyrin modes in myoglobin and cytochrome *c* following photodissociation of axial ligands.[53,55,61] Martin, Vos, and coworkers[124] have observed vibrational coherence in cytochrome *c* oxidase aa_3 upon photolysis and transfer of carbon monoxide from heme a_3 to Cu_B. The excited-state vibrational coherence observed by Vos and Martin from the primary electron donor, P, in the purple-bacterial photosynthetic reaction center,[43-51] however, is likely to involve modes that are derived from the surrounding protein medium[1,22] rather than

just from the paired bacteriochlorophyll (BChl) chromophore itself.[73,125,126] Because of their low frequencies, the modes would be expected to be delocalized over the protein structure spanning the reaction center's chromophores just as phonons are in molecular crystals.[43,45,50]

In the previous chapters, we discussed how the ground-state vibrational coherence observed in solutions of BChl and of Zn^{II} *meso*-tetrakis(N-methylpyridyl)porphyrin (ZnTMPyP) suggest, in contrast, that by far the strongest contributions to the vibrational coherence in the 100-cm^{-1} regime arise from localized intermolecular modes with clustered, first-shell solvent molecules.[63-65,88] The pump-probe signals observed with *Q*-band excitation of BChl in polar solvents are modulated by rapidly damped (time constant γ<200 fs) components that shift to higher frequencies as the dipole moment of the solvent increases. The mean frequency of these modulation components follows the natural frequency of a van der Waals intermolecular potential that contains dominant contributions from the London-dispersion and dipole-dipole interactions.[63] The slowly damped ($\gamma \geq 2000$ fs) modulation components that arise from the skeletal modes of the BChl macrocycle are perhaps ten times less intense than those from the solvent modes.[64] Similar assignments were made for the ground-state vibrational coherence observed in polar solutions of ZnTMPyP with Soret-band (420-nm) excitation. The normal modes of the porphyrin macrocycle and its single solvent-derived axial ligand contribute very slowly damped features to the vibrational coherence, some of which persist even to the 20-ps delay point. The rapidly damped, solvent-dependent modes again account for the dominant features. The dependence of the mean frequency of the rapidly damped components follows an intermolecular potential that exhibits a lower mode frequency in the nonpolar limit than observed in BChl (70 cm^{-1} and 120 cm^{-1}, respectively), and an isotope-dependent shift was observed when the signals from methanol and perdeuterated methanol were compared. The magnitude of the shift

indicates that the intermolecular modes arise in methanol solution predominantly from 1:1 complexes with the porphyrin solute.[88]

The intermolecular potential used in the discussion of the ground-state vibrational coherence in BChl and ZnTMPyP solutions includes only the terms that arise from the polarizability and dipole moment of the neutral solute and solvent. In ZnTMPyP, the π-electron density in the ground state is confined to the porphyrin macrocycle (see Figure 3.1a), so an attacking solvent molecule does not strongly sense the positive charges on the peripheral N-methylpyridyl rings. In the π^* excited states (see Figure 3.1b), however, the π-electron density is extensively delocalized from the porphyrin over two of the N-methylpyridyl rings, so the intermolecular potential between ZnTMPyP and clustered solvents should gain ion-dipole and ion-induced-dipole terms. These charge-dependent terms would be expected to contribute to a significant shift to higher frequency for the intermolecular oscillator. We have put these ideas to the test in this chapter. We show that pump-probe signals obtained with Q-band excitation of ZnTMPyP monitor excited-state wavepacket motions owing to detection of a net excited-state absorption signal. As expected, the rapidly damped portion of the vibrational coherence shifts to a much higher frequency than observed in the ground-state vibrational coherence observed with Soret-band excitation. These results advance the hypothesis that resonance Raman-active intermolecular modes with first-solvation-shell components contribute dominantly to the low-frequency vibrational coherence in porphyrin and BChl systems. We conclude with a brief discussion of how the charge-dependent terms in the intermolecular potential should play an important role in the trapping of charge-separated intermediates in the photosynthetic reaction center.

4.3 Experimental

4.3.1 Sample Preparation

ZnTMPyP (CAS 28850-44-4) was used as received from Frontier Scientific. Methanol (CH_3OH, spectrophotometric grade) was obtained from Sigma-Aldrich. For use in femtosecond pump-probe experiments, solutions of ZnTMPyP were prepared by dissolving the dry ZnTMPyP powder in methanol to obtain an absorbance of 0.4 for a path length of 1.0 mm at the center of the laser spectrum at 625 nm, as detailed below. The solution was passed through a 0.22-m filter prior to checking the absorbance. The samples were held in the femtosecond pump-probe spectrometer at room temperature (23 °C) in a fused-silica flow cuvette (0.5-mm path length). A peristaltic pump was used to circulate a 10-mL reservoir of sample solution through the cuvette at 2.70 mL/min. The sample's absorption spectrum was monitored during the experiment for changes arising from photochemistry or permanent photobleaching. The sample reservoir was exchanged with fresh solution several times during each run.

4.3.2 Continuous-Wave Absorption and Fluorescence Spectroscopy

Absorption spectra were obtained at 23 °C with a Hitachi U-2000 spectrophotometer (2-nm bandpass). Fluorescence spectra were acquired at 23 °C with a Hitachi F-4500 spectrofluorimeter (5-nm bandpass for the excitation and emission monochromators). As presented as a function of wavenumber, the fluorescence intensities are multiplied by the square of the wavelength in order to compensate for the fixed (in wavelength units) spectral bandpass of the emission spectrometer.[89]

4.3.3 Femtosecond spectroscopy

Femtosecond pump-probe transients with impulsive excitation were recorded using the dynamic-absorption technique, in which the probe beam is dispersed in a grating monochromator after passing through the sample.[32,33,35-37] Most of the instrumentation and methodology is similar to that described in the previous work on ZnTMPyP solutions with Soret-band excitation.[88] In this work, however, the pump and probe pulses were obtained from the signal-beam output of an optical parametric amplifier (Coherent OPA 9450), which was pumped by an amplified Ti:sapphire laser (Coherent Mira-seed oscillator and a modified Coherent RegA 9050 regenerative amplifier, with Coherent Verdi V5 and V10 pump lasers, respectively). The laser was operated at a repetition rate of 250 kHz. The experiments were conducted with 13-nJ, 45-fs pump and 7.2-nJ probe pulses centered at 625 nm (15 nm fwhm, as measured with an Ocean Optics USB-2000 spectrometer/CCD detector with a 0.5-nm bandpass).

The pump and probe pulses were corrected for group-delay dispersion on the way to the sample by a SF10 Brewster prism-pair pulse compressor. The pump-probe time delay was scanned using a rapid-scanning delay stage (Clark-MXR, ODL-150) in a modified Mach-Zehnder interferometer with confocal sample and autocorrelation-crystal positions. Calcite polarizers and $\lambda/2$-retarding wave plates in the pump and probe beams set their planes of polarization at 90°; after passing through the sample, the probe beam was analyzed by another calcite polarizer oriented 90° relative to the pump-beam's plane of polarization, and then it was passed through a monochromator (Spex 270M, 4-nm bandpass) and detected by an amplified photodiode (Thorlabs PDA55). The monochromator's slits were adjusted to obtain a fairly narrow bandpass (4 nm) compared to the width of the laser's spectrum; the monochromator's grating was detuned from the laser's intensity maximum to the ~50% intensity point. This approach is similar to that used by Champion and co-workers in their studies of low-frequency vibrational coherence in heme proteins.[53,55,61] The pump-probe

signal was obtained from the photodiode signal using a lock-in amplifier (Femto LIA-MV-200-H); the pump beam was modulated at 50 kHz by a $\lambda/4$-retarding photoelastic modulator (Hinds Instrumentation) with $\lambda/4$-retarding and $\lambda/2$-retarding waveplates and a calcite polarizer in series.

4.4 Results

Figure 4.1 shows continuous-wave absorption and fluorescence spectra from ZnTMPyP in methanol at 23 °C. The spectra are plotted as relative dipole strengths[89,91,92] as a function of wavenumber ν, $A(\nu)/\nu$ and $F(\nu)/\nu^3$ respectively. The fluorescence spectrum extends to the red from the 0–0 peak of the Q band, the absorption feature that corresponds to the first excited singlet (S_1) state. Also shown in Figure 4.1 is the output spectrum from the OPA as it was tuned to 625 nm for the dynamic-absorption experiments. Because we wanted to detect vibrational coherence from coherent wavepacket motion on the S_1 state's potential-energy surface, the OPA was tuned as far to the red in the Q band as possible so that the probe bandpass would detect a large stimulated-emission signal. As estimated from the dipole-strength spectra, at the 632-nm center of the probe bandpass the stimulated-emission (SE) signal is five times larger than the photobleaching (PB) signal.

The dynamic-absorption transient obtained from ZnTMPyP in methanol under these experimental conditions is shown in Figure 4.2. Following an intense bipolar spike that goes off the plotted scale near the pump–probe zero-delay point,[93–95] the transient exhibits a pattern of cosinusoidal modulations superimposed on a rising transient of net excited-state absorption (ESA) character. The oscillatory residual obtained by subtracting a fitted biexponential trend consists of a very rapidly damped portion over the 100–600-fs range followed by a more slowly damped part that persists at least to the 2000-fs range. This damping character is similar to that observed

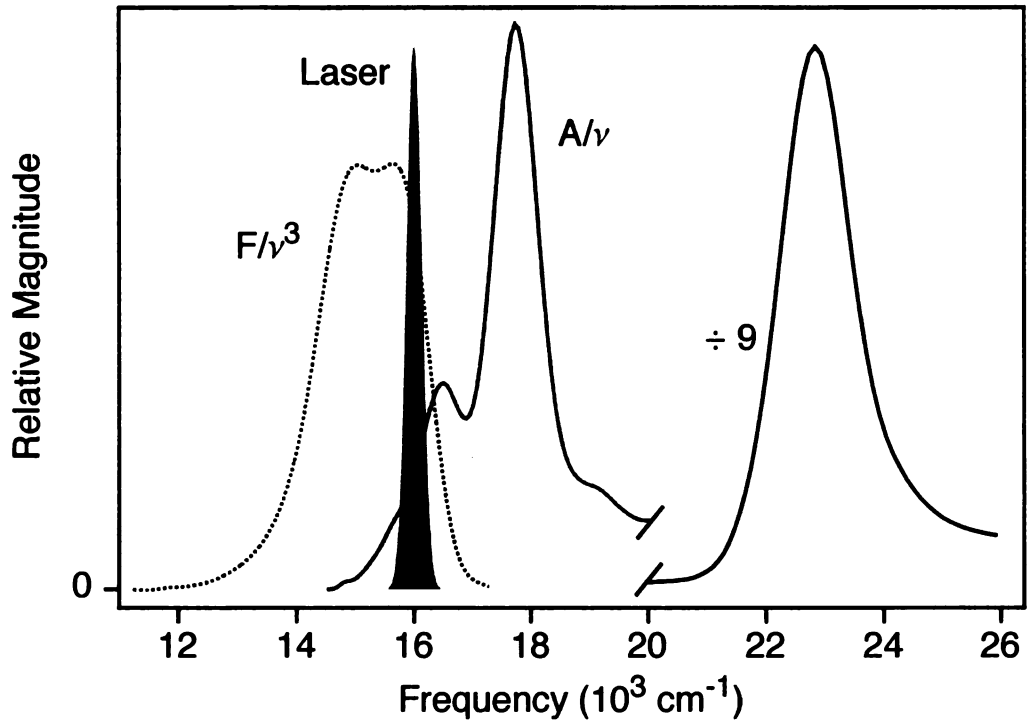

Figure 4.1. Soret (ν>20000 cm^{-1}) and Q-band region of the continuous-wave absorption (solid curve) and fluorescence (dotted curve) spectra from ZnTMPyP in methanol at room temperature (23 °C), plotted as the dipole strength, $A(\nu)/\nu$ and $F(\nu)/\nu^3$, respectively, and normalized to unit area for the fluorescence spectrum and Q band. Superimposed with arbitrary scaling is the intensity spectrum of the 625-nm, 45-fs pulses used in the pump-probe experiment.

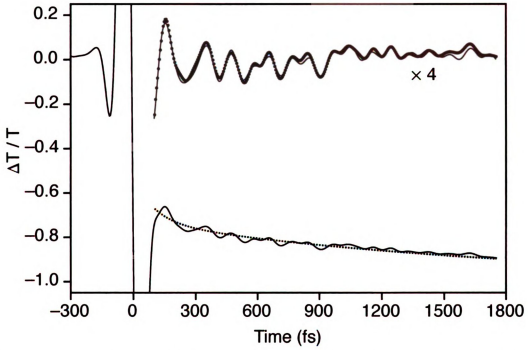

Figure 4.2. Femtosecond pump–probe dynamic absorption transient detected at 632 nm (4-nm bandpass) with ZnTMPyP in methanol. The pump-induced change in transmission signal ($\Delta T/T$) is shown superimposed on a double-exponential fit function (dashed curve) over the >100-fs delay range of the form $A_0(1+A_1e^{-t/\tau_1}+A_2e^{-t/\tau_2})$, with $A_0 = 3.00 \times 10^{-3}$, $A_1 = 0.204$, $\tau_1 = 98$ fs, $A_2 = 0.272$, and $\tau_2 = 1.8$ ps. As plotted, the signal is normalized by dividing by the nondecaying fraction, A_0. The oscillatory residual, the difference between the signal and the fit function, is shown above the signal superimposed on a model composed of slowly and rapidly damped oscillatory components (see Figure 4.3 and Tables 4.1 and 4.2).

in polar solutions of BChl and in polar solutions of ZnTMPyP with Soret-band excitation.[63,88]

After truncation of the <100-fs portion to avoid consideration of the spike near time zero,[95] the oscillatory residual was fit in the time domain to a model consisting of a sum of damped cosinusoids of the form

$$I_i(t) = A_i e^{-t^2\sigma_i^2/2} \cos(\omega_{0i}t - \phi_i) / \sqrt{2\pi} \tag{4.1}$$

with each component i having a center frequency ω_{0i} and phase ϕ_i. These waveforms correspond to Gaussian line shapes in the frequency domain,

$$I_i(\omega) = A_i e^{-(\omega-\omega_{0i})^2/(2\sigma_i^2)} / (\sigma_i\sqrt{2\pi}) \tag{4.2}$$

where the linewidth is controlled by the standard deviation, $\sigma_i = \Delta\omega_i/2\sqrt{2\ln 2}$, with $\Delta\omega_i$ representing the full width at half maximum. Equations 4.1 and 4.2 are normalized so that the amplitude A_i corresponds to the area of the lineshape in the frequency domain and to the intensity of the signal in the time domain. Except as noted in the following, the fitting procedure was described in detail in the chapter on the ground-state vibrational coherence from ZnTMPyP.[88] The fit is shown superimposed on the residual's data points in Figure 4.2.

Starting parameters for the slowly damped components ($\Delta\omega$<10 cm^{-1}) were obtained from a Hanning-windowed Fourier-transform spectrum (see Figure 4.3a). The window function suppresses the rapidly damped portion of the signal and applies linebroadening to the slowly damped components. The twelve most intense peaks in the Fourier-transform spectrum were included in the model. The fit parameters for the slowly damped components are listed in Table 4.1.

The remaining, rapidly damped ($\Delta\omega$>10 cm^{-1}) part of the oscillatory residual was then modeled as the sum of two broad Gaussian components. The fit was not improved by inclusion in the lineshape of an asymmetry or skew parameter,

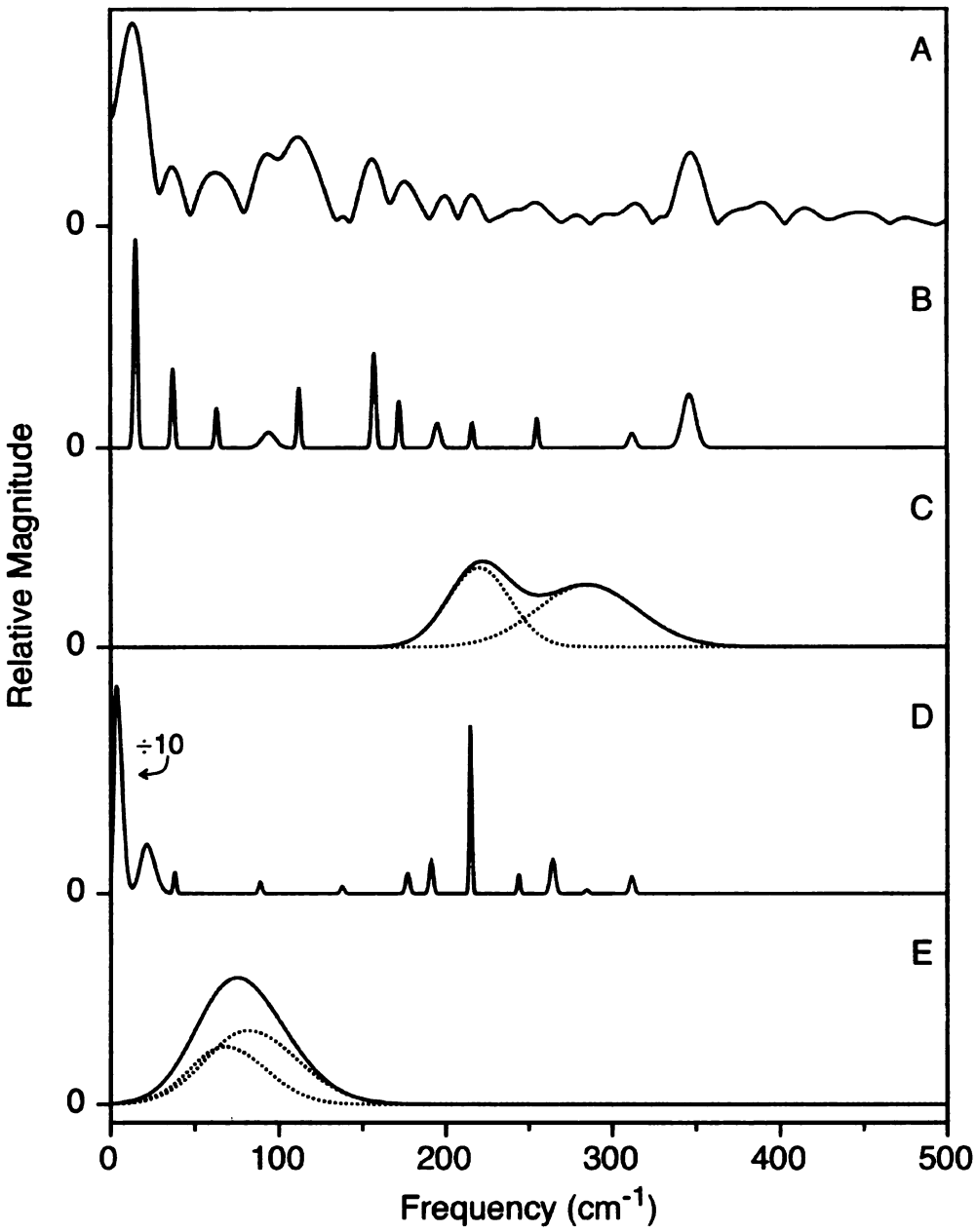

Figure 4.3. Comparison of the intensities and lineshapes observed in the excited-state and ground-state vibrational coherence from ZnTMPyP in methanol. *Excited state*, from the 625-nm pump-probe signal, see Figure 4.2: (a) Hanning-windowed, Fourier-transform magnitude spectrum; spectra for (b) the slowly damped ($\Delta\omega$<10 cm^{-1}) and (c) the rapidly damped ($\Delta\omega$>10 cm^{-1}) components from the time-domain model. *Ground state*, from the 420-nm pump-probe signal, from reference 88): spectra for (d) the slowly damped ($\Delta\omega$<10 cm^{-1}) and (e) the rapidly damped ($\Delta\omega$>10 cm^{-1}) components from the time-domain model. In (c) and (e), the sum of the two rapidly damped components (dotted lines) is shown as the solid trace. The scaling factor for (d) and (e) is 1.6 times smaller than that for (b) and (c).

Table 4.1. Gaussian lineshape parameters for the slowly damped modulation components obtained from the 625-nm pump-probe transient from ZnTMPyP in methanol (see Figure 4.2).

Component	ω_0 (cm^{-1})	$\Delta\omega$ (cm^{-1})	Amplitude[a]
1	15	2.55	2.84
2	37	2.36	1.00
3	63	2.35	0.507
4	94	9.41	0.776
5	112	9.41	0.761
6	157	2.77	1.42
7	172	2.35	0.597
8	195	4.61	0.597
9	216	2.35	0.313
10	255	2.35	0.373
11	313	4.66	0.358
12	346	9.04	2.54

[a] Normalized relative to component 2, which has an amplitude of 6.72×10^{-3} relative to the fitted nondecaying fraction, A_0 (see Figure 4.2).

Table 4.2. Gaussian lineshape parameters and effective exponential damping times for the rapidly damped modulation components obtained from the 625-nm pump-probe transient of ZnTMPyP in methanol (see Figure 4.2).

Component	ω_0 (cm^{-1})	$\Delta\omega$ (cm^{-1})	γ (fs)[a]	Amplitude[b]
1	220	44.0	309	17.9
2	285	70.8	193	22.4

[a] Damping time of best-fit exponentially damped cosinusoid (see Equation 4.3).
[b] Normalized relative to the 37-cm^{-1} slowly damped component (see Table 4.1).

as was previously required in the modeling of the rapidly damped ground-state components.[88] The two components are assigned, in order of frequency, to the hindered translational and librational (hindered rotational) intermolecular modes between the porphyrin macrocycle and its clustered, first-solvation-shell solvent molecules.[63,88] The fit parameters for these components are listed in Table 4.2. Also included in Table 4.2 are effective damping times γ for a best-fit exponentially damped cosinusoid of the form

$$I_i(t) = A_i\, e^{-t/\gamma_i} \cos(\omega_{0i} t - \phi_i) \tag{4.3}$$

which corresponds in the frequency domain to a Lorentzian line shape. The tabulated values of γ were obtained as previously described by fitting each Gaussian component in the model individually to Equation 4.3. This procedure provides a rough estimate of the lower limit for the damping time.[88]

Figures 4.3b and c show frequency domain representations of the slowly and rapidly damped portions of the optimized model. These spectra should be compared to Figures 4.3d and e, which show spectra for the slowly and rapidly damped components in the ground-state vibrational coherence.[88] The rapidly damped components in Figure 4.3c are clearly shifted to a much higher frequency from those in Figure 4.3e. From the sum of the two underlining component lineshapes (see Figure 4.3c and e), $\mathcal{M}(\omega) = I_1(\omega) + I_2(\omega)$, the mean frequency was obtained using a normalized mean-value relation,

$$\langle \omega \rangle = \frac{\int_0^\infty d\omega\, \mathcal{M}(\omega)\omega}{\int_0^\infty d\omega\, \mathcal{M}(\omega)} \tag{4.4}$$

The mean frequency of the sum of the two rapidly damped components shown in Figure 4.3c is 256 cm^{-1}, whereas the mean frequency for those in Figure 4.3e is 79 cm^{-1}.

4.5 Discussion

The pump-probe signal from ZnTMPyP with Q-band excitation at 625 nm is modulated primarily by coherent wavepacket motions on the S_1-state potential-energy surface. This assignment is based on the tuning of the laser spectrum, the choice of the detected probe bandwidth (see Figure 4.1), and the observation of a rising net ESA signal that persists to the end of the recording. This result is consistent with the observations of Fontaine-Aupart and coworkers,[103] who observed a long-lived ESA signal at probe wavelengths above 575 nm in their pump-continuum-probe time-resolved spectra. The laser was tuned so that the red side of the laser spectrum, where the probe bandpass was selected, overlaps favorably with the stimulated-emission spectrum (see Figure 4.1). Owing to the 5:1 SE:PB ratio, as judged from the ratio of the continuous-wave fluorescence and absorption dipole strengths centered at the detected probe bandpass, respectively, and because the strength of the ESA part of the signal is larger than of the sum of the photobleaching and stimulated-emission parts, we estimate that ground-state wavepacket motions make less than a 10% contribution to the pump-probe signal. The SE and ESA signals are synchronously modulated by the S_1-state wavepacket.

The pattern of modulation intensities observed in Figure 4.3a and b is fully consistent with an assignment to excited-state coherent wavepacket motions. These slowly damped ($\gamma > 1.5$ ps, $\Delta\omega < 10$ cm^{-1}) features are assigned to the skeletal normal modes of the ZnTMPyP molecule. In systems where the ground- and excited-state potential-energy surfaces are displaced with respect to the coordinate of the vibrational mode, moving wavepackets on the ground- and excited-state potential surfaces are launched by two successive actions of the pump field.[24-26,33] The ground-state wavepacket is created by a process that directly corresponds to resonance Raman scattering. The pump-probe signal is modulated optimally by ground-state wavepacket motion when the pump-pulse duration is about one-third of the mode's period.[26] As we explained

previously, the ~222-cm^{-1} maximum observed in the intensity profile of the slowly damped features detected with Soret-band excitation (see Figure 4.3d) is consistent with an assignment to ground-state wavepacket motions because of our use of 50-fs pump pulses in that experiment.[88] In contrast, for excited-state wavepacket motion, the amplitudes are expected to increase monotonically as the frequency decreases.[26] The intensity profile indicated by Figure 4.3b is obviously consistent with this trend.

The main exception to the expectation that the intensities for the excited-state wavepacket motions should decrease smoothly with increasing mode frequency is the relatively intense 346-cm^{-1} peak, which is assigned to an an out-of-plane deformation mode localized on the N-methylpyridyl rings based on assignments of peaks at similar frequencies in continuous-wave resonance Raman spectra of ZnTMPyP and other N-methylpyridyl porphyrins.[127] The strength of the 346-cm^{-1} peak is especially notable considering our use of 45-fs pump and probe pulses, which lack enough impulsive bandwidth to make observation of modulation features above 300 cm^{-1} facile. Note also that the relatively intense 3-cm^{-1} component observed in the ground state vibrational coherence (Figure 4.3d) but apparently absent from the excited-state vibrational coherence (Figure 4.3b) arises from internal rotation of the N-methylpyridyl rings with respect to the porphyrin. In the ground state, this motion is relatively unhindered because the π-electron density is confined to the porphyrin region (see Figure 3.1a); in the excited state, the π-electron density is extensively delocalized from the porphyrin to the rings (see Figure 3.1b), so the resulting partial double-bond character strongly damps internal rotation.

Except for the 3-cm^{-1} and 346-cm^{-1} peaks discussed above, the frequencies of the components observed in the slowly damped excited-state vibrational coherence (Figure 4.3b) correlate well with those observed in the ground-state vibrational coherence signal (Figure 4.3d). Most of these modes arise from out-of-plane deformations of the porphyrin macrocycle. The 37-cm^{-1} and 216-cm^{-1} components are

assigned to the metal-doming and Zn^{II}-axial-ligand stretching modes, respectively. The excited-state mode frequencies for these components differ by less than one cm^{-1} from the frequencies observed in the ground state.[88]

The rapidly damped (γ<400 fs, $\Delta\omega$>15 cm^{-1}) features shown in Figure 4.3d and e correspond to the intermolecular modes between the ZnTMPyP molecule and first-shell solvent molecules. In the excited state, the mean frequency of the summed intensity of these features is 256 cm^{-1}. This frequency is substantially higher than the ground-state mean frequency of 79 cm^{-1}. This increase is consistent with the van der Waals intermolecular potential we introduced previously in our discussion of the trend of the ground-state frequency as a function of the dipole-moment of the solvent molecule.[88] In the ground state of ZnTMPyP, because the π-electron density is confined to the porphyrin ring (see Figure 3.1), the intermolecular potential can be expressed as

$$V_0(r) = a/r^{12} - \left(b\alpha_1\alpha_2 + \frac{c|\boldsymbol{\mu}_1|^2|\boldsymbol{\mu}_2|^2}{(4\pi\varepsilon_0)^2} + \frac{\alpha_2|\boldsymbol{\mu}_1|^2 + \alpha_1|\boldsymbol{\mu}_2|^2}{4\pi\varepsilon_0}\right) \Big/ D^2 r^6 \qquad (4.5)$$

As shown previously,[63] a Taylor series expansion of Equation 4.5 around the equilibrium geometry gives an expression for the natural frequency of the intermolecular mode,

$$\nu = \frac{3}{(2a)^{2/3}} \left(b\alpha_1\alpha_2 + \frac{c|\boldsymbol{\mu}_1|^2|\boldsymbol{\mu}_2|^2}{(4\pi\varepsilon_0)^2} + \frac{\alpha_2|\boldsymbol{\mu}_1|^2 + \alpha_1|\boldsymbol{\mu}_2|^2}{4\pi\varepsilon_0}\right)^{7/6} \Big/ 2\pi D^{7/3}\mu^{1/2} \qquad (4.6)$$

In the above equations, the constant a scales the Pauli exchange interaction, b scales the London-dispersion interaction, $c = 2/3\, k_B T$ scales the dipole–dipole interactions, and the $\alpha_2|\boldsymbol{\mu}_1|^2$ and $\alpha_1|\boldsymbol{\mu}_2|^2$ terms correspond to dipole–induced-dipole interactions (see Table 4.3).[113-116] In these equations, $\boldsymbol{\mu}_i$ and α_i correspond to the dipole moment and polarizability for the solute (subscript 1) and solvent (subscript 2); r is the distance between the two molecules, μ is the reduced mass for the intermolecular oscillator, D represents the dielectric constant for the solvent, and ε_0 relates the permittivity of free space. As expressed above, the dipole-dependent terms apply to the

high-temperature limit, where k_BT is much greater than the well depth, so the interaction is averaged over all orientations.[115] Since the well depth for ZnTMPyP-CH_3OH in the ground state (see Table 4.3 and reference 88) is 286 cm^{-1} at T=298 K, the assumption that it is appropriate to average the interaction energy over all orientations may not be valid.

In the excited state, the π-electron density is extensively delocalized from the porphyrin region to the N-methylpyridyl rings (see Figure 3.1), so the formal charges on the rings are also delocalized. As noted previously,[88] the intermolecular potential should be expanded to include two additional solute-charge-dependent terms corresponding to the ion-dipole and ion-induced dipole interactions with the charge Q:

$$V_Q(r) = V_0 - \left(\frac{cQ|\mu_2|^2}{(4\pi\epsilon_0)^2} + \frac{\alpha_2 Q^2}{4\pi\varepsilon_0}\right) \Big/ 2D^2r^4 \qquad (4.7)$$

Both of the new terms are attractive; the ion-dipole term depends linearly on the charge Q of the solute and on the square of the solvent's dipole moment, μ_2; the ion-induced-dipole term contains the polarizability α_2 of the solvent and the square of the charge, Q^2. Both terms depend on r^{-4}, so the potential expands to much larger intermolecular distances than does the neutral potential (Equation 4.5). Thus, inclusion of the charge-dependent terms causes the potential to extend to much greater intermolecular distances than does the neutral potential. The relation for the natural mode frequency that follows from Equation 4.7 is not shown here owing to its length, but it predicts that the mode frequency should significantly increase over that predicted by Equations 4.5 and 4.6. Equation 4.7 also predicts that the depth of the potential well will increase significantly over that predicted from the neutral potential (Equation 4.5), so the assumption of orientational averaging made for the uncharged case is no longer valid, and the result would be an even more stable structure for the porphyrin-solvent van der Waals complex.

Figure 4.4 shows three model curves for the ZnTMPyP-CH_3OH intermolecular mode to illustrate the effect of adding charges to the intermolecular potential. Most

of the parameters in Figure 4.5 and 4.7 are obtained from the literature (see Table 4.3). The coefficient of the exchange interaction, a, can be estimated given the experimental measurement of the ground-state mode frequency (79 cm^{-1}) and the assumption that $Q = 0$ in the ground state so that the charge-dependent terms do not contribute to the intermolecular potential. In the excited state, the π-electron density extends over two of the N-methylpyridyl rings, so it is reasonable to suppose that two charges are introduced. As Q increases from 0 to 2, the potential-well depth V_{min} increases by almost a factor of five but the equilibrium bond length r_{eq} experiences only a ten percent contraction (0.18 Å). The potential well sharpens significantly as Q increases, so the intermolecular mode will accordingly increase in frequency. The predicted mode frequency for the $Q = 2$ case obtained from Equation 4.7 is 168 cm^{-1}, which is about two-thirds of the mean frequency determined from the rapidly damped components shown in Figure 4.3c, 256 cm^{-1}. A better prediction of the excited-state mode frequency would be obtained from a improved potential that includes explicitly the excited-state charge distribution and employs a molecular dynamics simulation to gauge the distribution of solvent–solute interaction distances and orientations.

4.5.1 Conclusions

The ground-to-excited-state increase in the frequency of the intermolecular mode between ZnTMPyP and its first-shell solvent molecules allows firm conclusions about the nature of the intermolecular potential and the nature of the coupling of the mode to the $\pi \rightarrow \pi^*$ transition. First, the magnitude of the increase in the mode frequency shows the importance of charge-dependent terms in the intermolecular potential relative to the nonpolar dipole-dependent terms. The effective absence of the charge-dependent terms in the intermolecular potential detected in the ground state further suggests that the solvent molecules that contribute to the detected intermolecular

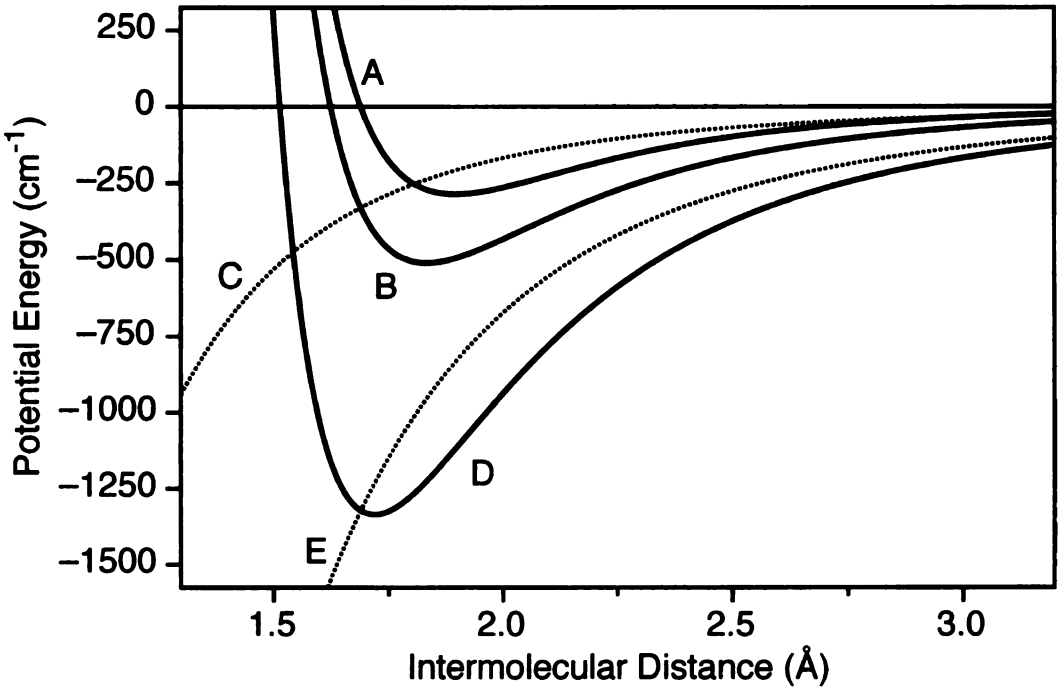

Figure 4.4. Model potential-energy curves for the ZnTMPyP-CH_3OH van der Waals complex as a function of the charge Q on the ZnTMPyP moiety: (a) $Q = 0$; (b) $Q = 1$; (c) the attractive, charge-dependent terms for $Q = 1$; (d) $Q = 2$ and (e) the attractive, charge-dependent terms for $Q = 2$. The curves were calculated using Equation 3.10 and the experimentally observed ground-state intermolecular mode frequency, 79 cm^{-1} (see reference 88). Table 4.3 lists the parameters and compares r_{eq} and V_{min} for curves (a), (b), and (d).

Table 4.3. Parameters for ZnTMPyP-CH_3OH intermolecular potentials (see Figure 4.4)

Parameters[a]	Symbol	Value
exchange (Pauli) interaction coefficient	a	76.2 eV Å^{12}
London-dispersion interaction coefficient	b	9.35 eV[b,c]
ZnTMPyP dipole moment	μ_1	0.663 D[b]
CH_3OH dipole moment	μ_2	1.70[b]
ZnTMPyP polarizability	α_1	109.8 Å^3 [b]
CH_3OH polarizability	α_2	3.29 Å^3 [c]
CH_3OH dielectric constant	D	33[c]
Equilibrium geometry with $Q = 0$	r_{eq}	1.90 Å
	V_{min}	286 cm^{-1}
Equilibrium geometry with $Q = 1$	r_{eq}	1.83 Å
	V_{min}	510 cm^{-1}
Equilibrium geometry with $Q = 2$	r_{eq}	1.72 Å
	V_{min}	1336 cm^{-1}

[a] See Equations 4.5-4.7 and the text.

[b] From B3LYP/6-31G calculation (see reference 88).

[c] From reference 117.

mode are those that directly contact the π-electron density. In the ground state, the π-electron density is essentially confined to the porphyrin region, so the charges on the N-methylpyridyl rings are not sensed by the solvent molecules that interact with the π-electron density. The extensive excited-state delocalization of the π-electron density over the N-methylpyridyl rings then turns on the charge-dependent terms that control the intermolecular mode frequency. These observations allow us to conclude further that the displacement of the intermolecular potential in the excited state that underlies the ground-state and excited-state wavepacket motions arises at least in part from the excited-state change of extent of the π-electron density; the expansion of the π electrons pushes the solvent molecules away from the frame of the porphyrin and launches the wavepacket motions.

These conclusions are significant because they imply that substantially increased activation and reorganization energies will be encountered for electron-transfer reactions in polar solution owing to the trapping of net charges by the intermolecular modes with the surrounding medium. A particular impact would be expected on the well depths of the intermolecular modes with first-shell groups that we suggest make dominant contributions to the reorganization energies for the electron-transfer reactions in photosynthetic reaction centers. The rate of the secondary electron-transfer reaction that shuttles the negative charge from $BPhe_L^-$ to Q_A in the purple-bacterial photosynthetic reaction center would be maximized by locating the $BPhe_L$ acceptor in a nonpolar region, as far as possible from polar or charged side chains. In contrast, the barriers for charge-recombination reactions are raised by placing the primary electron-donor *P* and the quinones Q_A and Q_B in polar regions of the reaction center. These structural features[73,125,126] clearly enhance the quantum efficiency of the two-step, transmembrane charge-transfer/energy-storage mechanism in the reaction center.

CHAPTER 5

Vibrational coherence in the native and molten-globule states of Zn^{II}-substituted cytochrome *c*

5.1 Summary

A crucial feature of the long-distance electron-transfer reactions in the purple-bacterial photosynthetic reaction center is that they exhibit activationless dynamics. In the previous chapters, we have advanced the hypothesis that van der Waals interactions between the redox-active chromophores and adjacent groups in the protein-derived medium account for the majority of the reorganization energy in these reactions and accordingly control the activation energy. In this chapter, we test several aspects of this hypothesis by characterizing the ground-state low-frequency vibrational coherence from Zn^{II}-substituted cytochrome *c* (ZnCytc) in the native and acid-induced molten-globule states using femtosecond dynamic-absorption spectroscopy. The vibrational coherence observed from the native state exhibits two types of components. The first type is a pair of slowly damped (damping time γ>1.5 ps) com-

ponents with frequencies of ~10 and ~30 cm^{-1} that are assigned to metal-doming modes with the M80 and H18 axial ligands. The second type is a strong, very rapidly damped (γ<150 fs) 79-cm^{-1} component that is assigned to van der Waals interactions with nonpolar groups from the surrounding protein. The resonance Raman activity of this set of modes is effectively quenched in the molten-globule state owing to the expansion of the hydrophobic core and to the randomization of the surrounding structure. These findings show that the van der Waals modes obtain resonance Raman activity through a direct attack of the neighboring groups upon the π-electron density of the Zn^{II} porphyrin. Similar interactions are likely candidates for the rate-controlling interactions in the photosynthetic reaction center.

5.2 Introduction

Perhaps the key feature that allows the purple bacterial photosynthetic reaction center to perform efficient conversion of solar photons into transmembrane chemical potential is that the electron-transfer reactions are optimized by the protein structure so that they occur with activationless dynamics. The rate of electron transfer is effectively independent of temperature in the theory of Bixon and Jortner because the reactions are coupled to displacements along vibrational modes of the intervening protein medium that supports the redox-active chromophores.[1,22] The temperature dependence of the rate constant for the primary electron transfer reaction, from the paired bacteriochlorophyll primary electron donor, P, to the bacteriopheophytin acceptor, $BPhe_L$, is modeled adequately when the mean frequency of the protein-derived modes lies in the 80–100 cm^{-1} regime.[20] The observation of vibrational coherence in the stimulated emission from P* in this frequency range by Vos, Martin, and co-workers[43-46,48-51,76] is probably consistent with the expectations of the

Bixon and Jortner theory but the structural assignment of the active modes has remained indeterminate.

Vos and Martin suggest that the modes that appear in the vibrational coherence in the reaction center are like the phonons of molecular crystals in being delocalized over the protein structure spanning the redox chromophores.[43,45,50] In the previous chapters, we raise an alternative hypothesis that the modes arise from van der Waals interactions: from localized, formally nonbonding interactions between the chromophores and groups in the first-solvation shell.[63-65,88] We have explicitly compared the interactions that occur in polar liquids to those of the solvent molecules that are coordinated in gas-phase clusters.[128] The vibrational modes arising from these intermolecular interactions contribute rapidly damped features to the ground-state and excited-state vibrational coherence observed in polar solutions of bacteriochlorophyll (BChl) and of Zn^{II} porphyrins. In comparison to the components arising from the slowly damped intramolecular (or skeletal) normal modes of vibration of the chromophores in the < 300-cm^{-1} regime, the intermolecular modes exhibit perhaps ten times the resonance Raman activity.[63-65,88]

The broad lineshapes observed in solution for the van der Waals modes arise predominantly from the inhomogeneously broaded ensemble of chromophore–solvent interactions in the first shell.[63,88] In a folded protein structure, the interactions between a chromophore and the neighboring protein-derived groups are formally analogous to the those observed in polar solution but are likely to be more highly ordered. Thus, the lineshape of a particular chromophore–protein interaction should exhibit a narrower lineshape. In this chapter, in order to test these hypotheses, we have characterized the ground-state vibrational coherence from Zn^{II}-substituted cytochrome *c* (ZnCytc) in the native state and in the molten-globule state. The structure of cytochrome *c* surrounds the intrinsic metalloporphyrin with an essentially nonpolar environment. The closest polar amino-acid residue lies at a distance of about 3 Å.

This arrangement suggests that the low-frequency vibrational coherence from the native state should be dominated by London-dispersion interactions with the nonpolar residues that are at closer range. In the molten-globule state, however, the loss of order and the expansion of the hydrophobic core should turn off the resonance Raman activity of the modes that contribute to the vibrational coherence in the native state.

The results allow a comparison of the spectrum of the vibrational coherence in the native and molten-globule states of ZnCytc with that observed from Zn^{II} porphyrins in polar solution. The main finding is that the rapidly damped component that dominates the vibrational coherence in the native state is completely absent in the vibrational coherence from the molten-globule state. We conclude that the protein-dependent changes in lineshape and intensity are consistent with the form of the van der Waals potential and the mechanism of resonance Raman activity we introduced previously.[63,65,88] The present results strongly support a structural assignment of the low-frequency modes that are active in photosynthetic reaction centers to van der Waals interactions, and we discuss briefly how the mean frequency of these interactions can be tuned by the introduction of polar residues to the environment of the redox-active chromophores.

5.3 Experimental

5.3.1 Sample Preparation

ZnCytc was prepared from horse-heart ferricytochrome FeCytc (see Figure 5.1) using the procedure developed in the Vanderkooi laboratory.[129] Liquid anhydrous hydrogen fluoride (Linde) was employed as the demetalating agent; the reaction was run on a home-built gas-handling system in Teflon reaction vessels. Metal reconstitution of the free-base Cytc product with Zn^{II} was performed in the presence of a 10-fold molar excess of zinc acetate (Sigma 379786-5G, 99.999%). The extent of

demetalation and metal-reconstitution reactions was monitored spectrophotometrically; the starting and product species are easily distinguished from each other in terms of the number and position of bands in the *Q*-band region of the absorption spectrum. ZnCytc product solutions were subsequently worked up using methods derived from those of Winkler and co-workers[130] and Kostić and co-workers.[131] After desalting, the protein was isolated by cation-exchange chromatography, first on a Whatman CM-52 column and optionally then on a Mono-S 4.6/100 PE FPLC column (GE Healthcare Life Sciences). Fractions corresponding to ZnCytc were equilibrated with a 25-mM sodium phosphate buffer solution at pH 6.9 by repeated concentration using an Amicon ultrafilter and dilution with the buffer solution. After a final ultrafiltration step, the product was analyzed on a Superdex 75 FPLC gel-filtration column (GE Healthcare Life Sciences). The eluent was monitored simultaneously at 280 and 420 nm. The gel-filtration column was calibrated using a solution of low-molecular-weight protein standards (GE Healthcare Life Sciences, LMW standards kit). The chromatograms (not shown) indicate that the porphyrin binding fractions correspond exclusively to monomeric cytochrome *c* species and that the samples are free of low-molecular-weight peptide fragments.

Solutions of the acid-induced molten-globule state of ZnCytc were prepared according to the methods developed by Goto and co-workers[132] and described by Kostić and co-workers.[133] For use in the femtosecond pump–probe experiments, solutions of ZnCytc in the native or molten-globule states were prepared by diluting the stock protein solution with pH 7.0 50-mM sodium phosphate buffer solution to obtain an absorbance of 0.8 for a path length of 1.0 mm at the center of the laser spectrum at 420 nm for the native-state samples or at 418 nm for the molten-globule-state samples.

The samples were held in the femtosecond pump–probe spectrometer at room temperature (23 °C) in a fused-silica flow cuvette (0.5-mm path length). A peristaltic

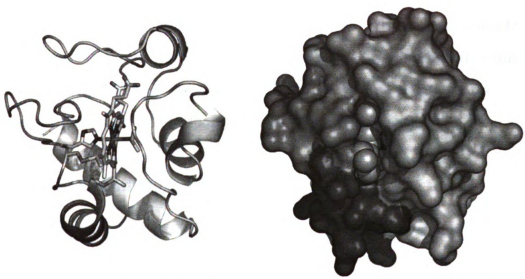

Figure 5.1. Ribbon (left) and surface (right) renderings of the X-ray crystal structure of horse-heart ferricytochrome *c* (1hrc.pdb). The porphyrin and the axial ligands to the Fe^{III} ion, M80 and H18, are shown as stick representations in the ribbon picture, and space-filling representations in the surface picture.

pump was used to circulate a 10-mL reservoir of sample solution through the cuvette at 2.70 mL/min. The sample's absorption spectrum was monitored during the experiment for changes arising from photochemistry or permanent photobleaching. The sample reservoir was exchanged with fresh solution several times during each run.

5.3.2 Continuous-Wave Absorption and Fluorescence spectroscopy

Absorption spectra were obtained at 23 °C with a Hitachi U-2000 spectrophotometer (2-nm band pass). Fluorescence spectra were acquired at 23 °C with a Hitachi F-4500 spectrofluorimeter (5-nm band pass for the excitation and emission monochromators). As presented as a function of wavenumber, the fluorescence intensities are multiplied by the square of the wavelength in order to compensate for the fixed (in wavelength units) spectral bandpass of the emission spectrometer.[89]

5.3.3 Femtosecond Spectroscopy

Femtosecond pump–probe transients with impulsive excitation were recorded using the dynamic-absorption technique in which the probe beam is dispersed in a grating monochromator after passing through the sample.[26,32,35-37] The present experiments were conducted with 50-fs pulses with intensity spectra centered at 420 nm for the native state and 418 nm for the molten-globule state (both 4 nm FWHM, as measured with an Ocean Optics USB-2000 spectrometer/CCD detector with a 0.5-nm bandpass) and a fairly narrow bandpass (1 nm) of the transmitted probe beam. This approach is similar to that used by Champion and co-workers in their studies of low-frequency vibrational coherence of heme proteins.[53,55,62]

The pump–probe spectrometer used in this work consists of a frequency doubled, self-mode-locked Ti:sapphire oscillator (Coherent Mira-F oscillator and Verdi V5 (5 W) Nd:YVO_4 pump laser, Coherent/Inrad 5-050 second-harmonic generator), a

SF10 Brewster prism-pair pulse compressor, and a rapid-scanning, modified Mach-Zehnder interferometer with confocal sample and autocorrelation-crystal positions. The planes of polarization of the pump and probe beams were set to be 45° apart using calcite polarizers and $\lambda/2$-retarding wave plates. After passing through the sample, the probe beam was analyzed by another calcite polarizer oriented 90° relative to the pump-beam's plane of polarization, and then it was passed through a monochromator (Acton Research SP-150) and was detected by an amplified photodiode (Thorlabs PDA5). The pump-probe signal was obtained from the photodiode signal using a lock-in amplifier (Femto LIA-MV-200-H); the pump beam was modulated at 100 kHz by a $\lambda/2$-retarding photoelastic modulator (Hinds Instrumentation) and a calcite polarizer. The instrumentation and methodology is identical to that described in Chapter 3.

5.4 Results

Figure 5.2 shows continuous-wave absorption and fluorescence spectra from the native state of ZnCytc at 23 °C. The spectra are plotted as relative dipole strengths[89,91,92] as a function of wavenumber ν, $A(\nu)/\nu$ and $F(\nu)/\nu^3$ respectively. The absorption spectrum features two bands, the Soret (or *B*) band and the *Q* band, in the blue and red parts of the spectrum, respectively. The fluorescence spectrum extends to the red from the 0-0 peak of the *Q* band. Also shown in Figure 5.2 is the absorption spectrum from the molten-globule state of ZnCytc. The absorption spectrum of the molten-globule sample is blue shifted relative to that of the native state sample.

The dynamic-absorption transients obtained for the native and molten-globule states are shown in Figures 5.3 and 5.4, respectively. Each transient exhibits an intense biphasic spike near the zero of time that goes off the plotted scale.[93-95] The

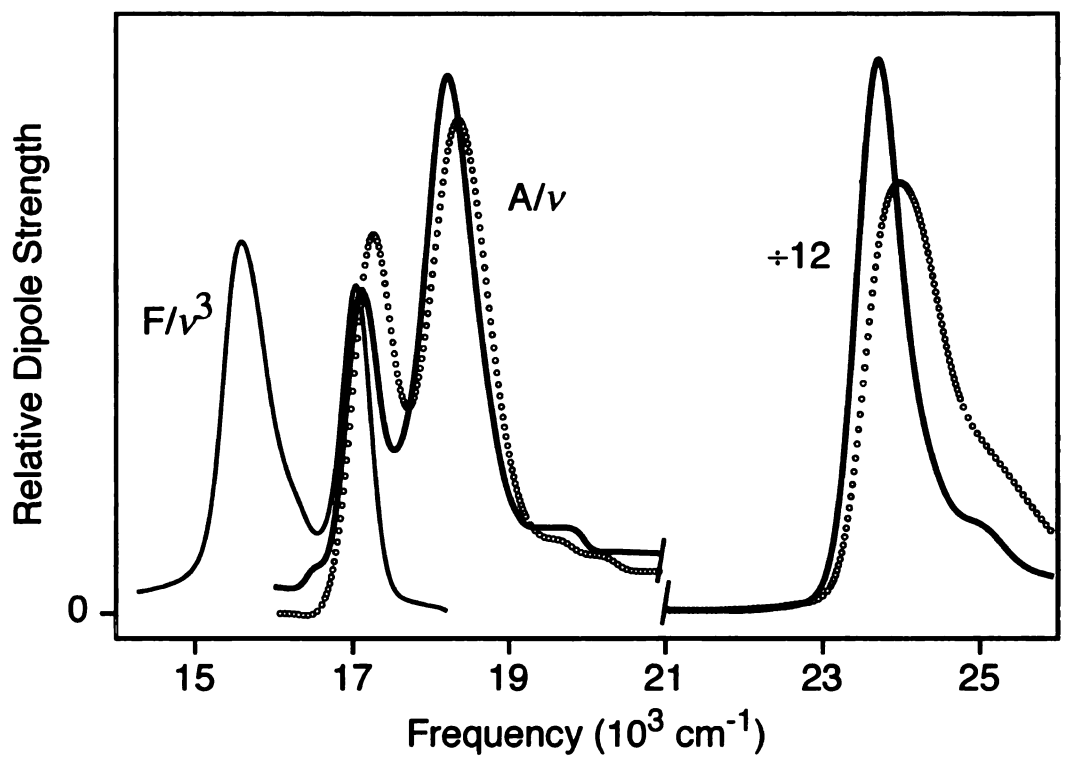

Figure 5.2. Soret ($\nu > 23000$ cm^{-1}) and Q-band regions of the continuous-wave absorption spectrum of ZnCytc in the native (solid curves) and molten-globule (circles) states. The fluorescence spectrum of the native state of ZnCytc at room temperature (23 °C) is shown overlapping and extending to the red of the absorption spectrum. The spectra are normalized to unit area with respect to the fluorescence spectrum and Q band.

native-state transient (see Figure 5.3) then exhibits a very rapidly damped oscillation over the early-time portion of the signal. The signal drops almost to the baseline and is then followed by a positive-going recurrence at the 170-fs delay point. The oscillation appears to be largely damped within the next 600 fs. The transient from the molten-globule state (see Figure 5.4) does not exhibit this oscillation. The signal exhibits a smooth transition from the positive side of the spike to a positive offset at the ~150 fs point. Both transients then exhibit a pattern of slowly damped cosinusoidal oscillations superimposed on an exponential decay that extends to the ~4 ps delay point. The most intense oscillations have periods longer than 1 ps.

Following truncation of the < 100-fs portion,[95] the transients were fit in the time domain to the sum of an exponential decay and multiple oscillatory components of the form

$$I_i(t) = A_i \, e^{-t^2\sigma_i^2/2} \cos(\omega_{0i}t - \phi_i) \Big/ \sqrt{2\pi} \tag{5.1}$$

with each component i having a center frequency ω_{0i} and phase ϕ_i. These waveforms correspond to Gaussian lineshapes in the frequency domain,

$$I_i(\omega) = A_i \, e^{-(\omega-\omega_{0i})^2/(2\sigma_i^2)} \Big/ (\sigma_i\sqrt{2\pi}) \tag{5.2}$$

where the line width is controlled by the standard deviation, $\sigma_i = \Delta\omega_i / 2\sqrt{2\ln 2}$, with $\Delta\omega_i$ standing for the full width at half maximum. Equations 5.1 and 5.2 are normalized so that the amplitude A_i corresponds to the area of the lineshape in the frequency domain and to the intensity of the signal in the time domain. Except as noted in the following, the modeling procedure was as described in detail in previous work on the ground-state vibrational coherence from ZnTMPyP.[88] The models are shown superimposed on the data points of the transient in Figures 5.3 and 5.4. The two strongest slowly damped components observed below 100 cm^{-1} in a Hanning-windowed Fourier-transform spectrum (not shown) were included in the model. The Fourier-transform spectra from both samples exhibit higher-frequency peaks near

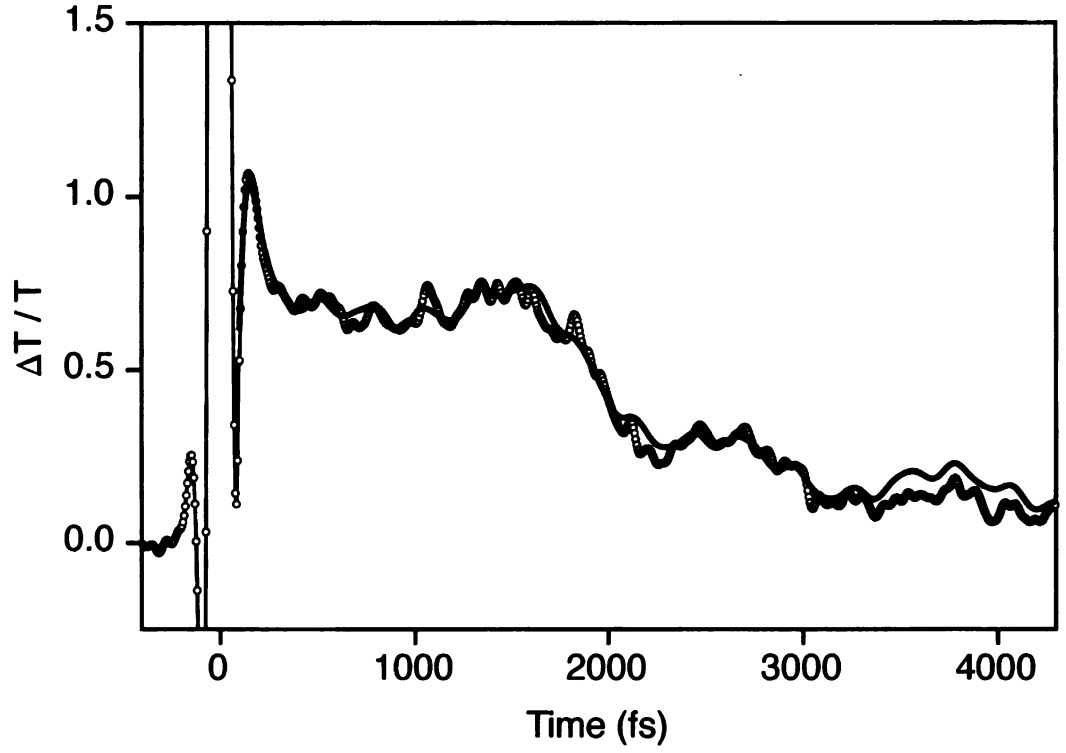

Figure 5.3. Soret-band (420-nm) pump-probe transient from the native state of Zn-Cytc. The signal points (circles) are superimposed on a model consisting of the sum of an exponential decay and two oscillatory components. The exponential has a time constant of 1.8 ps; the plotted signal is normalized to the exponential's intensity. The parameters for the oscillatory components are listed in Table 5.1.

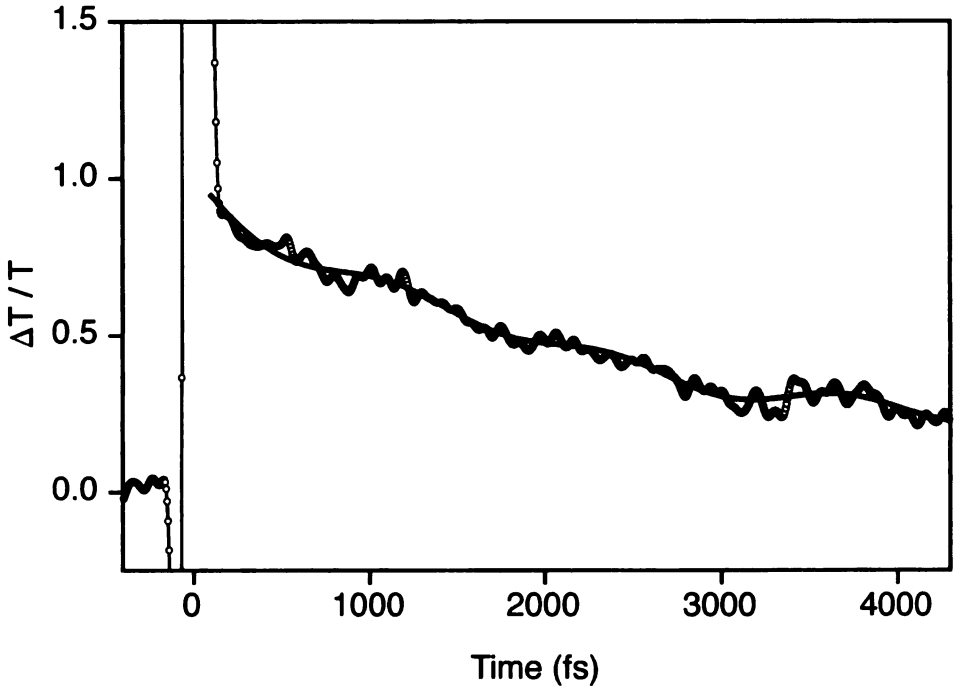

Figure 5.4. Soret-band (420-nm) pump–probe transient from the molten-globule state of ZnCytc. The signal points (circles) are superimposed on a model consisting of the sum of an exponential decay and two oscillatory components. The exponential has a time constant of 1.8 ps; the plotted signal is normalized to the exponential's intensity. The parameters for the oscillatory components are listed in Table 5.2.

120 cm^{-1} and 220 cm^{-1}, but these features are comparable in intensity to the noise level. Similar features were observed by Champion and co-workers in ferricytochrome *c* and myoglobin.[54,57] The relative weakness of the higher-frequency modulation components is consistent with the tuning of the pump spectrum to the center of the absorption spectrum.[55,56]

Frequency-domain representations of the models obtained for the oscillatory part of the native and molten-globule signals are shown in Figure 5.5a and b, respectively. The parameters for these models are listed in Tables 5.1 and 5.2. The model for the native-state signal includes two slowly damped features, at 10 and 31 cm^{-1}, and a single rapidly damped feature centered at 79 cm^{-1}. The slowly damped components probably arise from metal-doming modes in sites having axial-ligand interactions to the Zn^{II} ion with the M80 and H18 side chains, respectively. Comparable features appear at 11 and 26 cm^{-1} in the molten-globule spectrum, but they are less intense and narrower in lineshape than those observed in the native state. The broad feature ($\Delta\omega$=106 cm^{-1}) at 79 cm^{-1} that appears only in the native-state model is assigned to van der Waals modes with the surrounding protein. It is several times more intense than the slowly damped, metal-doming features.

5.5 Discussion

The main finding of this chapter is that the vibrational coherence observed in the molten-globule state of ZnCytc lacks the strong, rapidly damped modulation component from van der Waals interactions with nearby protein residues that is observed in the native state. This observation suggests that the expanded hydrophobic core and the randomization of the local structural order that accompanies the formation of the molten-globule state destroys the coupling of the Zn^{II} porphyrin's $\pi \rightarrow \pi^*$ transition to the surrounding protein. In the following, we account for this conclu-

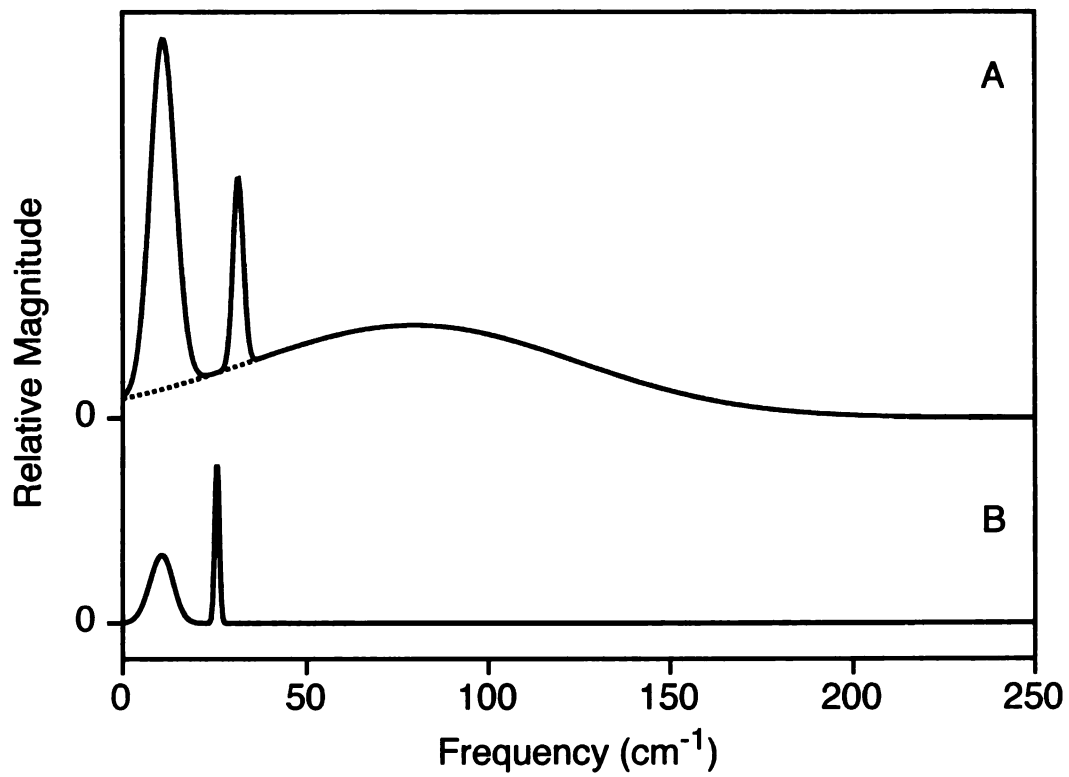

Figure 5.5. Frequency-domain representations of oscillatory components of the fitted models of the vibrational coherence obtained from the (a) native state and (b) molten globule state of ZnCytc. The model parameters are listed in Tables 5.1 and 5.2.

Table 5.1. Gaussian lineshape parameters for the modulation components obtained from the pump-probe transient of ZnCytc in the native state (see Figure 5.3).

Component	ω_0 (cm^{-1})	$\Delta\omega$ (cm^{-1})	Amplitude[a]
1	10	8.02	0.809
2	31	3.25	0.177
3	79	106	2.84

[a] Normalized relative to the amplitude of the exponential decay of the transient (see Figure 5.3).

Table 5.2. Gaussian lineshape parameters for the modulation components obtained from the pump-probe transient of ZnCytc in the molten-globule state (see Figure 5.4).

Component	ω_0 (cm^{-1})	$\Delta\omega$ (cm^{-1})	Amplitude[a]
1	11	7.76	0.157
2	26	0.575	7.08×10^{-2}

[a] Normalized relative to the amplitude of the exponential decay of the transient (see Figure 5.4).

sion first by considering the spectroscopic origin of the vibrational coherence that we observe in both samples and then by considering the nature of the change in structure that modulates the resonance Raman activity and possibly also the lineshape of the van der Waals modes. We conclude with a brief discussion of the significance of these findings with respect to the function of the van der Waals interactions in purple-bacterial reaction centers and how the frequency of these interactions can be tuned by changing the structure of the protein around the chromophore.

The pump-probe signals obtained with Soret-band excitation of ZnCytc in the native and molten-globule states are modulated primarily by ground-state vibrational coherence. Both signals exhibit a net ground-state depletion character over the 4-ps experimental window, but there is a ~2-ps exponential decay that returns the signal to the baseline level at the end of the recording (see Figures 5.3 and 5.4). This behavior is just like that observed previously with ZnTMPyP.[88] The exponential decay, then, most likely arises from vibrational cooling in the S_1-state manifold following an ultrafast (t<100 fs) internal conversion of the S_2-state population prepared by the pump pulse.[103] Given that the impulsive character of the excitation is not retained following the $S_2 \rightarrow S_1$ nonradiative process, the modulations observed in the pump-probe signals have to be assigned to coherent wavepacket motions on the ground-state potential energy surface. These motions are launched along the coordinates of the normal modes that are displaced by the $\pi \rightarrow \pi^*$ transition, assuming the Albrecht A-term mechanism for resonance Raman activity;[120,121] the amplitudes of the associated modulation components that appear in the pump-probe signal are analogous to relative resonance Raman activities.[24-26,30,32,33,121] The intramolecular or skeletal modes of the Zn^{II} porphyrin obtain resonance Raman activity owing to the changes in the electronic structure that accompany the $\pi \rightarrow \pi^*$ transition. The van der Waals modes between the Zn^{II} porphyrin and groups that pack around its π-electron density obtain resonance Raman activity because they are reoriented or

displaced by the changes in shape or extent of the π-electron density that accompany the $\pi \rightarrow \pi^*$ transition.

The slowly damped modulation components ($\gamma > 1.5$ ps, $\Delta\omega < 10$ cm^{-1}) correspond to intramolecular modes, from the porphyrin macrocycle and the axial ligands to the Zn^{II} ion.[65,88] The two modulation features that were modeled in the native and molten-globule signals are very likely to correspond to metal-doming motions. In their studies of myoglobin and ferricytochrome *c*, Champion and co-workers observed low-frequency modes near 40 cm^{-1} that were assigned to the metal-doming mode.[57] In Zn^{II} porphyrins, however, the central metal ion is not as strongly coordinated by the porphyrin, so a decrease in the metal-doming frequency might be expected. Previous studies have shown that the Zn^{II} ion in porphyrin complexes in solution prefers a five-coordinate crystal field, so only a single axial ligand is likely to be bound in ZnCytc.[134-137] Six-coordinate Zn^{II} porphyrins are observed in crystals, but the porphyrin is distorted by crystal-packing forces.[138-140] In ZnCytc, the resonance Raman spectra obtained by Kostić and co-workers suggest that an orthodox six-coordinate configuration for the Zn^{II} ion is not present.[131] The picosecond time-resolved fluorescence results obtained previously in this laboratory, however, show that there are two phases of axial-ligand photodissociation with *Q*-band excitation.[141] We suggested in that work that the folded native structure might impose a six-coordinate structure on the Zn^{II} ion owing to packing forces from the folded protein in analogy to those in crystals.

The present work shows that two slowly damped modulation features, at 10 and 30 cm^{-1}, are present in the signals from the native and molten-globule states of ZnCytc. We suggest that both of these features arise from the metal-doming mode of the Zn^{II} porphyrin in two different five-coordinate configurations. The lower frequency feature, at 10 and 11 cm^{-1} in the native and molten-globule states, respectively, probably arises from the sub-ensemble of molecules in which the Zn^{II} ion is

domed so that an axial-ligand interaction can be made to the side chain of the methionine residue M80. The higher-frequency feature, at 31 and 26 cm^{-1} in the native and molten-globule states, would then arise from the sub-ensemble with the Zn^{II} ion domed so that the axial-ligand interaction is made to the side chain of the histidine residue H18. The two structures would be distinct because of the significant activation required for the Zn^{II} ion to move across the plane of the porphyrin. The lower frequency and broader width of the 10-cm^{-1} feature probably arises from the weaker ligand-metal bond formed between the Zn^{II} ion and the thioether side chain of the methionine residue. The observation that the both the 10-cm^{-1} and 30-cm^{-1} features are significantly weaker in modulation amplitude in the molten-globule state than observed in the native state (see Figure 5.5 and Tables 5.1 and 5.2) suggests that a smaller fraction of the overall ensemble of molecules coordinates either of the two amino acids to the Zn^{II} ion at a given instant in time.

Several aspects of the change in protein structure that accompanies the formation of the molten-globule state account for the disappearance of the rapidly damped modulation feature that apparently arises from van der Waals interactions in the native state. The molten-globule state of cytochrome *c* has been extensively studied.[132,133,142-148] It is characterized by the loss of the ordered interactions between neighboring groups that characterizes the native structure, but most of the secondary structural content of the native state is retained.[143] The protein structure adopts an expanded configuration that rapidly samples a range of internal organizations. X-ray light-scattering experiments show that the Stokes radius of the cavity that surrounds the porphyrin in the molten-globule state is between four and fifteen percent larger than that of the native state.[142,143] The blue-shifted absorption spectrum of the molten-globule state (see Figure 5.2) probably results from the lowered average polarizability of the protein-derived surroundings that results from the expanded cavity. Such an expansion would be expected to attenuate strongly the res-

onance Raman activities of the van der Waals modes because on average the distance between the adjacent groups and the π-electron density of the Zn^{II} porphyrin would be increased and the associated sensing of the ground-to-excited-state changes in the π-electron density would be concomitantly decreased. The rapid sampling of different internal configurations would be expected to broaden the range of configurations that contribute to the inhomogeneously broadened ensemble, with a broadened lineshape the likely result. In the time domain, in a pump-probe experiment, the especially rapid damping of such a component would mitigate further against its detection.

The relatively low mean frequency of the van der Waals modes observed in the native state of ZnCytc is consistent with the structure of the FeCytc because there are no nearby polar residues that are close enough to the π-electron density of the porphyrin to obtain strong coupling to the $\pi \rightarrow \pi^*$ transition and high mode frequencies. In the following, we analyze the range of possible interactions in terms of the X-ray crystal structure and in terms of the known behavior of the van der Waals potential.

The frequency of the van der Waals modes can be understood in terms of the potential that was discussed in the previous chapters. When there are no nearby charges present, the potential can be expressed as the sum of a repulsive, exchange term scaled by r^{-12} and a series of attractive terms scaled by r^{-6}:

$$V_0(r) = a/r^{12} - \left(b\alpha_1\alpha_2 + \frac{c|\boldsymbol{\mu}_1|^2|\boldsymbol{\mu}_2|^2}{(4\pi\varepsilon_0)^2} + \frac{\alpha_2|\boldsymbol{\mu}_1|^2 + \alpha_1|\boldsymbol{\mu}_2|^2}{4\pi\varepsilon_0} \right) \Big/ D^2 r^6 \qquad (5.3)$$

As shown previously,[63] a Taylor series expansion of Equation 5.3 around the equilibrium geometry gives an expression for the natural frequency of the van der Waals mode,

$$\nu = \frac{3}{(2a)^{2/3}} \left(b\alpha_1\alpha_2 + \frac{c|\boldsymbol{\mu}_1|^2|\boldsymbol{\mu}_2|^2}{(4\pi\varepsilon_0)^2} + \frac{\alpha_2|\boldsymbol{\mu}_1|^2 + \alpha_1|\boldsymbol{\mu}_2|^2}{4\pi\varepsilon_0} \right)^{7/6} \Big/ 2\pi D^{7/3}\mu^{1/2} \qquad (5.4)$$

In both equations, the constant a scales the Pauli (exchange) interaction, b scales the London-dispersion interaction, $c = 2/3k_BT$ scales the dipole–dipole interactions, and the $\alpha_i\mu_j^2$ terms correspond to dipole-induced-dipole interactions; μ_i and α_i correspond to the dipole moment and polarizability of the choromphore solute and solvent (subscripts 1 and 2, respectively). Lastly, r is the distance between the two molecules, μ is the reduced mass of the oscillator, D is the dielectric constant of the medium, and ε_0 is the permittivity of free space.[113-116] As expressed above, the dipole-dependent terms apply to the high-temperature limit, where k_BT is much greater than the well depth, so the interaction is averaged over all orientations.[115] If the potential well depth is greater than k_BT, the assumption that it is appropriate to average the interaction energy over all orientations may not be valid.

When the solute or solvent has a charge $Q_{1,2}$, the potential gains attractive terms corresponding to the ion–dipole and ion-induced-dipole interactions:

$$V_Q(r) = V_0 - \left(\frac{cQ_1|\mu_2|^2 + cQ_2|\mu_1|^2}{(4\pi\epsilon_0)^2} + \frac{\alpha_2 Q_1^2 + \alpha_1 Q_2^2}{4\pi\varepsilon_0} \right) \Big/ 2D^2 r^4 \qquad (5.5)$$

This form of the potential is similar to that introduced in Chapters 3 and 4, except that we now explicitly account for any charges that may be located either on the solute or solvent. The ion–dipole term depends linearly on the charge and the square of the dipole moment μ_i, and the ion-induced-dipole term depends on the polarizability α_i and exhibits quadratic charge dependence. Additionally, the charge-containing terms have an r^{-4} dependence on the solute–solvent distance. Thus, the charge-dependent terms cause the potential to extend to much greater distances than does the neutral potential. Equation 5.5 also predicts that the depth of the potential well will increase significantly over that predicted from the neutral potential (Equation 5.3), so the assumption of orientational averaging made for the uncharged case is no longer valid, and the result would be an even more stable structure for the van der Waals complex. Overall, the largest contributions to the van der Waals potential

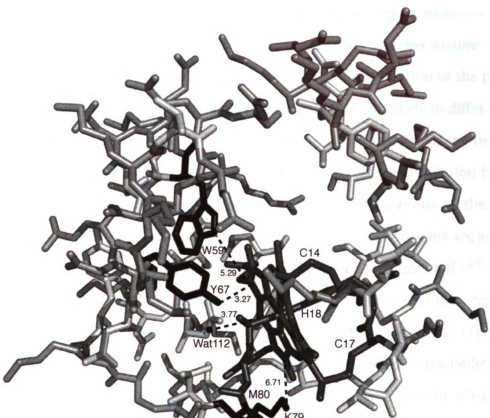

Figure 5.6. Detail of the X-ray crystal structure of ferricytochrome *c* (1hrc.pdb) examining possible interactions of the protein with the π-electron density of the porphyrin. Polar and charged residues are rendered as light and dark gray stick figures, respectively. Nonpolar residues are omitted from the figure so that the resulting non-polar cavity is made clear. Nearest-neighbor distances are shown between the porphyrin and several residues: the hydroxyl group on Y67 (3.27 Å), the nitrogen atom on W59 (5.29 Å), and the nitrogen on K79 (6.71 Å). The Y67, W59 and K79 residues are shown in black. The interior water molecule (Wat-112, black sphere) is 3.77 Å from the porphyrin.

are those arising from the London-dispersion interactions and those involving nearby polar or charged residues.

An assessment of the protein-derived structures that are near enough to the porphyrin in ZnCytc to form a coupled van der Waals mode can be made on the basis of the X-ray crystal structure of FeCytc because the two proteins assume the same or similar structures in solution. As noted above, the conformation of the porphyrin and the configuration of the axial ligands to the metal ion are likely to differ in FeCytc and ZnCytc because of the specifics of the coordination chemistry of the two metals. The structures of horse-heart ZnCytc and ferrocytochrome *c* in solution have been compared using 2D-NMR spectroscopy.[149,150] The configurations of the polypeptide backbone and amino-acid side chains of the Fe^{II} and Zn^{II} proteins are apparently quite comparable judging from the proton chemical shifts. Anni et al.[149] conclude that the side chains of H18 and M80 are suitably arranged so that they can interact with the Zn^{II} ion as axial ligands just as indicated by the FeCytc X-ray crystal structure. The X-ray crystal structure of ZnCytc from horse heart is not available; however, the structures of Fe:ZnCytc cocrystals from tuna have been solved by Winkler, Gray, and coworkers.[151] The Fe^{III}-containing sites in the asymmetric unit exhibit structures that are qualitatively comparable to those of the Zn^{II}-containing sites. Thus, although some differences from the crystal structure should be expected in solution, it is reasonable to use the crystal structure of FeCytc from horse heart as a guide for that of ZnCytc in the following analysis.

Figure 5.6 depicts the polar and charged residues in FeCytc that contribute to the environment of the porphyrin. None of these groups are close enough to the π-electron density of the porphyrin to make a coupled van der Waals mode. The distances shown in Figure 5.6 are those for the shortest nearest-neighbor vectors between the porphyrin and a labeled polar or charged residue. The π-electrons are delocalized over the entire porphyrin ring, however, so the magnitude of the van der

Waals interactions would be smaller than indicated by the distance measurements. The nearest charged residue is a lysine residue (K79), but it lies greater than 6 Å at closest approach from the nearest atom in the porphyrin macrocycle. The lysine residue (K13) that crosses in front of the heme in Figure 5.6 is approximately 10 Å from the porphyrin. The nearest polar groups in the surrounding protein medium that are not directly coordinated to the metal ion are the tyrosine and tryptophan residues, Y67 and W59. As shown in Figure 5.6, these residues are at least 3 and 5 Å from the porphyrin macrocycle, respectively, so their interactions with the π-electron density are weak. Polar interactions with nearby bulk water molecules can be neglected because the porphyrin is exposed along the equatorial plane (see Figure 5.1). The conserved interior water molecule Wat-112 (Wat-166 in yeast *iso*-1-cytochrome c[152]) is hydrogen bonded to the nearby N52, Y67 and T78 residues.[153] It is ~3.8 Å from the porphyrin (see Figure 5.6), so its contribution to the signal will also be negligible.

The main contributions to the coupled van der Waals interactions between the protein and the porphyrin's π-electron density in ZnCytc arise from London-dispersion interactions with non-polar residues. These residues fill the majority of the cavity adjacent to the porphyrin in the native state (see Figure 5.6). The lineshape resulting from these interactions will be very broad because of the wide range of distances and orientations with respect to the porphyrin. The modulation components from polar residues, if they were present, would exhibit higher frequencies and narrower lineshapes. The trend of the mode frequency as a function of the solvent dipole moment obtained in the previous work on ZnTMPyP suggests a frequency in the nonpolar limit near 70 cm^{-1}.[88] The mean frequency (79 cm^{-1}) and broad lineshape (or rapid damping) of the van der Waals interaction observed in the native state of ZnCytc is consistent with these expectations.

These observations allow a suggestion about the nature of the vibrational coherence in the purple-bacterial photosynthetic reaction center[43-46,48-51,76] that arises from van der Waals modes. The overall spectrum should contain an underlying broad lineshape arising from the interactions of non-polar residues in the surroundings of the primary electron donor P. Narrower lineshapes, from interactions of dipolar or charged residues, will be superimposed on the broad background. This description is consistent with the observations made by Vos, Martin and co-workers in their studies of the effects of point mutations on the vibrational coherence in the *Rhodobacter sphaeroides* reaction centers.[50] The mutations swapped nonpolar for polar, polar for nonpolar, or polar for charged residues. The spectrum from each mutant was unique in having one or more relatively narrow lines at different frequencies but these varying features were superimposed on a broad background lineshape that was independent of the mutation. Thus, we suggest that the sharper components arise from dipole-dipole interactions involving an amino acid near the porphyrin, and the invariant broad background lineshape arises from the London-dispersion interactions with adjacent groups.

5.5.1 Conclusions

The principal result of this chapter is that rapidly damped contributions to the vibrational coherence in ZnCytc arise from van der Waals interactions between the porphyrin and the surrounding protein medium. The expansion of the core and randomization of the surrounding structure effectively quenches these interactions in the molten-globule state. The van der Waals potential that accounts for the modulation components in the vibrational coherence is dominated by London-dispersion interactions; charged and polar residues are too distant in the native structure from the porphyrin to contribute significantly to the signal. The specific interactions that gain resonance Raman intensity via coupling to the $\pi \rightarrow \pi^*$ transition of the por-

phyrin are those that are capable of directly attacking the π-electron density. In the photosynthetic reaction center, the low-frequency vibrational modes that are coupled to the primary and secondary charge-separation reactions probably arise from van der Waals interactions between the redox-active chromophores and the surrounding protein medium. The local structure around a chromophore can tune the mean frequency of the interaction through the addition of polar or charged groups. These findings provide a possible mechanism that accounts for the ability of the surrounding protein structure to optimize the efficiency of the energy-storing electron-transfer reactions in photosynthesis.

BIBLIOGRAPHY

(1) Bixon, M.; Jortner, J. Activationless and pseudoactivationless primary electron transfer in photosynthetic bacterial reaction centers. *Chem. Phys. Lett.* **1989**, *159*, 17-20.

(2) Marcus, R. A. On the theory of oxidation-reduction reactions involving electron transfer. I. *J. Chem. Phys.* **1956**, *24*, 966-989.

(3) Jortner, J. Temperature dependent activation energy for electron transfer between biological molecules. *J. Chem. Phys.* **1976**, *64*, 4860-4867.

(4) Marcus, R. A.; Sutin, N. Electron transfers in chemistry and biology. *Biochim. Biophys. Acta* **1985**, *811*, 265-322.

(5) Wasielewski, M. R. Photoinduced electron transfer in supramolecular systems for artificial photosynthesis. *Chem. Rev.* **1992**, *92*, 436-461.

(6) Wasielewski, M. R.; Wiederrecht, G. P.; Svec, W. A.; Niemczyk, M. P. Chlorin-based supramolecular assemblies for artificial photosynthesis. *Solar Energy Mat. Solar Cells* **1995**, *38*, 127-134.

(7) Gust, D.; Moore, T. A.; Makings, L. R.; Liddell, P. A.; Nemeth, G. A.; Moore, A. L. Photodriven electron transfer in triad molecules: a two-step charge recombination reaction. *J. Am. Chem. Soc.* **1986**, *108*, 8028-8031.

(8) Gust, D.; Moore, T. A. Mimicking photosynthesis. *Science* **1989**, *244*, 35-41.

(9) Gust, D.; Moore, T. A.; Moore, A. L.; Lee, S. -J.; Bittersmann, E.; Luttrull, D. K.; Rehms, A. A.; DeGaraziano, J. M.; Ma, X. C.; Gao, F.; Belford, R. E.; Trier, T. T. Efficient multistep photoinitiated electron transfer in a molecular pentad. *Science* **1990**, *248*, 199-201.

(10) Gust, D.; Moore, T. A.; Moore, A. L. Mimicking photosynthetic solar energy transduction. *Acc. Chem. Res.* **2001**, *34*, 40-48.

(11) Prathapan, S.; Johnson, T. E.; Lindsey, J. S. Building-block synthesis of porphyrin light-harvesting arrays. *J. Am. Chem. Soc.* **1993**, *115*, 7519-7520.

(12) Hsiao, J. -S.; Krueger, B. P.; Wagner, R. W.; Johnson, T. E.; Delayen, J. K.; Mauzerall, D. C.; Fleming, G. R.; Lindsey, J. S.; Bocian, D. F.; Donohoe, R. J. Soluble Synthetic Multiporphyrin Arrays. 2. Photodynamics of energy-transfer processes. *J. Am. Chem. Soc.* **1996**, *118*, 11181-11193.

(13) Stenberg-Yfrach, G.; Rigaud, J. -L.; Durantini, E. N.; Moore, A. L.; Gust, D.; Moore, T. A. Light-driven production of ATP catalysed by F0F1-ATP synthase in an artificial photosynthetic membrane. *Nature* **1998**, *392*, 479-482.

(14) McCusker, J. K. Fuel from photons. *Science* **2001**, *293*, 1599-1601.

(15) McCusker, J. K. Femtosecond absorption spectroscopy of transition metal charge-transfer complexes. *Acc. Chem. Res.* **2003**, *36*, 876-887.

(16) Redmore, N. P.; Rubtsov, I. V.; Therien, M. J. Synthesis, electronic structure, and electron transfer dynamics of (aryl)ethynyl-bridged donor-acceptor systems. *J. Am. Chem. Soc.* **2003**, *125*, 8769-8778.

(17) Splan, K. E.; Stern, C. L.; Hupp, J. T. Two coordinatively linked supramolecular assemblies constructed from highly electron deficient porphyrins. *Inorg. Chim. Acta* **2004**, *357*, 4005-4014.

(18) Kalyanasundaram, K.; Vlazhopoulos, N.; Krishnan, V.; Monnier, A.; Grätzel, M. Sensitization of TiO_2 in the visible light region using zinc porphyrins. *J. Phys. Chem* **1987**, *91*, 2342.

(19) Kay, A.; Grätzel, M. Artificial photosynthesis. 1. Photosensitization of TiO2 solar cells with chlorophyll derivatives and related natural porphyrins. *J. Phys. Chem.* **1993**, *97*, 6272-6277.

(20) Fleming, G. R.; Martin, J. -L.; Breton, J. Rates of primary electron transfer in photosynthetic reaction centers and their mechanistic implications. *Nature* **1988**, *333*, 190-192.

(21) Atkins, P.; Jones, L. *Chemical Principles: The Quest for Insight*; W. H. Freeman: New York, 2002.

(22) Bixon, M.; Jortner, J. Coupling of protein modes to electron transfer in bacterial photosynthesis. *J. Phys. Chem.* **1986**, *90*, 3795-3800.

(23) Jortner, J.; Bixon, M. Intramolecular vibrational excitations accompanying solvent-controlled electron transfer reactions. *J. Chem. Phys.* **1988**, *88*, 167-170.

(24) Pollard, W. T.; Fragnito, H. L.; Bigot, J. -Y.; Shank, C. V.; Mathies, R. A. Quantum-mechanical theory for 6 fs dynamic absorption spectroscopy and its application to nile blue. *Chem. Phys Lett.* **1990**, *168*, 239-245.

(25) Pollard, W. T.; Lee, S. -Y.; Mathies, R. A. Wave packet theory of dynamic absorption spectra in femtosecond pump-probe experiments. *J. Chem. Phys.* **1990**, *92*, 4012-4029.

(26) Pollard, W. T.; Mathies, R. A. Analysis of femtosecond dynamic absorption spectra of nonstationary states. *Annu. Rev. Phys. Chem.* **1992**, *43*, 497-523.

(27) Jonas, D. M.; Bradforth, S. E.; Passino, S. A.; Fleming, G. R. Femtosecond wavepacket spectroscopy: influence of temperature, wavelength, and pulse duration. *J. Phys. Chem.* **1995**, *99*, 2594-2608.

(28) Voth, G. A.; Hochstrasser, R. M. Transition state dynamics and relaxation processes in solutions: a frontier of physical chemistry. *J. Phys. Chem.* **1996**, *100*, 13034-13049.

(29) Carson, E. A.; Diffey, W. M.; Shelly, K. R.; Lampa-Pastirk, S.; Dillman, K. L.; Schleicher, J. M.; Beck, W. F. Dynamic-absorption spectral contours: vibrational phase-dependent resolution of low-frequency coherent wave-packet motion of IR144 on the ground and excited $\pi \rightarrow \pi^*$ surfaces. *J. Phys. Chem. A* **2004**, *108*, 1489-1500. DOI: 10.1021/jp035176c.

(30) Walsh, A. M.; Loring, R. F. Theory of resonant and nonresonant impulsive stimulated Raman scattering. *Chem. Phys. Lett.* **1989**, *160*, 299-304.

(31) Pollard, W. T.; Brito Cruz, C. H.; Shank, C. V.; Mathies, R. A. Direct observation of the excited-state *cis-trans* photoisomerization of bacteriorhodopsin: multilevel line shape theory for femtosecond dynamic hole burning and its application. *J. Chem. Phys.* **1989**, *90*, 199-208.

(32) Dexheimer, S. L.; Wang, Q.; Peteanu, L. A.; Pollard, W. T.; Mathies, R. A.; Shank, C. V. Femtosecond impulsive excitation of nonstationary vibrational states in bacteriorhodopsin. *Chem. Phys. Lett.* **1992**, *188*, 61-66.

(33) Pollard, W. T.; Dexheimer, S. L.; Wang, Q.; Peteanu, L. A.; Shank, C. V.; Mathies, R. A. Theory of dynamic absorption spectroscopy of nonstationary states. 4. Application to 12-fs resonant impulsive Raman spectroscopy of bacteriorhodopsin. *J. Phys. Chem.* **1992**, *96*, 6147-6158.

(34) Myers, A. B.; Mathies, R. A. Resonance Raman intensities: a probe of excited-state structure and dynamics. In *Biological Applications of Raman Spectroscopy*; Spiro, T. G., Ed.; Wiley-Interscience: New York, 1987; Vol. 2, Resonance Raman Spectra of Polyenes and Aromatics, pp 1-58.

(35) Fragnito, H. L.; Bigot, J. -Y.; Becker, P. C.; Shank, C. V. Evolution of the vibronic absorption spectrum in a molecule following impulsive excitation with a 6-fs optical pulse. *Chem. Phys. Lett.* **1989**, *160*, 101-104.

(36) Schoenlein, R. W.; Peteanu, L. A.; Mathies, R. A.; Shank, C. V. The first step in vision: femtosecond isomerization of rhodopsin. *Science* **1991**, *254*, 412-415.

(37) Wang, Q.; Schoenlein, R. W.; Peteanu, L. A.; Mathies, R. A.; Shank, C. V. Vibrationally coherent photochemistry in the femtosecond primary event of vision. *Science* **1994**, *266*, 422-424.

(38) Mathies, R. A.; Brito Cruz, C. H.; Pollard, W. T.; Shank, C. V. Direct observation of the femtosecond excited-state *cis-trans* isomerization in bacteriorhodopsin. *Science* **1988**, *240*, 777-779.

(39) Schoenlein, R. W.; Peteanu, L. A.; Wang, Q.; Mathies, R. A.; Shank, C. V. Femtosecond dynamics of *cis-trans* isomerization in a visual pigment analog: isorhodopsin. *J. Phys. Chem.* **1993**, *97*, 12087-12092.

(40) Peteanu, L. A.; Schoenlein, R. W.; Wang, Q.; Mathies, R. A.; Shank, C. V. The first step in vision occurs in femtoseconds: complete blue and red spectral studies. *Proc. Natl. Acad. Sci. U.S.A.* **1993**, *90*, 11762-11766.

(41) Wang, Q.; Kochendoerfer, G. G.; Schoenlein, R. W.; Verdegem, P. J. E.; Lugtenburg, J.; Mathies, R. A.; Shank, C. V. Femtosecond spectroscopy of a 13-demethylrhodopsin visual pigment analogue: the role of nonbonded interactions in the isomerization process. *J. Phys. Chem.* **1996**, *100*, 17388-17394.

(42) Bardeen, C. J.; Yakovlev, V. V.; Wilson, K. R. Quantum control of population transfer in green fluorescent protein by using chirped femtosecond pulses. *J. Am. Chem. Soc.* **1998**, *120*, 13023.

(43) Vos, M. H.; Lambry, J. -C.; Robles, S. J.; Youvan, D. C.; Breton, J.; Martin, J. -L. Direct observation of vibrational coherence in bacterial reaction centers using femtosecond absorption spectroscopy. *Proc. Natl. Acad. Sci. U.S.A.* **1991**, *88*, 8885-8889.

(44) Vos, M. H.; Lambry, J. -C.; Robles, S. J.; Youvan, D. C.; Breton, J.; Martin, J. -L. Femtosecond spectral evolution of the excited state of bacterial reaction centers at 10 K. *Proc. Natl. Acad. Sci. U.S.A.* **1992**, *89*, 613-617.

(45) Vos, M. H.; Rappaport, F.; Lambry, J. -C.; Breton, J.; Martin, J. -L. Visualization of the coherent nuclear motion in a membrane protein by femtosecond spectroscopy. *Nature* **1993**, *363*, 320-325.

(46) Vos, M. H.; Jones, M. R.; Hunter, C. N.; Breton, J.; Lambry, J. -C.; Martin, J. -L. Coherent dynamics during the primary electron-transfer reaction in membrane-bound reaction centers of *Rhodobacter sphaeroides*. *Biochemistry* **1994**, *33*, 6750-6757.

(47) Vos, M. H.; Jones, M. R.; McGlynn, P.; Hunter, C. N.; Breton, J.; Martin, J. -L. Influence of the membrane environment on vibrational motions in reaction

centers of *Rhodobacter sphaeroides*. *Biochim. Biophys. Acta* **1994**, *1186*, 117-122.

(48) Vos, M. H.; Jones, M. R.; Breton, J.; Lambry, J. -C.; Martin, J. -L. Vibrational dephasing of long- and short-lived primary donor states in mutant reaction centers of *Rhodobacter sphaeroides*. *Biochemistry* **1996**, *35*, 2687-2692.

(49) Vos, M. H.; Jones, M. R.; Martin, J. -L. Vibrational coherence in bacterial reaction centers: spectroscopic characterisation of motions active during primary electron transfer. *Chem. Phys.* **1998**, *233*, 179-190.

(50) Rischel, C.; Spiedel, D.; Ridge, J. P.; Jones, M. R.; Breton, J.; Lambry, J. -C.; Martin, J. -L.; Vos, M. H. Low frequency vibrational modes in proteins: changes induced by point-mutations in the protein-cofactor matrix of bacterial reaction centers. *Proc. Natl. Acad. Sci. U.S.A.* **1998**, *95*, 12306-12311.

(51) Vos, M. H.; Martin, J. -L. Femtosecond processes in proteins. *Biochim. Biophys. Acta* **1999**, *1411*, 1-20.

(52) Go, N.; Noguti, T.; Nishikawa, T. Dynamics of a small globular protein in terms of low-frequency vibrational modes. *Proc. Nat. Acad. Sci. USA* **1983**, *80*, 3696-3700.

(53) Zhu, L.; Li, P.; Huang, M.; Sage, J. T.; Champion, P. M. Real time observation of low frequency heme protein vibrations using femtosecond coherence spectroscopy. *Phys. Rev. Lett.* **1994**, *72*, 301-304.

(54) Rosca, F.; Kumar, A. T. N.; Ye, X.; Sjodin, T.; Demidov, A.; Champion, P. M. Investigations of coherent vibrational oscillations in myoglobin. *J. Phys. Chem. A* **2000**, *104*, 4280-4290.

(55) Rosca, F.; Ionascu, D.; Kumar, A. T. N.; Demidov, A. A.; Champion, P. M. Femtosecond coherence spectroscopy using spectrally selective differential photodetection. *Chem. Phys. Lett.* **2001**, *337*, 107-116.

(56) Rosca, F.; Kumar, A. T. N.; Ionascu, D.; Sjodin, T.; Demidov, A. A.; Champion, P. M. Wavelength selective modulation in femtosecond pump-probe spectroscopy and its application to heme proteins. *J. Chem. Phys.* **2001**, *114*, 10884-10898.

(57) Rosca, F.; Kumar, A. T. N.; Ionascu, D.; Ye, X.; Demidov, A. A.; Sjodin, T.; Wharton, D.; Barrick, D.; Sligar, S. G.; Yonetani, T.; Champion, P. M. Investigations of anharmonic low-frequency oscillations in heme proteins. *J. Phys. Chem. A* **2002**, *106*, 3540-3552.

(58) Barkhuijsen, H.; de Beer, R.; Bovée, W. M. M. J.; van Ormondt, D. Retrieval of frequencies, amplitudes, damping factors, and phases from time-domain signals using a linear least-squares procedure. *J. Magn. Reson.* **1985**, *61*, 465-481.

(59) Barkhuijsen, H.; de Beer, R.; van Ormondt, D. Aspects of the computational efficiency of LPSVD. *J. Magn. Reson.* **1985**, *64*, 343-346.

(60) Barkhuijsen, H.; de Beer, R.; van Ormondt, D. Improved algorithm for noniterative time-domain model fitting to exponentially damped magnetic resonance signals. *J. Magn. Reson.* **1987**, *73*, 553-557.

(61) Wang, W.; Ye, X.; Demidov, A. A.; Rosca, F.; Sjodin, T.; Cao, W.; Sheeran, M.; Champion, P. M. Femtosecond multicolor pump-probe spectroscopy of ferrous cytochrome *c*. *J. Phys. Chem. B* **2000**, *104*, 10789-10801.

(62) Wang, W.; Demidov, A.; Ye, X.; Christian, J. F.; Sjodin, T.; Champion, P. M. Application of femtosecond coherence spectroscopy to the observation of nuclear motions in heme proteins and transparent solutions. *J. Raman Spectr.* **2000**, *31*, 99-105.

(63) Shelly, K. R.; Golovich, E. C.; Beck, W. F. Intermolecular vibrational coherence in bacteriochlorophyll *a* with clustered polar solvent molecules. *J. Phys. Chem. B* **2006**, *110*, 20586-20595. DOI: 10.1021/jp062909v.

(64) Shelly, K. R.; Carson, E. A.; Beck, W. F. Vibrational coherence from the dipyridine complex of bacteriochlorophyll *a:* intramolecular modes in the 10-220 cm^{-1} regime, intermolecular solvent modes, and relevance to photosynthesis. *J. Am. Chem. Soc.* **2003**, *125*, 11810-11811. DOI: 10.1021/ja0366890.

(65) Shelly, K. R.; Golovich, E. C.; Dillman, K. L.; Beck, W. F. Intermolecular vibrational coherence in the purple-bacterial light-harvesting proteins B777 and B820 from *Rhodospirillum rubrum*. *J. Phys. Chem. B* **2008**, *112*, 1299-1307. DOI: 10.1021/jp077103p.

(66) Roszak, A. W.; Howard, T. D.; Southall, J.; Gardiner, A. T.; Law, C. J.; Isaacs, N. W.; Cogdell, R. J. Crystal structure of the RC-LH1 core complex from *Rhodopseudomonas palustris*. *Science* **2003**, *302*, 1969-1972.

(67) Sturgis, J. N.; Robert, B. Thermodynamics of membrane polypeptide oligomerization in light-harvesting complexes and associated structural changes. *J. Mol. Biol.* **1994**, *238*, 445-454.

(68) Miller, J. F.; Hinchigeri, S. B.; Parkes-Loach, P. S.; Callahan, P. M.; Sprinkle, J. R.; Riccobono, J. R.; Loach, P. A. Isolation and characterization of a subunit form

of the light-harvesting complex of *Rhodospirillum rubrum*. *Biochemistry* **1987**, *26*, 5055–5062.

(69) Parkes-Loach, P. S.; Sprinkle, J. R.; Loach, P. A. Reconstitution of the B873 light-harvesting complex of *Rhodospirillum rubrum* from the separately isolated α- and β-polypeptides and bacteriochlorophyll *a*. *Biochemistry* **1988**, *27*, 2718–2727.

(70) Pandit, A.; Visschers, R. W.; van Stokkum, I. H. M.; Kraayenhof, R.; van Grondelle, R. Oligomerization of light-harvesting I antenna peptides of *Rhodospirillum rubrum*. *Biochemistry* **2001**, *40*, 12913–12924.

(71) Arluison, V.; Seguin, J.; Robert, B. The reaction order of the dissociation reaction of the B820 subunit of *Rhodospirillum rubrum* light-harvesting I complex. *FEBS Lett.* **2002**, *516*, 40–42.

(72) Wang, Z. Y.; Gokan, K.; Kobayashi, M.; Nozawa, T. Solution structures of the core light-harvesting alpha and beta polypeptides from *Rhodospirillum rubrum*: Implications for the pigment-protein and protein-protein interactions. *J. Mol. Biol.* **2005**, *347*, 465–477.

(73) Deisenhofer, J.; Epp, O.; Miki, K.; Huber, R.; Michel, H. X-ray structure analysis of a membrane protein complex: electron density map at 3 Å resolution and a model of the chromophores of the photosynthetic reaction center from *Rhodopseudomonas viridis*. *J. Mol. Biol.* **1984**, *180*, 385–398.

(74) Diffey, W. M.; Homoelle, B. J.; Edington, M. D.; Beck, W. F. Excited-state vibrational coherence and anisotropy decay in the bacteriochlorophyll *a* dimer protein B820. *J. Phys. Chem. B* **1998**, *102*, 2776–2786.

(75) Hu, X.; Schulten, K. Model for the light-harvesting complex I (B875) of *Rhodobacter sphaeroides*. *Biophys. J.* **1998**, *75*, 683–694.

(76) Vos, M. H.; Jones, M. R.; Hunter, C. N.; Breton, J.; Martin, J. -L. Coherent nuclear dynamics at room temperature in bacterial reaction centers. *Proc. Nat. Acad. Sci. USA* **1994**, *91*, 12701–12705.

(77) Stanley, R. J.; Boxer, S. G. Oscillations in the spontaneous fluorescence from photosynthetic reaction centers. *J. Phys. Chem.* **1995**, *99*, 859–863.

(78) Vos, M. H.; Rischel, C.; Jones, M. R.; Martin, J. -L. Electrochromic detection of a coherent component in the formation of the charge pair P+HL in bacterial reaction centers. *Biochemistry* **2000**, *39*, 8353–8361.

(79) Yakovlev, A. G.; Shkuropatov, A. Y.; Shuvalov, V. A. Nuclear wavepacket motion producing a reversible charge separation in bacterial reaction centers. *FEBS Lett.* **2000**, *466*, 209-212.

(80) Yakovlev, A. G.; Shkuropatov, A. Y.; Shuvalov, V. A. Nuclear wave packet motion between P* and $P^+B_A^-$ potential surfaces with a subsequent electron transfer to H_A in bacterial reaction centers at 90 K. Electron transfer pathway. *Biochemistry* **2002**, *41*, 14019-14027.

(81) Yakovlev, A. G.; Shkuropatov, A. Y.; Shuvalov, V. A. Nuclear wavepacket motion between P* and $P^+B_A^-$ potential surfaces with a subsequent electron transfer to H_A in bacterial reaction centers. 1. Room temperature. *Biochemistry* **2002**, *41*, 2667-2674.

(82) Shuvalov, V. A.; Yakovlev, A. G. Coupling of nuclear wavepacket motion and charge separation in bacterial reaction centers. *FEBS Lett.* **2003**, *540*, 26-34.

(83) Spörlein, S.; Zinth, W.; Wachtveitl, J. Vibrational coherence in photosynthetic reaction centers observed in the bacteriochlorophyll anion band. *J. Phys. Chem. B* **1998**, *102*, 7492-7496.

(84) Huppmann, P.; Spörlein, S.; Bibikova, M.; Oesterhelt, D.; Wachtveitl, J.; Zinth, W. Electron transfer in reaction centers of *Blastochloris viridis*: photosynthetic reactions approximating the adiabatic regime. *J. Phys. Chem. A* **2003**, *107*, 8302-8309.

(85) Palaniappan, V.; Aldema, M. A.; Frank, H. A.; Bocian, D. F. Q_y-excitation resonance Raman scattering from the special pair in extitRhodobacter sphaeroides reaction centers. Implications for primary charge separation. *Biochemistry* **1992**, *31*, 11050-11058.

(86) Czarnecki, K.; Diers, J. R.; Chynwat, V.; Erickson, J. P.; Frank, H. A.; Bocian, D. F. Characterization of the strongly coupled, low-frequency vibrational modes of the special pair of photosynthetic reaction centers via isotopic labeling of the cofactors. *J. Am. Chem. Soc.* **1997**, *119*, 415-426.

(87) Frisch, M. J.; Trucks, G. W.; Schlegel, H. B.; Scuseria, G. E.; Robb, M. A.; Cheeseman, J. R.; Montgomery, J. A. J.; Vreven, T.; Kudin, K. N.; Burant, J. C.; Millam, J. M.; Iyengar, S. S.; Tomasi, J.; Barone, V.; Mennucci, B.; Cossi, M.; Scalmani, G.; Rega, N.; Petersson, G. A.; Nakatsuji, H.; Hada, M.; Ehara, M.; Toyota, K.; Fukuda, R.; Hasegawa, J.; Ishida, M.; Nakajima, T.; Honda, Y.; Kitao, O.; Nakai, H.; Klene, M.; Li, X.; Knox, J. E.; Hratchian, H. P.; Cross, J. B.; Bakken, V.; Adamo, C.; Jaramillo, J.; Gomperts, R.; Stratmann, R. E.; Yazyev, O.; Austin, A. J.; Cammi, R.; Pomelli, C.; Ochterski, J. W.; Ayala, P. Y.; Morokuma, K.; Voth, G. A.; Salvador,

P.; Dannenberg, J. J.; Zakrzewski, V. G.; Dapprich, S.; Daniels, A. D.; Strain, M. C.; Farkas, O.; Malick, D. K.; Rabuck, A. D.; Raghavachari, K.; Foresman, J. B.; Ortiz, J. V.; Cui, Q.; Baboul, A. G.; Clifford, S.; Cioslowski, J.; Stefanov, B. B.; Liu, G.; Liashenko, A.; Piskorz, P.; Komaromi, I.; Martin, R. L.; Fox, D. J.; Keith, T.; Al-Laham, M. A.; Peng, C. Y.; Nanayakkara, A.; Challacombe, M.; Gill, P. M. W.; Johnson, B.; Chen, W.; Wong, M. W.; Gonzalez, C.; Pople, J. A. *Gaussian 03, Revision D.01*; Gaussian, Inc.: Wallingford, CT, 2004.

(88) Dillman, K. L.; Shelly, K. R.; Beck, W. F. Vibrational coherence in polar solutions of Zn^{II} tetrakis(N-methylpyridyl)porphyrin with Soret-band excitation: rapidly damped intermolecular modes with clustered solvent molecules and slowly damped intramolecular modes from the porphyrin macrocycle. *J. Phys. Chem. B* **2009**, *113*, 6127-6139. DOI: 10.1021/jp807795x.

(89) Lakowicz, J. R. *Principles of Fluorescence Spectroscopy*; Kluwer Academic/Plenum Publishers: New York, 1999.

(90) Diffey, W. M.; Beck, W. F. Rapid-scanning interferometer for ultrafast pump-probe spectroscopy with phase-sensitive detection. *Rev. Sci. Instrum.* **1997**, *68*, 3296-3300.

(91) Cantor, C. R.; Schimmel, P. R. *Biophysical Chemistry. Part II: Techniques for the Study of Biological Structure and Function*; W. H. Freeman and Company: San Francisco, 1980.

(92) McHale, J. L. *Molecular Spectroscopy*; Prentice Hall: Upper Saddle River, New Jersey, 1999.

(93) Cong, P.; Deuhl, H. P.; Simon, J. D. Using optical coherence to measure the ultrafast electronic dephasing of large molecules in room-temperature liquids. *Chem. Phys. Lett.* **1993**, *211*, 367-373.

(94) Joo, T.; Jia, Y.; Yu, J. -Y.; Lang, M. J.; Fleming, G. R. Third-order nonlinear time domain probes of solvation dynamics. *J. Chem. Phys.* **1996**, *104*, 6089-6108.

(95) Xu, Q.; Ma, Y.; Stiopkin, I. V.; Fleming, G. R. Wavelength-dependent resonant homodyne and heterodyne transient grating spectroscopy with a diffractive optics method: Solvent effect on the third-order signal. *J. Chem. Phys.* **2002**, *116*, 9333-9340.

(96) Stratt, R. M. The instantaneous normal modes of liquids. *Acc. Chem. Res.* **1995**, *28*, 201-207.

(97) Stratt, R. M.; Maroncelli, M. Nonreactive dynamics in solution: the emerging molecular view of solvation dynamics and vibrational relaxation. *J. Phys. Chem.* **1996**, *100*, 12981-12996.

(98) Siano, D. B.; Metzler, D. E. Band shapes of the electronic spectra of complex molecules. *J. Chem. Phys.* **1969**, *51*, 1856-1861.

(99) Vanden Bout, D.; Berg, M. Ultrafast Raman echo experiments in liquids. *J. Raman Spectr.* **1995**, *26*, 503-511.

(100) Berg, M.; Vanden Bout, D. A. Ultrafast Raman echo measurements of vibrational dephasing and the nature of solvent-solute interactions. *Acc. Chem. Res.* **1997**, *30*, 65-71.

(101) Yu, H. -Z.; Baskin, J. S.; Zewail, A. H. Ultrafast dynamics of porphyrins in the condensed phase: II. Zinc tetraphenylporphyrin. *J. Phys. Chem. A.* **2002**, *106*, 9845-9854. DOI: 10.1021/jp0203999.

(102) Yoon, M. -C.; Jeong, D. H.; Cho, S.; Kim, D.; Rhee, H.; Joo, T. Ultrafast transient dynamics of Zn(II) porphyrins: observation of vibrational coherence by controlling chirp of femtosecond pulses. *J. Chem. Phys.* **2003**, *118*, 164-171.

(103) Enescu, M.; Steenkeste, K.; Tfibel, F.; Fontaine-Aupart, M. -P. Femtosecond relaxation processes from upper excited states of tetrakis(N-methyl-4-pyridyl)porphyrins studied by transient absorption spectroscopy. *Phys. Chem. Chem. Phys.* **2002**, *4*, 6092-6099.

(104) Jean, J. M.; Fleming, G. R. Competition between energy and phase relaxation in electronic curve crossing processes. *J. Chem. Phys.* **1995**, *103*, 2092-2101.

(105) Franzen, S.; Fritsch, K.; Brewer, S. H. Experimental observation of anharmonic coupling of the heme-doming and iron-ligand out-of-plane vibrational modes confirmed by density functional theory. *J. Phys. Chem. B* **2002**, *106*, 11641-11646.

(106) Morikis, D.; Li, P.; Bangcharoenpaurpong, O.; Sage, J. T.; Champion, P. M. Resonance Raman scattering as a probe of electron-nuclear coupling: applications to heme proteins. *J. Phys. Chem.* **1991**, *95*, 3391-3398.

(107) Ladanyi, B. M.; Stratt, R. M. Short-time dynamics of solvation: linear solvation theory for polar solvents. *J. Phys. Chem.* **1995**, *99*, 2502-2511.

(108) Wilson, Jr., E. B.; Decius, J. C.; Cross, P. C. *Molecular Vibrations: The Theory of Infrared and Raman Vibrational Spectra*; McGraw-Hill: New York, 1955.

(109) Garg, S. K.; Smyth, C. P. Microwave absorption and molecular structures in liquids. LXII. The three dielectric dispersion regions of the normal primary alcohols. *J. Phys. Chem.* **1965**, *69*, 1294-1301.

(110) Jorgensen, W. L. Structure and properties of liquid methanol. *J. Am. Chem. Soc.* **1980**, *102*, 543-549.

(111) Bertolini, D.; Cassettari, M.; Salvetti, G. The dielectric properties of alcohols-water solutions. I. The alcohol rich region. *J. Chem. Phys.* **1983**, *78*, 365-372.

(112) Sumi, H.; Marcus, R. A. Dielectric relaxation and intramolecular electron transfers. *J. Chem. Phys.* **1986**, *84*, 4272-4276.

(113) London, F. The general theory of molecular forces. *Trans. Faraday Soc.* **1937**, *33*, 8-26.

(114) Margenau, H. Van der Waals forces. *Rev. Mod. Phys.* **1939**, *11*, 1-35.

(115) Kauzmann, W. *Quantum Chemistry: An Introduction*; Academic Press: New York, 1957.

(116) Berry, R. S.; Rice, S. A.; Ross, J. *Physical Chemistry*; Oxford University Press: New York, 2000.

(117) Lide D. R., Ed. *CRC Handbook of Chemistry and Physics*; CRC Press, Inc.: Boca Raton, Florida, 2006.

(118) He, Z.; Sundstrom, V.; Pullerits, T. Excited states of carotenoid in LH2: an ab initio study. *Chem. Phys. Lett.* **2001**, *334*, 159-167.

(119) Jin, R. -H.; Aoki, S.; Shima, K. Phosphoniumyl cationic porphyrins: self-aggregation origin from π-π and cation-π interactions. *J. Chem. Soc. Faraday Trans.* **1997**, *93*, 3945-3953.

(120) Albrecht, A. C. "Forbidden" character in allowed electronic transitions. *J. Chem. Phys.* **1960**, *33*, 156-169.

(121) Tang, J.; Albrecht, A. C. Developments in the theories of vibrational Raman intensities. In *Raman Spectroscopy: Theory and Practice*; Szymanski, H. A., Ed.; Plenum: New York, 1970; Vol. 2, pp 33-68.

(122) Arnett, D. C.; Vohringer, P.; Scherer, N. F. Excitation dephasing, product formation, and vibrational coherence in an intervalence charge-transfer reaction. *J. Am. Chem. Soc.* **1995**, *117*, 12262-12272.

(123) Yang, T. -S.; Chang, M. -S.; Chang, R.; Hayashi, M.; Lin, S. H.; Vohringer, P.; Dietz, W.; Scherer, N. F. Femtosecond pump-probe study of molecular vibronic structures and dynamics of a cyanine dye in solution. *J. Chem. Phys.* **1999**, *110*, 12070-12081.

(124) Liebl, U.; Lipowski, G.; Negrerie, M.; Lambry, J. -C.; Martin, J. -L.; Vos, M. H. Coherent reaction dynamics in a bacterial cytochrome *c* oxidase. *Nature* **1999**, *401*, 181-184.

(125) Deisenhofer, J.; Epp, O.; Miki, K.; Huber, R.; Michel, H. Structure of the protein subunits in the photosynthetic reaction center of *Rhodopseudomonas viridis* at 3.1 Å resolution. *Nature* **1985**, *318*, 618-624.

(126) Deisenhofer, J.; Michel, H. The photosynthetic reaction center from the purple bacterium *Rhodopseudomonas viridis*. *Science* **1989**, *245*, 1463-1473.

(127) Blom, N.; Odo, J.; Nakamoto, K.; Strommen, D. P. Resonance Raman studies of metal tetrakis(4-N-methylpyridyl)porphine: band assignments, structure-sensitive bands, and species equilibria. *J. Phys. Chem.* **1986**, *90*, 2847-2852. DOI: 10.1021/j100404a015.

(128) Spence, T. G.; Trotter, B. T.; Burns, T. D.; Posey, L. A. Metal-to-ligand charge transfer in the gas-phase cluster limit. *J. Phys. Chem. A* **1998**, *102*, 6101-6106.

(129) Vanderkooi, J. M.; Adar, F.; Ericińska, M. Metallocytochromes *c:* characterization of electronic absorption and emission spectra of Sn^{4+} and Zn^{4+} cytochromes *c*. *Eur. J. Biochem.* **1976**, *64*, 381-387.

(130) Elias, H.; Chou, M. H.; Winkler, J. R. Electron-transfer kinetics of Zn-substituted cytochrome *c* and its $Ru(NH_3)_5$(Histidine-33) derivative. *J. Am. Chem. Soc.* **1988**, *110*, 429-434.

(131) Ye, S.; Shen, C.; Cotton, T. M.; Kostić, N. M. Characterization of zinc-substituted cytochrome *c* by circular dichroism and resonance Raman spectroscopic methods. *J. Inorg. Biochem.* **1997**, *65*, 219-226.

(132) Goto, Y.; Calciano, L. J.; Fink, A. L. Acid-induced folding of proteins. *Proc. Natl. Acad. Sci. U.S.A.* **1990**, *87*, 573-577.

(133) Tremain, S. M.; Kostić, N. M. Molten-globule and other conformational forms of zinc cytochrome *c*. Effect of partial and complete unfolding of the protein on its electron-transfer reactivity. *Inorg. Chem.* **2002**, *41*, 3291-3301.

(134) Nappa, M.; Valentine, J. S. The influence of axial ligands on metalloporphyrin visible absorption spectra. Complexes of tetraphenylporphynatozinc. *J. Am. Chem. Soc.* **1978**, *100*, 5075-5080.

(135) Humphry-Baker, R.; Kalyanasundaram, K. Influence of axial ligation on the fluorescence of tetrakisphenylporphyrins. *J. Photochem.* **1985**, *31*, 105-112.

(136) Vogel, G. C.; Beckmann, B. A. Binding of pyridine to phenyl-substituted derivatives of zinc tetraphenylporphine. *Inorg. Chem.* **1976**, *15*, 483-484.

(137) Scheidt, R. W. Porphyrin stereochemistry. In *The Porphyrins*; Dolphin, D., Ed.; Academic Press: New York, 1978; Vol. 3, pp 463-511.

(138) Fleischer, E. B.; Miller, C. K.; Webb, L. E. Crystal and molecular structures of some metal tetraphenylporphines. *J. Am. Chem. Soc.* **1964**, *86*, 2342-2347.

(139) Schauer, C. K.; Anderson, O. P.; Eaton, S. S.; Eaton, G. R. Crystal and molecular structure of a six-coordinate zinc porphyrin: bis(tetrahydrofuran)(5,10,15,20-tetraphenylporphinato)zinc(II). *Inorg. Chem.* **1985**, *24*, 4082-4086.

(140) Scheidt, R. W.; Eigenbrot, C. W.; Ogiso, M.; Hatano, K. Stereochemistry of a porphyrin atropisomer. The molecular and crystal structure of six-coordinate [5α, 10β-bis(o-nicotinamidophenyl)-15,20-diphenylporphinato] zinc(II). *Bull. Chem. Soc. Jpn.* **1987**, *60*, 3529-3533.

(141) Lampa-Pastirk, S.; Lafuente, R. C.; Beck, W. F. Excited-state axial-ligand photodissociation and nonpolar protein-matrix reorganization in Zn(II)-substituted cytochrome *c*. *J. Phys. Chem. B* **2004**, *108*, 12602-12607. DOI: 10.1021/jp049587k.

(142) Damaschun, G.; Gernat, C.; Damaschun, H.; Bychkova, V. E.; Ptitsyn, O. B. Comparison of intramolecular packing of a protein in native and 'molten globule' states. *Int. J. Biol. Macromol.* **1986**, *8*, 226-230.

(143) Ptitsyn, O. B. The molten globule state. In *Protein Folding*; Creighton, T. E., Ed.; W. H. Freeman and Company: New York, 1993; pp 243-300.

(144) Kataoka, M.; Hagihara, Y.; Mihara, K.; Goto, Y. Molten globule of cytochrome *c* studied by small angle x-ray scattering. *J. Mol. Biol.* **1993**, *229*, 591-596.

(145) Hamada, D.; Kuroda, Y.; Kataoka, M.; Aimoto, S.; Yoshimura, T.; Goto, Y. Role of heme axial ligands in the conformational stability of the native and molten globule states of horse cytochrome *c*. *J. Mol. Biol.* **1996**, *256*, 172-186.

(146) Kamiyama, T.; Sadahide, Y.; Nogusa, Y.; Gekko, K. Polyol-induced molten globule of cytochrome *c*: an evidence for stabilization by hydrophobic interaction. *Biochim. Biophys. Acta* **1999**, *1434*, 44-57.

(147) Lyubovitsky, J. G.; Gray, H. B.; Winkler, J. R. Structural features of the cytochrome *c* molten globule revealed by fluorescence energy transfer kinetics. *J. Am. Chem. Soc.* **2002**, *124*, 14840-14841.

(148) Bongiovanni, C.; Sinibaldi, F.; Ferri, T.; Santucci, R. Glycerol-induced formation of the molten globule from acid-denatured cytochrome *c*: Implication for hierarchical folding. *J. Protein Chem.* **2002**, *21*, 35-41.

(149) Anni, H.; Vanderkooi, J. M.; Mayne, L. Structure of zinc-substituted cytochrome *c*: nuclear magnetic resonance and optical spectroscopic studies. *Biochemistry* **1995**, *34*, 5744-5753.

(150) Qian, C.; Yao, Y.; Tong, Y.; Wang, J.; Tang, W. Structural analysis of zinc-substituted cytochrome *c*. *J. Biol. Inorg. Chem.* **2003**, *8*, 394-400.

(151) Teczan, F. A.; Crane, B. R.; Winkler, J. R.; Gray, H. B. Electron tunneling in protein crystals. *Proc. Natl. Acad. Sci. U.S.A.* **2001**, *98*, 5002-5006.

(152) Berghuis, A. M.; Brayer, G. D. Oxidation state-dependent conformational changes in cytochrome *c*. *J. Mol. Biol.* **1992**, *223*, 959-976.

(153) Pielak, G. J.; Auld, D. S.; Betz, S. F.; Hilgen-Willis, S. E.; Garcia, L. L. Nuclear magnetic resonance studies of class I cytochromes *c*. In *Cytochrome* c*: a Multidisciplinary Approach*; Scott, R. A., Mauk, A. G., Eds.; University Science Books: Sausalito, California, 1996; pp 203-284.